

DISSERTATION

APPROACHING ARCTIC-MIDLATITUDE DYNAMICS FROM A TWO-WAY FEEDBACK
PERSPECTIVE

Submitted by

Marie C. McGraw

Department of Atmospheric Science

In partial fulfillment of the requirements

For the Degree of Doctor of Philosophy

Colorado State University

Fort Collins, Colorado

Spring 2019

Doctoral Committee:

Advisor: Elizabeth A. Barnes

David A. Randall

Russ. S. Schumacher

Karan Venayagamoorthy

Copyright by Marie C. McGraw 2019

All Rights Reserved

ABSTRACT

APPROACHING ARCTIC-MIDLATITUDE DYNAMICS FROM A TWO-WAY FEEDBACK PERSPECTIVE

Arctic variability and the variability of the midlatitude circulation are closely intertwined. Although these connections are interrelated and bi-directional, and occur on a variety of timescales, they are not often studied together. Modeling studies generally focus on a single direction of influence—usually, how the midlatitude circulation responds to the Arctic. Studying these relationships in a two-way feedback perspective can offer new insights into these connections, providing information on how they feed back upon each other.

This work approaches Arctic-midlatitude dynamics from a two-way feedback perspective, mostly on sub-monthly timescales. Particular emphasis is placed on the influence of midlatitude circulation variability upon the Arctic, as this direction of influence is less-studied than the converse pathway. Reinforcing feedback loops are identified between the North Pacific and North Atlantic jet streams and the Arctic. Variability in both the North Atlantic and North Pacific jet streams drives Arctic variability, which then drives further variability in the jet streams. The circulation variability in many regions, including North America, the east Pacific and Alaska, and Siberia, drives Arctic variability far more than it is driven by Arctic variability. These relationships exhibit substantial regional variability, stressing the important role of an analytical approach that incorporates this spatial heterogeneity. The two-way nature of Arctic-midlatitude connections is also explored in the context of Arctic moisture fluxes. The circulation response to sea ice loss also drives changes in Arctic moisture fluxes, with moisture flux out of the Arctic increasing more than moisture flux into the Arctic.

The two-way feedback perspective explored in this research is built around the ideas of causal discovery, particularly Granger causality. Most of these two-way Arctic-midlatitude relationships

are considered in the context of added variance explained, or added predictive power. That is, these relationships are characterized by comparing how much an additional predictor improves predictability beyond autocorrelation. Limiting the ability of autocorrelation to color these results emphasizes added variance explained—how much additional variance in the circulation can be explained by Arctic temperature variability, and vice versa? As an example, many recent studies have concluded that warm Arctic temperatures or low sea ice conditions drive a strengthening of high pressures and an increase in cold temperatures over Siberia. However, when memory and autocorrelation are accounted for, it emerges that the circulation variability over Siberia drives a response in the Arctic more than the other way around—results that are in concordance with modeling studies that have also disputed the veracity of the claim of the Arctic driving a strong response in Siberia.

Ultimately, this research seeks to offer a different perspective on analyzing climate dynamics, with an emphasis on two-way feedbacks. While targeted climate modeling studies offer great physical insights, and provide substantial opportunities to explore and test physical mechanisms, they are often limited to exploring only one pathway of influence. In reality, these relationships do go in both directions, and a comprehensive understanding of such large-scale interactions between different parts of the atmosphere must ultimately consider the two-way relationships. The causal discovery methods used in much of this research can be used in conjunction with modeling studies to better understand these two-way relationships, and improve interpretation of results. While this research has focused on the relationships between the Arctic and the midlatitude circulation on sub-seasonal timescales, the broad framework and ideas presented within can be more widely applied to many other questions in climate variability studies. Thus, this work has also put a special emphasis on describing and implementing these causality-based methods in a manner that is accessible and interpretable for atmospheric and climate scientists.

ACKNOWLEDGMENTS

This work was completed over the course of five and a half years. It is the result of the labor, direct and indirect, of many hands, eyes, and brains—too many to explicitly mention here. Thus, for the sake of brevity, only the most easily definable contributions are explicitly listed here; however, that does not render that which was excluded any less meaningful.

First, I would like to thank my advisor, Elizabeth Barnes, who has guided me from a student of science to an interpreter and disseminator of scientific research. She has created and maintained high standards for her students without imposing them, offered guidance without interference, reshaped and revised innumerable rewrites and unappealing figures, and endured thousands of my frustrated scowls and sighs. Thank you.

I have also profited from the patience and knowledge of my Ph.D. committee—Thomas Birner, David Randall, Russ Schumacher, and Karan Venayagamoorthy. I thank you profusely for your time and your energy in serving on my committee and offering me constructive feedback. Many thanks to Lantao Sun of the NOAA/Earth System Research Laboratory, who generously provided the model output analyzed in Chapter 5. I have been fortunate enough to collaborate with scientists outside of Colorado State, most notably, Tim Woollings of Oxford University, and especially Clara Deser and her group at the National Center for Atmospheric Research. Although none of this work is included here, these collaborations have provided me with opportunities to explore new research topics, to present my own work to a broader audience, and to sustain viable long-term relationships with scientists across the world.

I have reaped enormous rewards from close collaboration with and extremely patient tutelage from Professor Imme Ebert-Uphoff and Savini Samarasinghe in the Department of Electrical and Computer Engineering. Few people have influenced this work as closely as Imme and Savini, and I am deeply indebted to them. In particular, the code that forms the backbone of Chapter 3 and influences much of Chapter 4 would have been impossible without them.

Research and ideas are not just sparked by conversations with one's superiors. The students and staff in the Barnes research group, past and present, have been collaborators, co-authors, conspirators, sounding boards,

captive audiences, and correctors. My most heartfelt thanks and sincere appreciation to Chengji Liu, Bryan Mundhenk, Cory Baggett, Savini Samarasinghe, Steven Brey, Bryn Ronalds, Kai-Chih Tseng, Andrea Jenney, Kyle Nardi, Kirsten Mayer, and Ben Toms. In particular, the work in Chapter 5 would not have been possible without Chengji Liu and his Rossby wave breaking detection algorithm; Bryan Mundhenk and his preliminary work and initial leadership in spearheading this effort; and especially Cory Baggett and his 18+ months of consistent hard work, superior understanding of atmospheric energy and moisture transport, and rigorous standards in producing excellent research.

Outside of my own group, I have benefitted greatly from the expertise of other atmospheric and climate dynamics experts at Colorado State inside and out of the classroom. Thank you to professors Thomas Birner, Eric Maloney, David Thompson, and David Randall, and their groups for over 5 years of derivations and discussions. I have received special assistance in all aspects of becoming an effective and well-rounded scientist from Nick Davis, Ed Charlesworth, Stephanie Henderson, Brandon Wolding, Samantha Wills, Jingyuan Li, Brian Crow, and Alex Naegele. I am very grateful to Greg Herman and Jingyuan Li for consistently offering helpful, specific feedback and ideas on many topics related to statistical methods.

Although it has been more than a decade since I moved away, I have always depended on the support of my family, even when I have not recognized it. To my parents, Mary Haas McGraw and Brian McGraw, my brother Tom and almost sister Libby, my sister Karen, and my uncle Jim Haas—more than anyone else, you have encouraged me to work consistently and diligently, to treat people and ideas with respect, and to act in accordance with my own values. I would also like to remember my grandmother, Eileen Haas (1923-2016), who remains a benchmark of humility and selflessness that I continue to reach for (and inevitably fall short of). If I have ever made you a cookie, cheesecake, or cinnamon roll, you should thank her too.

It is no exaggeration to say that I could fill another book with lavish praise and ardent expressions of gratitude acknowledging the support of my friends, near and far. In particular, I struggle to express something that is properly appreciative of everything that makes atmospheric science at Colorado State the peerless community that it is. For reasons sufficient to the author, I will not try to do so; instead, I will only say that I am deeply aware of how much you all have given me, and that I would not change a day of this experience. Thank you.

TABLE OF CONTENTS

ABSTRACT	ii
ACKNOWLEDGMENTS	v
LIST OF TABLES	viii
LIST OF FIGURES	ix
Chapter 1. Introduction	1
1.1 The Two-Way Nature of Arctic-Midlatitude Teleconnections	1
1.2 Scope of This Work	5
Chapter 2. An Overview of Granger Causality and A Case for Its Use in Climate Science	8
2.1 Introduction to Granger Causality	8
2.2 Developing the Monte Carlo Model	12
2.3 Monte Carlo Model Results	14
2.4 Applications in Climate Variability	18
2.5 Discussion	23
Chapter 3. Granger and Pearl Causality Models for Climate Science	25
3.1 Intervention and an Overview of Graphical Methods	25
3.2 Vector Autoregression (VAR) Model	28
3.3 Regularized Regression Model (LASSO)	31
3.4 Pearl Causality and the PC-Stable Algorithm	36
3.5 Climate Model Data	38
3.6 Application of Causal Discovery Methods to Arctic-Jet Stream Connections	39
3.7 Conclusions	48
Chapter 4. New Insights on Subseasonal Arctic-Midlatitude Causal Connections from a Regularized Regression Model	50

4.1	Introduction	50
4.2	Data and Methods	53
4.3	Results	57
4.4	Discussion	69
4.5	Conclusions	71
Chapter 5.	Changes in Arctic Moisture Transport Over the North Pacific Associated with Sea Ice Loss	73
5.1	Introduction	73
5.2	Methods	76
5.3	Results	79
5.4	Conclusions	95
5.5	Additional Figures	97
Chapter 6.	Conclusions	99
6.1	The Role of Midlatitude Variability in Driving an Arctic Response	99
6.2	The Persistence of Memory	101
6.3	A Difference of Perspective	103
References	105
Appendix A.	Additional VAR and LASSO Model Results for CESM	122
A1	Assessing the Significance of the VAR Model	122
A2	Results of the VAR Model for MERRA-2	123
A3	VAR Model Results for CESM	124

LIST OF TABLES

Table 4.1 Region definitions.	64
---------------------------------------	----

LIST OF FIGURES

Fig. 1.1	Change in observed annual mean surface temperature from 1963-2012.	2
Fig. 2.1	Using lagged regression to test the hypothesis that (a) ENSO drives T_s , and (b) T_s drives ENSO.	10
Fig. 2.2	Testing the hypothesis that D drives R using (a) lagged regression, and (b) Granger causality.	15
Fig. 2.3	Testing the hypothesis that R drives D using (a) lagged regression, and (b) Granger causality.	17
Fig. 2.4	Using (a,b) lagged regression and (c,d) Granger causality to test the hypothesis that (a,c) ENSO drives T_s , and (b,d) T_s drives ENSO.	19
Fig. 2.5	Using (a,b) lagged regression and (c,d) Granger causality to test the hypothesis that (a,c) polar mean temperature drives 700 hPa zonal winds, and (b,d) 700 hPa zonal winds drive polar mean temperature.	22
Fig. 3.1	Example of a directed, acyclic graph.	26
Fig. 3.2	Example of a graph with hidden common causes.	27
Fig. 3.3	AIC and BIC values for VAR models of varying p	30
Fig. 3.4	k-folds cross-validation error curves for LASSO for $K = 10$	35
Fig. 3.5	An illustration of the elimination method.	37
Fig. 3.6	Distributions of jet position and strength over the North Pacific in DJF.	40
Fig. 3.7	Arctic temperature (\mathcal{T}) and North Pacific jet speed (\mathcal{S}) relationships as described by VAR, LASSO, and PC models.	42
Fig. 3.8	Arctic temperature (\mathcal{T}) and North Pacific jet latitude (\mathcal{L}) relationships as described by VAR, LASSO, and PC models.	44
Fig. 3.9	Minimalist graphs showing the dominant feedback loops and their time lags identified by all three methods when applicable.	45

Fig. 3.10 Arctic temperature (\mathcal{T}) and North Atlantic jet speed (\mathcal{J}) relationships as described by VAR, LASSO, and PC models.	46
Fig. 3.11 Arctic temperature (\mathcal{T}) and North Atlantic jet latitude (\mathcal{L}) relationships as described by VAR, LASSO, and PC models.	47
Fig. 3.12 Minimalist graphs showing the dominant feedback loops and their time lags identified by all three methods for the North Atlantic.	47
Fig. 4.1 LASSO model of T_{polar} driving Z_{500} at each gridpoint at lags of 5-25 days.	59
Fig. 4.2 LASSO model of Z_{500} at each gridpoint driving T_{polar} at lags of 5-25 days.	61
Fig. 4.3 Zonal anomalies of the time-mean 500 hPa geopotential heights in DJF.	62
Fig. 4.4 Graphical representation of Arctic-midlatitude causal connections for regions in which Z_{500} drives T_{polar}	65
Fig. 4.5 Graphical representation of Arctic-midlatitude causal connections for regions in which T_{polar} drives Z_{500}	66
Fig. 4.6 Simplified schematic of LASSO model results for Arctic-midlatitude causal connections at lags of 5-25 days.	68
Fig. 5.1 Change (PERT - CTRL) in percent of grid box covered by sea ice for associated with sea ice loss in SONDJF.	77
Fig. 5.2 Change (PERT - CTRL) in meridional IVT associated with sea ice loss as a function of (a) month, (b) longitude during SONDJF (highlighted in (a)), and (c) month over the North Pacific region (120-240° E, highlighted in (b)).	81
Fig. 5.3 Change (PERT - CTRL) in the components of meridional IVT during SONDJF associated with sea ice loss as a function of (a) month (SONDJF is highlighted in orange), and (b) longitude (the North Pacific is highlighted in orange).	83
Fig. 5.4 Change (PERT - CTRL) in zonal winds in SONDJF for (a) 850 hPa and (b) 300 hPa.	85
Fig. 5.5 Change (PERT - CTRL) in cyclonic wind shear $\left(-\frac{\partial u}{\partial y}\right)$ at (a) 850 hPa and (b) 300 hPa.	86
Fig. 5.6 Change (PERT - CTRL) in 500 hPa geopotential height in SONDJF.	88

Fig. 5.7	Change (PERT - CTRL) in SONDJF Rossby wave breaking frequency for (a) cyclonic wave breaking and (b) anticyclonic wave breaking events.	90
Fig. 5.8	Lagged composites of anomalous moisture transport across 70° N over the North Pacific during cyclonic wave breaking (CWB) events.	91
Fig. 5.9	Lagged composites of 500 hPa geopotential height (shading) and $I\vec{V}T$ (arrows; only plotted north of 60° N) anomalies during cyclonic Rossby wave breaking events for (left) CTRL, (center) PERT, and (right) PERT - CTRL.	94
Fig. 5.10	As in Figure 2, but for meridional IVT across 65° N.	97
Fig. 5.11	As in Figure 2, but for meridional IVT across 60° N.	98
Fig. A1	VAR model gridpoints exhibiting statistical significance.	123
Fig. A2	LASSO (left) and VAR (right) models of T_{polar} driving Z_{500} at each gridpoint. . .	125
Fig. A3	LASSO (left) and VAR (right) models of Z_{500} at each gridpoint driving T_{polar} . . .	126
Fig. A4	VAR model results for the 7 regions outlined in Table 1.	127
Fig. A5	T_{polar} driving Z_{500} for (left) CESM and (right) MERRA-2.	129
Fig. A6	Z_{500} driving T_{polar} for (left) CESM and (right) MERRA-2.	130
Fig. A7	Percent of 37-year chunks of CESM that agree on the sign of the regression coefficient at each gridpoint.	133

1 Introduction

Rising concentrations of atmospheric carbon dioxide have been linked to especially large temperature changes at high latitudes as early as the late 19th century (Arrhenius (1896)). Polar amplification has been a near-universal response to anthropogenic climate change in model projections for over 30 years (e.g., Manabe and Stouffer (1980), Hansen et al. (1984), Holland and Bitz (2003)). The Arctic has already warmed twice as much as the rest of the Northern Hemisphere land masses over the past 50 years (Figure 1.1a), and coupled climate model projections estimate that Arctic surface temperatures will increase up to four times as much as the global mean surface temperature (Figure 1.1b). Strong sea ice loss accompanies this warming—each of the past five years has seen below-average sea ice extent in the Arctic (Figure 1.1c), while the Fifth Assessment Report of the Intergovernmental Panel on Climate Change estimates that it is likely that the Arctic Ocean will become seasonally ice-free sometime in this century (e.g., Collins et al. (2013)). More recent model projections surmise that ice-free summers in the Arctic Ocean could be the norm by the 2060s under the strongest forcing conditions (e.g., Jahn et al. (2016)). Such widespread and rapid changes in the Arctic have substantial implications for all aspects of the climate system, and the impacts of a warmer Arctic extend to the lower latitudes.

1.1 THE TWO-WAY NATURE OF ARCTIC-MIDLATITUDE TELECONNECTIONS

This question of how a warmer Arctic may affect the weather and climate of the midlatitudes has been of great scientific interest in the past decade. In long-term simulations of climate change, Arctic warming or sea ice loss is linked to warmer atmospheric temperatures across the Northern Hemisphere (e.g., Deser et al. (2015), Tomas et al. (2016)); as well as changes in the large-scale circulation patterns and the midlatitude jet streams. These changes include a weakening of the winds on the poleward side of the midlatitude jet region, and a strengthening on the equatorward side, often characterized as an equatorward shift of the westerlies (e.g., Deser et al. (2015), Blackport

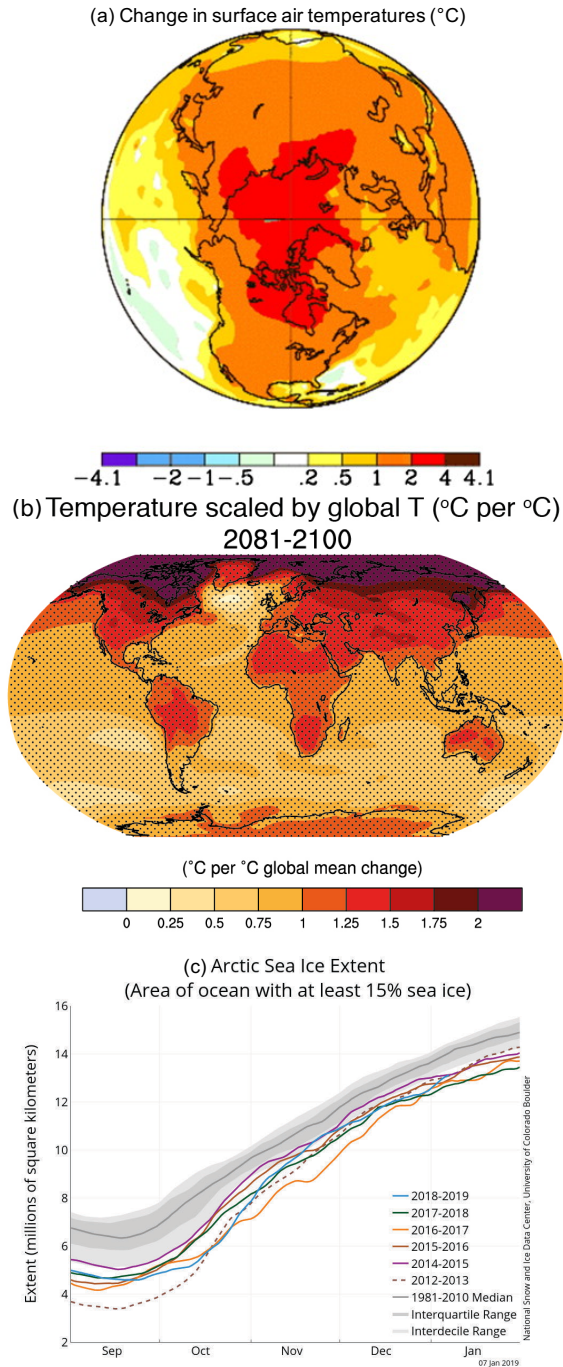


Fig. 1.1. (a) Change in observed annual mean surface temperature from 1963-2012. Reprinted from Walsh (2014). (b) End of 21st century (2081-2100 minus 1985-2005) surface temperature change scaled to 1°C of global mean surface temperature change as estimated by the Coupled Model Intercomparison Project, version 5 (CMIP5) simulations. Stippling indicates where the mean change averaged over all realizations is larger than the 95% percentile of the distribution of models. Reprinted from Collins et al. (2013); consult for more details on how this figure was created. (c) Monthly change in Arctic sea ice extent, separated by year. Gray line indicates the mean sea ice extent from 1981-2010, with shading indicating the variability; colored lines indicate recent years. Reprinted from the National Snow and Ice Data Center.

and Kushner (2016), Smith et al. (2017), Oudar et al. (2017), McCusker et al. (2017), Blackport and Kushner (2017), Peings et al. (2017), Ronalds et al. (2018)). On intraseasonal timescales, the reduction in the equator-to-pole temperature difference that accompanies Arctic warming has been linked to changes in planetary-scale waves that drive blocking events and extreme weather, and changes to large-scale atmospheric variability patterns like the North Atlantic Oscillation (e.g., Francis and Vavrus (2012), Liu et al. (2012), Cattiaux et al. (2016)), although some of these links have been debated (e.g., Barnes (2013), Woollings et al. (2014)). Arctic warming has been connected to reductions in midlatitude temperature variability, as well as the severity of extreme cold temperature events (e.g., Screen et al. (2015b), Ayarzagüena and Screen (2016)). In particular, many studies have described Arctic warming as driving a large-scale atmospheric pattern of variability that is often described as “warm Arctic, cold continents”, although this conclusion has come under debate in recent years (e.g., Overland et al. (2015), Sun et al. (2016), McCusker et al. (2017), Kug et al. (2017), Ogawa et al. (2018), Screen et al. (2018)). A stratospheric pathway of Arctic-midlatitude influence has been identified, with sea ice loss and the associated turbulent fluxes driving changes in vertical wave propagation, which modify the polar stratospheric vortex and ultimately affect tropospheric circulation (e.g., Peings and Magnusdottir (2014), Sun et al. (2015), Wu and Smith (2016), Zhang et al. (2018a)).

While the Arctic can affect the midlatitude circulation, so too can the midlatitudes impact the Arctic. Changes in Arctic temperature and sea ice variability have been linked to intrusions of moist air from outside the Arctic (e.g., Woods et al. (2013), Park et al. (2015a), Park et al. (2015b), Woods and Caballero (2016), Mortin et al. (2016), Burt et al. (2016), Messori et al. (2018)). These Arctic moisture intrusions are intimately linked to the large-scale circulation features of the midlatitudes, such as Rossby wave breaking (e.g., Woods et al. (2013), Liu and Barnes (2015)), and atmospheric rivers (e.g., Newman et al. (2012), Baggett et al. (2016), Mundhenk et al. (2016)). Even tropical convection has been shown to enhance Arctic moisture transport by exciting Rossby wave trains that propagate poleward (e.g., Lee (2014), Baggett and Lee (2017)). The midlatitude circulation can also affect the Arctic through latent energy transport (e.g., Graverson and Burtu (2016)) and warm air advection (e.g., Messori et al. (2018)).

Thus, Arctic variability can drive variability in the midlatitude circulation; and the midlatitude circulation can impact the Arctic. The bi-directional nature of this problem renders a comprehensive understanding of Arctic-midlatitude dynamics elusive, due to the thorny nature of questions of causality. Such issues of cause and effect are often tackled in targeted modeling studies—that is, experiments that study the response of the atmosphere to some external forcing. In the case of Arctic-midlatitude dynamics, the most common approach is to simulate Arctic warming and/or sea ice loss with a variety of approaches including adjusting the surface heat fluxes (e.g., Oudar et al. (2017)), continuously nudging sea ice (e.g., Smith et al. (2017), McCusker et al. (2017)), reducing the albedo of the sea ice (e.g., Blackport and Kushner (2016), Blackport and Kushner (2017)), or simply applying an atmospheric temperature anomaly (e.g., Butler et al. (2010)). Such modeling studies have many advantages, chief among them being a clear pathway of cause and effect, and the opportunity to test and refine physical hypotheses. However, targeted modeling studies such as these have one drawback in common—the Arctic is being continually forced to a certain state—warm air temperature anomalies, lower sea ice, increased heat fluxes from the ocean—regardless of what the atmosphere may be doing. This limits the ability of the midlatitude atmosphere to affect Arctic climate, even though it can and does.

Targeted modeling studies are by design focused on one pathway of influence. Causal discovery-based approaches, which seek to identify cause and effect relationships using frameworks based on added predictive power or causal calculus (e.g., Granger (1969), Pearl (1988), Ebert-Uphoff and Deng (2012)), can be an effective tool for augmenting modeling studies. Causal discovery methods can analyze both directions of influence simultaneously, and can be used to explore feedback loops between variables and processes of interest, such as those concerning Arctic-midlatitude relationships. Such approaches have gained traction in climate science in recent years, although they remain relatively uncommon (e.g., Strong et al. (2009), Kretschmer et al. (2016)). The ability to jointly analyze the Arctic’s influence on the midlatitude circulation and the midlatitude circulation’s impact on the Arctic provides a framework for a more thorough understanding of the complex, two-way feedbacks between the Arctic and the midlatitudes.

1.2 SCOPE OF THIS WORK

The work within this dissertation is focused on approaching Arctic-midlatitude dynamics from this perspective of two-way feedbacks. Most, although not all, of this research uses causal discovery-based approaches. Special attention is paid to the role of the atmospheric circulation in driving Arctic variability, as this pathway is less well-characterized in large-scale climate variability studies than the Arctic driving the midlatitudes. Much of this research has involved close collaboration with computer scientists, and the application of analysis techniques that may be less familiar to climate scientists. Beyond the scientific results, this research has also focused on effective communication of the underlying ideas behind causal discovery methods in the hopes of making them approachable and implementable for people in the atmospheric and climate science communities. Some of the questions addressed within include:

- Can we paint a consistent picture of sub-monthly Arctic-jet stream dynamics using a variety of causal discovery methods?
- What do two-way Arctic-midlatitude relationships look like on sub-monthly timescales, particularly when we account for autocorrelation in the climate system? How do these relationships vary spatially?
- How do Arctic moisture fluxes respond to sea ice loss, and what is the role of the midlatitude circulation in driving this response?

There are four chapters of research in this dissertation, all of which have been published or submitted to peer-reviewed scientific journals. Chapter 2 and Chapter 3 are primarily concerned with exploring an analytical framework based on causal discovery in the context of climate science and Arctic-midlatitude dynamics; they also prioritize the communication of these ideas in an accessible manner. Chapter 4 takes some of the ideas of Chapter 2 and Chapter 3, and uses them to characterize sub-monthly connections between the Arctic and the midlatitude circulation in a manner that focuses on two-way feedbacks. Chapter 5 also explores two-way Arctic-midlatitude dynamics, with a focus on how Arctic warming could affect moisture transport via changes in the circulation. Unlike Chapters 2-4, Chapter 5 does not apply a causal discovery framework to this problem.

Chapter 2 provides an overview of Granger causality (that is, causality based on added predictive power) and its utility in climate variability studies. In particular, it uses a Monte Carlo model as well as examples from climate science to show the advantages of a Granger causality analysis as compared to standard lagged linear regression analysis when one or more variables has autocorrelation. Chapter 2 is published, with slight modifications, in the *Journal of Climate* as:

McGraw, M.C., and E.A. Barnes: Memory Matters: A Case for Granger Causality in Climate Variability Studies. *J. Climate*, **31**, 3289- 3300, <https://doi.org/10.1175/JCLI-D-17-0334.1>.

Chapter 3 describes three methods, based in Granger and Pearl causality frameworks, for assessing causal relationships in climate science, as well as giving a broader overview of graphical methods in climate science. The two-way feedbacks between the Arctic and the midlatitude jet streams on sub-monthly timescales are explored with each of these three approaches, and their strengths and weaknesses are assessed. Ultimately, several relationships between the Arctic and the jet-streams on sub-monthly timescales are identified. There is evidence for positive feedback loops between the Arctic and the jet speed in the North Atlantic and the North Pacific, and the jet position in the North Pacific, meaning that existing anomalies in the Arctic are reinforced (and vice versa). Most of this work has been published in *Environmetrics* as:

Samarasinghe, S., M. McGraw, E. A. Barnes, and I. Ebert-Uphoff: A study of links between the Arctic and the midlatitude jet-stream using Granger and Pearl causality. *Environmetrics*, **e2540**, <https://doi.org/10.1002/env.2540>.

While much of the content of Chapter 3 is contained in Samarasinghe et al. (2018b), Chapter 3 has been substantially rewritten and reorganized from Samarasinghe et al. (2018b), with the addition of expanded background on graphical methods, and on regularized regression. The results from the North Atlantic were also not included in Samarasinghe et al. (2018b).

Chapter 4 explores sub-monthly Arctic-midlatitude causal connections with a regularized regression model. The results from the regularized regression model indicate that, on sub-monthly timescales, the regions in which Arctic temperature variability drives a midlatitude response are

different from those in which the midlatitude circulation drives Arctic variability; and that in many regions, the midlatitude circulation impacts the Arctic more than the Arctic impacts the midlatitude circulation. Most of this work has been submitted for publication, with slight changes, to the *Journal of Climate* as:

McGraw, M.C. and E.A. Barnes: New Insights on Subseasonal Arctic-Midlatitude Causal Connections from a Regularized Regression Model, submitted to *Journal of Climate*, 02/2019.

Chapter 5 explores how Arctic moisture transport changes in response to sea ice loss—that is, how might the atmospheric response to Arctic sea ice loss feed back upon and further modify the Arctic? This work highlights the disproportionate increase in equatorward moisture transport—that is, moisture flux out of the Arctic—and the role that sea ice loss-driven changes in the circulation play in modifying Arctic moisture transport. Most of this work has been submitted for publication, with slight changes, to *Climate Dynamics* as:

McGraw, M.C., Baggett, C.F., Liu, C., and B.D. Mundhenk: Changes in Arctic moisture transport over the North Pacific associated with sea ice loss, *Climate Dynamics*, submitted 02/2019.

Finally, Chapter 6 summarizes the results of this dissertation, and their broader implications, as well as some possible shortcomings. Chapter 6 also provides suggestions for future research.

2 An Overview of Granger Causality and A Case for Its Use in Climate Science¹

In climate variability studies, lagged linear regression is frequently used to infer causality. While lagged linear regression analysis can often provide valuable information about causal relationships, lagged regression is also susceptible to over-reporting significant relationships when one or more of the variables has substantial memory (autocorrelation). Granger causality analysis takes into account the memory of the data and is therefore not susceptible to this issue. A simple Monte Carlo example highlights the advantages of Granger causality compared to traditional lagged linear regression analysis in situations with one or more highly autocorrelated variables. Differences between the two approaches are further explored in two illustrative examples applicable to large-scale climate variability studies. Given that Granger causality is straightforward to calculate, Granger causality analysis may be preferable to traditional lagged regression analysis when one or more data sets has large memory.

2.1 INTRODUCTION TO GRANGER CAUSALITY

The establishment of cause and effect is a fundamental, if elusive, driver of climate science research. While causality is much sought after, it is challenging to establish, especially in observations—recall the adage, “Correlation does not equal causation”. Determining true causality not only requires the establishment of a relationship between two variables but also the far more difficult task of determining a direction of causality. Although they do not provide information regarding directionality, correlation-based methods such as lagged linear regression remain popular and useful tools for identifying lagged relationships between climate variables.

¹This chapter contains material that has been published in the *Journal of Climate* as: McGraw, M.C. and E.A. Barnes, 2018: Memory Matters: A Case for Granger Causality in Climate Variability Studies. *J. Climate*, **31**, 3289-3300, <https://doi.org/10.1175/JCLI-D-17-0334.1>.

A lagged regression model can provide a straightforward assessment of spatial and temporal variability. Lagged regression analysis has been a popular technique in climate science for nearly 100 years (e.g., Walker (1923), Walker (1924)). Since 1988, the phrases “lagged regression”, “lag regression”, “lagged correlation”, and “lag correlation” appear in a combined total of over 800 manuscripts in the *Journal of Climate* alone. Lagged linear regression analysis has been used in a wide variety of climate science applications including, but not limited to: stratosphere-troposphere interactions (e.g., Polvani and Waugh (2004)); tropical variability patterns such as the Madden-Julian Oscillation and the El Niño-Southern Oscillation (e.g., Klein et al. (1999), Hendon et al. (2007)); Arctic sea ice extent (e.g., Blanchard-Wrigglesworth et al. (2011)); and sea surface temperature variability (e.g., Yu et al. (2010)). This is just a small sampling of the hundreds of studies across atmospheric and climate science that utilize linear lagged regression analysis.

While lagged regression can be a straightforward and effective tool for identifying covarying patterns in space and time, lagged regression also has its drawbacks. First, while lagged regression can show the existence of instantaneous and lagged relationships between variables, lagged regression alone cannot indicate the direction of causality. Lagged regression may indicate that two variables are related to each other when in actuality they are linked or driven by a third variable (e.g., Figure 3 in Kretschmer et al. (2016)). Finally, lagged regression can be interpreted to suggest that one variable causes a response in the other when in fact it does not. This can occur when one variable has high memory, or autocorrelation (e.g., Runge et al. (2014), Kretschmer et al. (2016)), and this is the scenario that will be explored here.

As an example, consider the relationship between tropical Pacific sea surface temperatures (that is, the El Niño-Southern Oscillation (ENSO)), and surface temperature over North and South America. ENSO is considered to be a primary driver of surface temperature anomalies in these regions (e.g., Ropelewski and Halpert (1986), Gu and Adler (2011)). However, on monthly timescales, SST anomalies are quite persistent—the 1 month lag autocorrelation of the Niño 3.4 SST index (anomaly form, with the 1951-2000 mean removed, Rayner et al. (2003)) is 0.91, meaning that over 80% of the variability in tropical Pacific SST in the Niño 3.4 region is determined by the previous month. The Niño 3.4 index takes over 6 months to decorrelate (defined using its e-folding

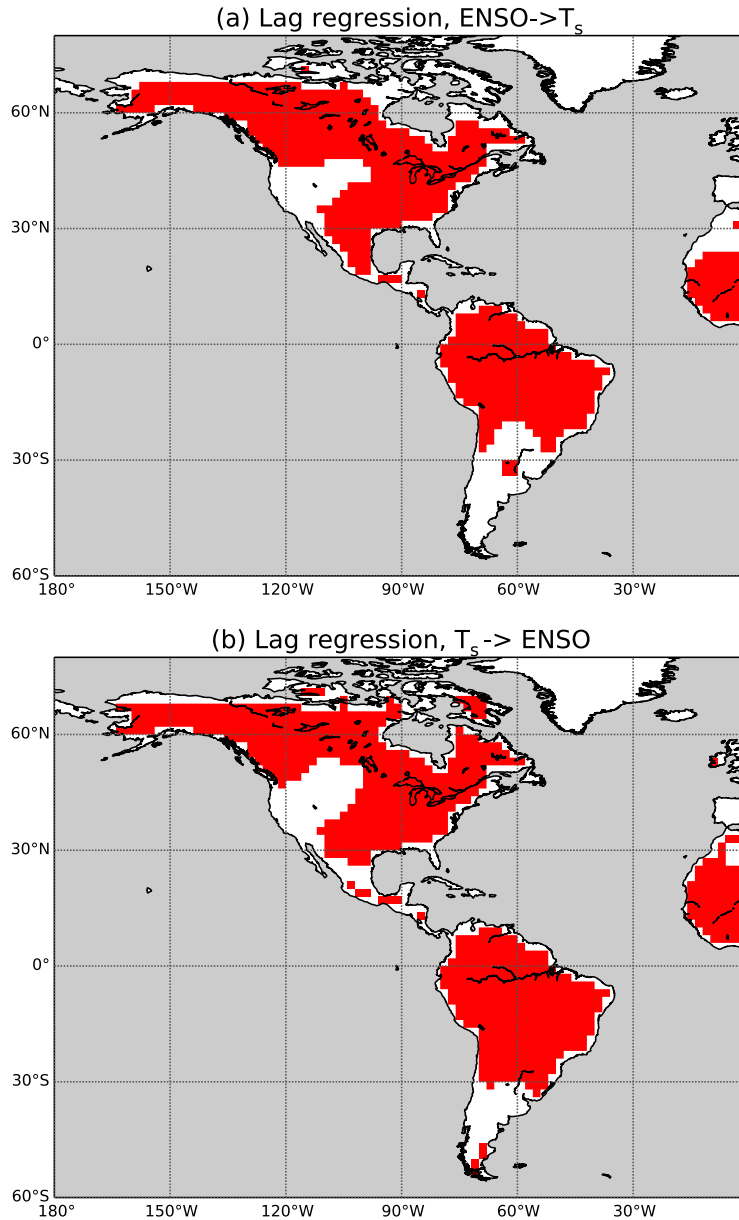


Fig. 2.1. Using lagged regression to test the hypothesis that (a) ENSO drives T_s , and (b) T_s drives ENSO. Red indicates a significant lagged relationship identified at up to 7 months. Significance is assessed at 95% using a 2-sided t -test.

time). This memory in ENSO can lead to ambiguity when applying lagged linear regression. For example, Figure 2.1 shows the lagged relationship between ENSO and land surface temperature (T_s , obtained from the NOAA-CIRES 20th Century Reanalysis Project (Compo et al. (2011)), with mean and second-order trend removed) over the Americas. Figure 2.1a displays the regression of ENSO on T_s at lags of up to of 7 months—that is, the red shading in Figure 2.1a indicates gridpoints

for which there is a significant lagged relationship between T_s and ENSO up to 7 months prior (refer to section 2 for details on determining a significant lagged relationship). However, when the regression is performed in the opposite direction—that is, assessing the influence of lagged T_s upon ENSO—Figure 2.1b is nearly identical to Figure 2.1a. One could interpret Figure 2.1b as demonstrating that T_s is driving ENSO up to 7 months in advance, even though it is generally agreed that ENSO drives T_s at these time scales.

Decades of research on ENSO and its impact on surface temperature over the Americas points to ENSO driving surface temperature, not the other way around (e.g., Ropelewski and Halpert (1986), Gu and Adler (2011)). However, that conclusion is not clear from Figure 2.1—the lagged regression results are ambiguous. One potential cause of this ambiguity could be the high autocorrelation in Niño 3.4 index. Instead of asking, “Can we use T_s to predict ENSO?”, we are better off asking, “Does T_s help us predict ENSO **beyond** ENSO’s ability to predict itself?” We propose the use of Granger causality (Granger (1969)) to answer this question, and to address the issue of causality in data with non-zero memory. Granger causality analysis consists of a lagged auto-regression (e.g., a lagged regression of ENSO on itself) compared to a lagged multiple linear regression (e.g., a lagged regression of T_s and ENSO on ENSO), and is only slightly more challenging to implement than a typical lagged regression analysis. As Granger causality accounts for memory in the data by using a lagged autoregression, it is not susceptible to over-reporting of causal relationships with high-memory data, as lagged regression can be. We note that while formal definitions of causality exist as defined by Pearl’s causal theory (Pearl (2009)), and have been more recently introduced into climate science (e.g., Hannart et al. (2016b)), here, we loosely define a “causal relationship” as one that shows a significant lagged relationship between variables. The distinction between Pearl causality and Granger causality is discussed further in Section 5. It is worth noting that, like lagged regression, Granger causality could have difficulty in situations in which there are strong two-way feedbacks occurring on similar timescales; Granger causality is also not applicable in situations in which some additional process not included in the model is driving the modeled processes of interest.

2.2 DEVELOPING THE MONTE CARLO MODEL

Granger causality (Granger (1969)) was first developed as a predictive model in economics. More recently, Granger causality has found applications in climate science such as determining the influence of snow cover and vegetation on surface temperature (e.g., Kaufman et al. (2003)); the impact of sea surface temperature on the North Atlantic Oscillation (e.g., Mosedale et al. (2006)) or on Atlantic hurricane strength (e.g., Elsner (2006), Elsner (2007)); ENSO's impact on the Indian monsoon (e.g., Mohkov et al. (2011)); and in attributing global temperature increases to increases in global atmospheric CO₂ (see Attanasio et al. (2013) and references therein). However, the use of Granger causality remains far behind that of lagged regression. We use a Monte Carlo simulation to demonstrate that Granger causality is straightforward, and, under specific circumstances, is less likely than lagged regression to lead to the inference of causal relationship when there is not one.

We start by creating our driver, D . D is a first-order autoregressive (AR-1), or red-noise, process, defined as,

$$D(t) = \alpha \cdot D(t-1) + [1 - \alpha^2]^{1/2} \epsilon_D(t), \quad (2.1)$$

where α is the lag-1 autocorrelation, ϵ_D is a random value drawn from a standard normal distribution (that is, a standard Gaussian random variable), and thus, D has a variance of one. We use D to create a second time series, our response R . By design, R is simply D lagged by some amount of time, $\tau > 0$, with added Gaussian noise, ϵ_R ,

$$R(t) = D(t - \tau) + \gamma \cdot \epsilon_R(t). \quad (2.2)$$

When γ is small, there is little additional noise added to R , and the lag-1 autocorrelations of R and D are very similar; large values of γ yield a much noisier R with less memory.

We perform a Monte Carlo simulation in which we vary α , γ , and τ . First, we create a D time series with 550 steps following equation 2.1. After discarding the first 50 values of D , we create R following equation 2.2. We perform our regression analysis (discussed in the next section), and repeat this process 5000 times for each combination of α , γ , and τ . We test 20 values of α , ranging from 0 to 1; 20 values of γ , ranging from 0.005 to 15; and 15 of τ , ranging from 1 to 15, to ensure

that our results are robust.

To evaluate the performance of the statistical model, we first perform a traditional lagged regression, where we use our driver, D , to predict our response, R ,

$$R(t) = c_0 + c_1 \cdot D(t-1) + c_2 \cdot D(t-2) + \dots + c_k \cdot D(t-k), \quad (2.3)$$

where k is the maximum lag. The significance of the full model is assessed using a two-sided t -test. In all situations, significance is assessed at 95% confidence.

As an alternative to lagged regression, we use Granger causality. Mathematically, establishing Granger causality consists of two regressions—a lagged autoregression of the predictand, R ,

$$R(t) = c_0 + c_1 \cdot R(t-1) + c_2 \cdot R(t-2) + \dots + c_k \cdot R(t-k), \quad (2.4)$$

and a multiple linear lagged regression including information about both the predictand, R , and the predictor (hereafter, D),

$$R(t) = a_0 + a_1 \cdot R(t-1) + \dots + a_k \cdot R(t-k) + b_1 \cdot D(t-1) + \dots + b_k \cdot D(t-k), \quad (2.5)$$

The variance explained of R as determined by equation 2.4 is compared to the variance explained of R as determined by equation 2.5. If the multiple linear lagged regression (equation 2.5) explains significantly more variance in R than the autoregression (equation 2.4), it is said that D Granger-causes R . Significance is assessed using a two-step process:

- (1) At least one value of b must be significant according to a two-sided t -test.
- (2) All values of b collectively must increase the variance explained by the regression according to an F -test.

For both the standard lagged regression and the Granger causality analysis, we perform the regressions in both directions—the direction we know to be correct (D driving R), and the direction we know to be incorrect (R driving D). In this way, we can evaluate whether or not Granger causality outperforms standard lagged regression, as defined by a lower risk of false detection given the same identification rate of correct relationships. It is also worth noting that selecting the maximum

lag, k , is an important and potentially challenging part of Granger causality analysis. Typically, k is selected based on a common metric for model selection such as the Akaike information criterion or the Bayesian, or Schwarz, information criterion (e.g., Mosedale et al. (2006)). In both cases, the preferred model is the one with the k value that minimizes the selection criteria and thus limits the model from becoming overfitted. Finally, the approach that we detail here is a relatively straightforward approach to Granger causality that has been used in climate sciences in recent years to great success; it is worth noting, however, that there are alternative ways of calculating Granger causality, many of which have been developed in neuroscience (e.g., Barnett and Seth. (2014), Stokes and Purdon (2017)).

2.3 MONTE CARLO MODEL RESULTS

First, we compare the performance of lagged regression and Granger causality by evaluating the ability of D to predict R . Recall that R was created using D , so our models should suggest a causal relationship. Figure 2.2 shows the percentage of significant results (e.g., the model reports a significant causal relationship for the hypothesis that D drives R at 95%) as a function of memory (α , y-axis) and noise in R (γ , x-axis) for the lagged regression model (Figure 2.2a, top) and the Granger causality model (Figure 2.2b, bottom). Darker colors imply that the model indicated a causal result (in this case, D causes R) more often. Both panels of Figure 2.2 look similar—in this case, lagged regression and Granger causality yield comparable results. Both methods show a dependence on γ —that is, as R becomes noisier, both models are less able to predict R from D . Both methods also exhibit minimal dependence on α , demonstrating that, in general, both models are quite capable of predicting R , even when D has a very high memory. Here, we note that this lack of dependence on α is specific to the AR-1 process modeled in equation 2.1, where the variance of the noise (the $\epsilon_D(t)$ term) is standardized. For the more general case where the variance of D is not equal to one, the ability of D to predict R does show a dependence on α , with larger values of α showing an increased ability to correctly identify that D drives R at a given value of γ . This effect occurs for both the lagged linear regression and Granger causality approaches. Thus, even for a more general model of red noise, both methods—lagged regression and Granger causality—yield

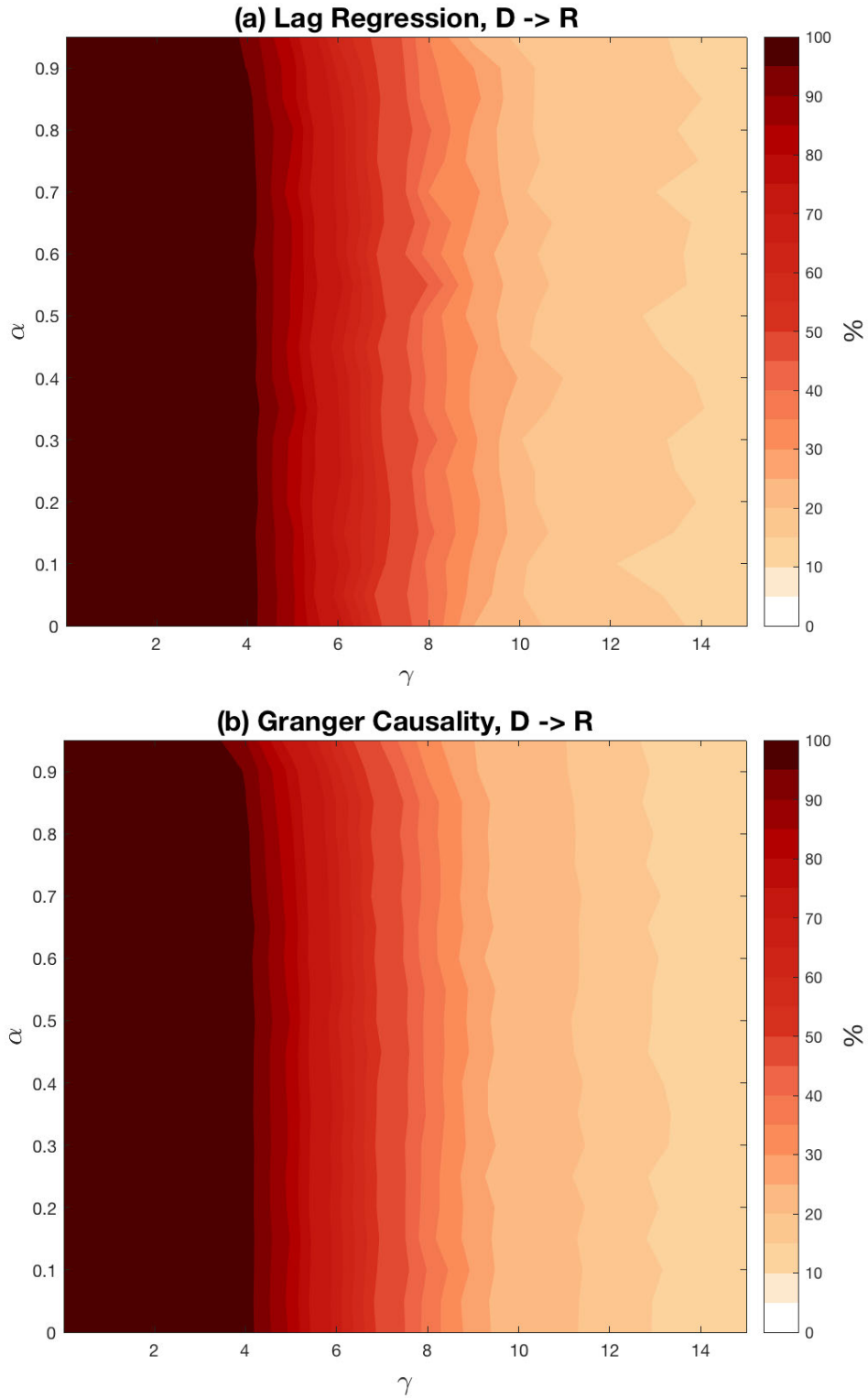


Fig. 2.2. Testing the hypothesis that D drives R using (a) lagged regression, and (b) Granger causality. Shading indicates percentage of significant results at 95% confidence.

results that are similar to each other, and either could be used in analyzing the hypothesis that D drives R .

While Figure 2.2 demonstrates that lagged regression and Granger causality generally yield similar results in the case of D driving R , there is one notable exception: when memory is very high ($\alpha \geq 0.8$), and noise is moderate ($\gamma > 2$). In this small region, Granger causality exhibits a slightly higher failure rate than lagged regression, as seen by the slight curve near the top of Figure 2.2b. This difference between Figure 2.2a and Figure 2.2b can be explained by the fact that Granger causality evaluates **added** variance explained—that is, the variance explained **beyond** what is explained by the autocorrelation of R . If the autocorrelation of D is very high, then R will have a similar autocorrelation and similar values if the noise is moderate. In this case, R has little to add beyond what is already contained in the past values of D , and thus, Granger causality will not indicate a significant causal relationship between R and D while lagged regression will. It is worth noting that this effect is only seen for a small subset of the Monte Carlo simulations with large memory and moderate noise, that the Granger causality model still confirms the hypothesis that D drives R at a rate of at least 70%, and that this effect is less severe as sample size is increased. Outside of this small region, lagged regression and Granger causality perform very similarly.

Next, we evaluate lagged regression and Granger causality by using R to predict D . That is, we compare the outcomes of the two methods when we look for causality in the wrong direction (recall that R was created from D). In this case, we would hope that the models do not suggest a causal relationship between R and D . This hypothesis of R driving D is tested in Figure 2.3. Figure 2.3 is laid out similarly to Figure 2.2, with darker colors indicating that the model reported a causal relationship more frequently. In Figure 2.3, the advantages of Granger causality become apparent. Figure 2.3a shows that the lagged regression model exhibits a strong dependence on α —as D 's memory increases, the lagged regression model is increasingly more likely to suggest that R drives D , which we know to be incorrect. Even at moderate values of α , the lagged regression model implies that there is a causal relationship in the wrong direction. While low values of α show a false positive rate between 5-10% (recall that significance is assessed at 95% confidence, meaning we'd expect a significant result 5% merely by random chance), at $\alpha = 0.5$, the lagged

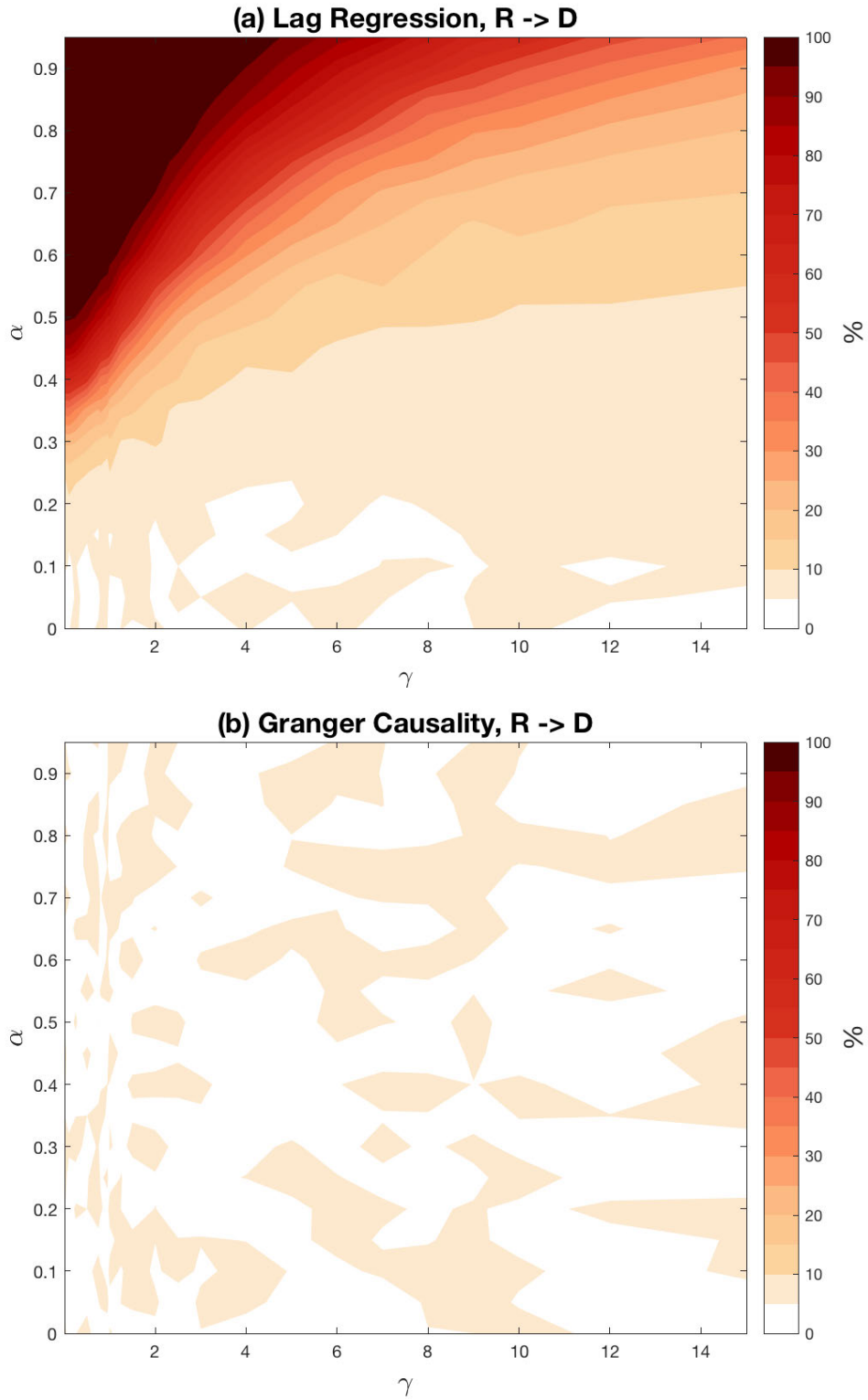


Fig. 2.3. Testing the hypothesis that R drives D using (a) lagged regression, and (b) Granger causality. Shading indicates percentage of significant results at 95% confidence.

regression model indicates that R causes D between 10 and 100% of the time, depending on the noisiness of R . For $\alpha \geq 0.8$, this false positive rate is even higher, suggesting 25% of the time that R causes D for even high values of γ . Figure 2.3a shows only the results for $\tau = 1$ (that is, a lag of 1 time step), but larger lags are qualitatively similar, though moderate values of α become less sensitive at larger lags (for example, at $\tau = 3$, values of $\alpha \leq 0.4$ yield a significant result less than 10% of the time).

There is no such dependence on memory for the Granger causality method, as seen in Figure 2.3b. Indeed, Figure 2.3b indicates that the results of the Granger causality method are simply noise, with Granger causality yielding a significant result about 5% of the time, consistent with our 95% significance testing. These results are not dependent on lag, τ ; memory, α ; or noise in R , γ . In this case, Granger causality's insensitivity to α , or memory in D , shows an improvement over a typical lagged regression model for variables with high memory.

Recall that the one-month autocorrelation of Niño 3.4 is 0.91. Figure 2.3a demonstrates that a lagged regression analysis involving Niño 3.4 could be susceptible to reporting a causal relationship when there is none—the lagged regression analysis is simply picking up the memory (α) in Niño 3.4. Granger causality analysis, on the other hand (as seen in Figure 2.3b), would likely not be susceptible to this problem, as the results of the Granger causality analysis do not depend on α , even when α is very high (see Runge et al. (2014) for a more in-depth discussion of this effect). This will be explored in the following section.

2.4 APPLICATIONS IN CLIMATE VARIABILITY

2.4.1 ENSO and Surface Temperature

We now apply the results of our statistical model to the apparent paradox of Figure 2.1. We know that ENSO's memory is large—do the benefits of Granger causality seen in the statistical model carry over to climate variability problems? This time, we perform lagged regression and Granger causality analysis in both directions—we use ENSO to predict T_s , and T_s to predict ENSO. We focus only on temperatures over land.

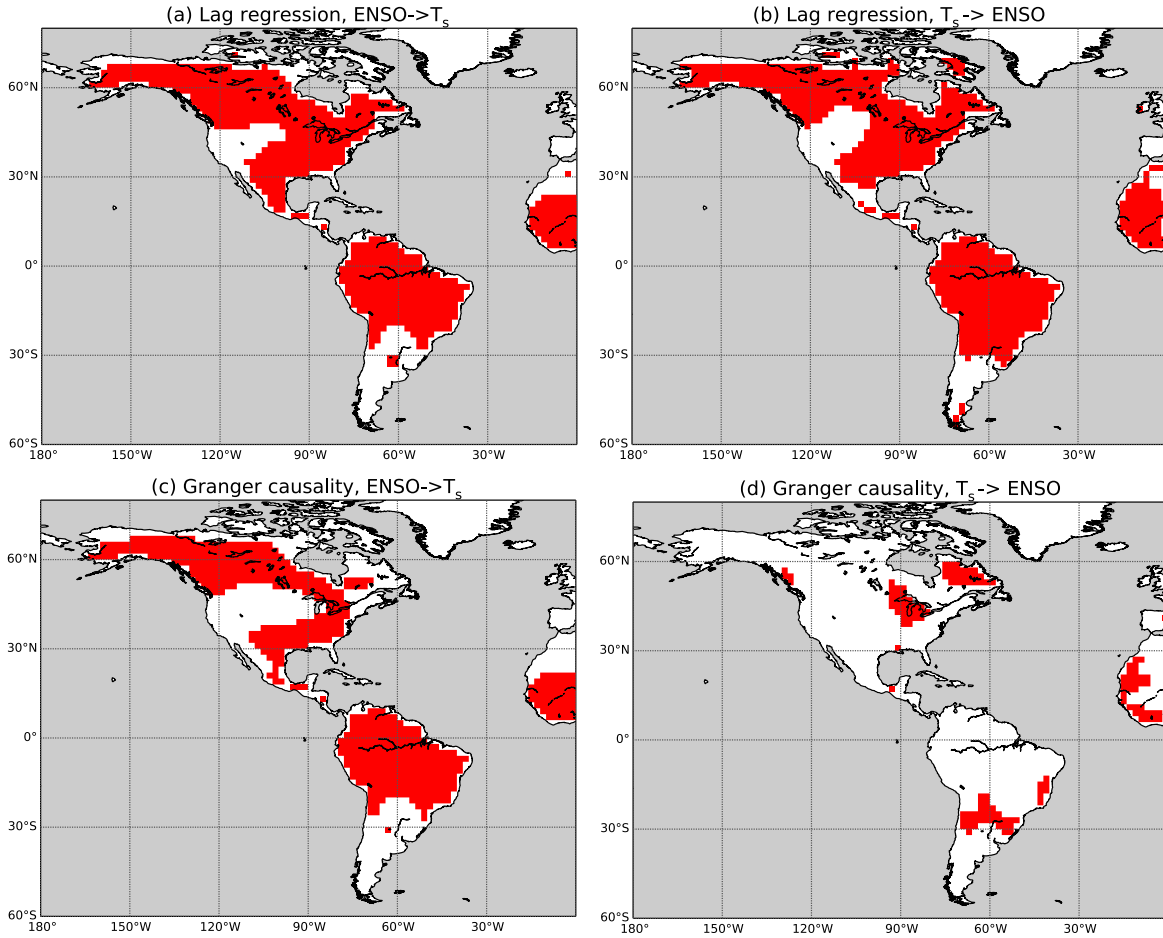


Fig. 2.4. Using (a,b) lagged regression and (c,d) Granger causality to test the hypothesis that (a,c) ENSO drives T_s , and (b,d) T_s drives ENSO. Red indicates a significant lagged relationship identified at up to 7 months ($k = 7$). Significance is assessed at 95%.

Figure 2.4 compares lagged regression (a,b) and Granger causality (c,d) to test the hypothesis that ENSO drives T_s (a,c), and that T_s drives ENSO (b,d). While Figure 2.4 shows only the results for a maximum lag of 7 months ($k = 7$), results from maximum lags of 3 to 9 months ($k = 3$ to $k = 9$) are comparable. Red in Figure 2.4 indicates that a significant lagged relationship is identified for $k = 7$. Red does not convey the magnitude of the relationship; it only indicates whether or not a significant relationship exists at a given gridpoint at 95% confidence. When testing whether or not ENSO drives T_s , Granger causality (Figure 2.4c) and lagged regression (Figure 2.4a) perform similarly—both indicate that ENSO from up to 7 months prior drives T_s over much of North and South America. However, when testing the other direction—that T_s from up to 7 months prior drives ENSO—the two methods yield very different results (Figure 2.4b,d). In this case, the lagged

regression (Figure 2.4b) looks quite similar to the results of the lagged regression testing whether or not ENSO drives T_s (Figure 2.4a). Since we know that the autocorrelation of ENSO is very high, it seems unlikely that T_s is exerting such a strong influence on ENSO at lags of 7 months; it is more likely that the results of Figure 2.4b are due, at least in part, to the high autocorrelation of ENSO. Granger causality does account for the memory in ENSO, and shows that T_s over North and South America up to 7 months prior has little influence on ENSO (Figure 2.4d). Put another way, Granger causality asks, “what is the variance in ENSO due to T_s not already accounted for by ENSO itself?”—therefore, since most of the variance in ENSO is explained by past values of ENSO, Granger causality does not report that T_s causes ENSO.

Since ENSO dynamics and teleconnections have been well-studied and largely understood for decades, climate scientists are unlikely to misinterpret Figure 2.4b. The memories of the two variables are vastly different, and the ENSO- T_s relationship is fairly well-known. However, in cases where the dynamics are not as well-understood, Granger causality analysis could provide valuable insights beyond that of traditional lagged regression.

2.4.2 Arctic-Midlatitude Connections—Another Example

Finally, we use Granger causality analysis and lagged regression to investigate the relationship between Arctic temperature and low-level winds across the mid-to-high latitudes. The topic of the impact of Arctic warming on midlatitude weather and climate is one of much scientific discussion and debate (e.g., Walsh (2014), Barnes and Screen (2015) and references therein). However, the direction of the causality of this Arctic-midlatitude relationship is not clear—how much does the Arctic temperature drive midlatitude weather, and how much does midlatitude weather drive changes in Arctic temperature? We do not fully address these questions here—we simply seek to point out that Granger causality can provide information about the direction(s) of causal relationships that cannot be determined from traditional lagged regression.

To analyze the relationship between Arctic temperature and low-level winds, we define Arctic temperature (T_{pol}) as a vertically-weighted average of 1000-700 hPa temperature from 70-90°N.

Low-level zonal winds ($U700$) are evaluated on the 700 hPa surface throughout the Northern Hemisphere. Both T_{pol} and $U700$ are calculated using daily means of 6-hourly data from the MERRA2 reanalysis data on 0.625° by 0.5° spatial grid (GMAO (2015)). The seasonal cycle and second-order trends are removed from both T_{pol} and $U700$. T_{pol} and $U700$ are then averaged into 5-day means in order to low-pass filter the data and focus on subseasonal variability rather than individual synoptic events. Lagged regression and Granger causality analysis are performed for maximum lags spanning 5 to 30 days ($k = 1, \dots, 6$); we focus on a subseasonal timescale of 25 days ($k = 5$), but results are similar for maximum lags of 5-30 days. Here, we focus solely on the annual mean; the impacts of seasonality will be discussed in a later study.

Figure 2.5 displays the results of lagged (a,b) and Granger (c,d) regression analysis for T_{pol} and $U700$ at a maximum lag of 25 days ($k = 5$). The left panels (a,c) test the hypothesis that T_{pol} drives $U700$; the right panels (b,d) test the hypothesis that $U700$ drives T_{pol} . Focusing first on the case of T_{pol} driving $U700$ (Figure 2.5 (a,c)), we see that both Granger causality (Figure 2.5c) and lagged regression (Figure 2.5a) show large-scale responses across much of Siberia, Alaska, the Canadian Arctic, and Northern Europe, as well as signals in interior North America and Asia. Lagged regression, however, shows much larger responses over the ocean basins than Granger causality. As the autocorrelation of the ocean is larger than that of the land surface (that is, the ocean has more memory than the land), it is possible that the differences in the response in Figure 2.5a as compared to Figure 2.5c are due to the effect of memory over the oceans. Physically, Figures 2.5a,c imply that Arctic lower-tropospheric temperatures may drive a response in the low-level zonal winds in the sub-Arctic, particularly over northern Europe, Siberia, and northern Canada. This response is consistent with studies that have reported links between Siberian temperature anomalies and snow cover and Arctic amplification and sea ice loss (e.g., Inoue et al. (2012), Ghatak et al. (2012), Cohen et al. (2012), Peings et al. (2013)).

The case of 700 hPa winds driving Arctic temperatures (Figure 2.5(b,d)) presents a somewhat different picture. Again, the lagged regression (Figure 2.5b) shows large-scale responses over much of the Northern Hemisphere—the Atlantic and Pacific storm tracks, much of continental North America, nearly the entire sub-Arctic (poleward of 60°N), most of Europe, and much

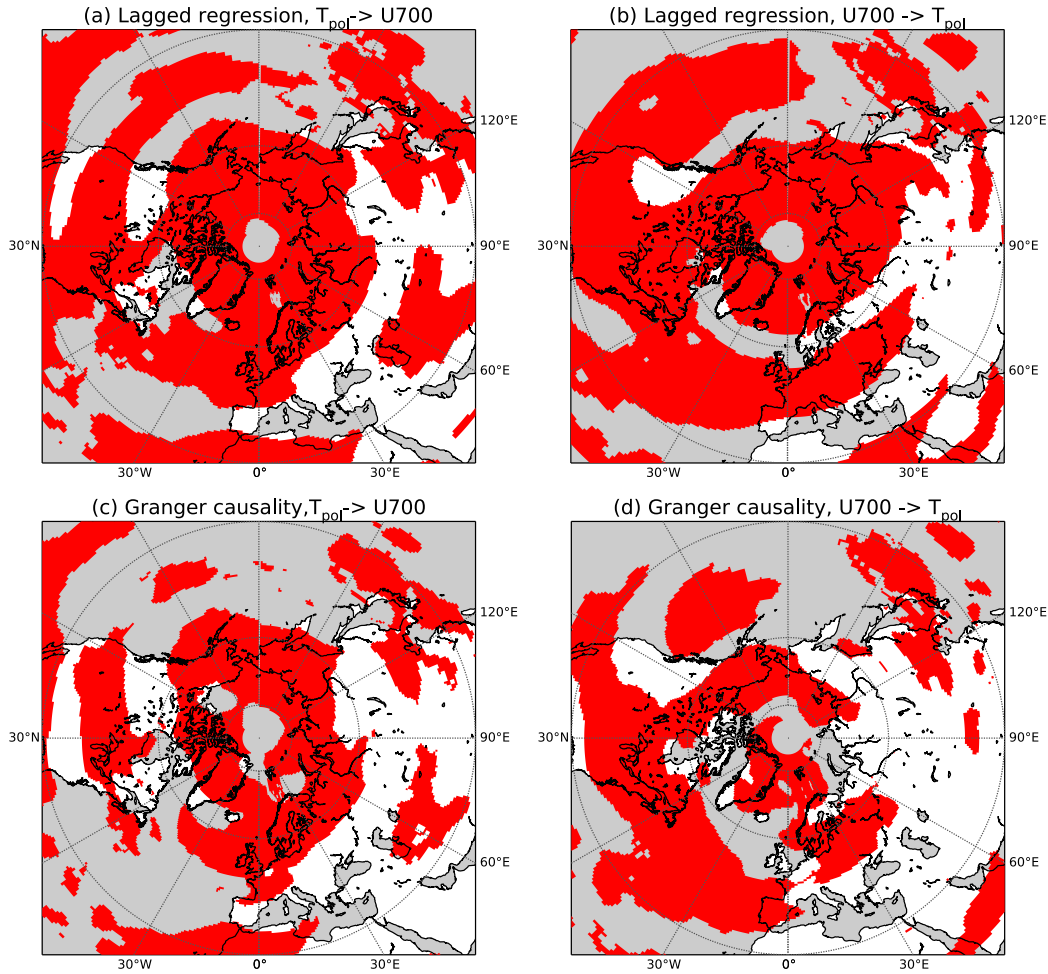


Fig. 2.5. Using (a,b) lagged regression and (c,d) Granger causality to test the hypothesis that (a,c) polar mean temperature drives 700 hPa zonal winds, and (b,d) 700 hPa zonal winds drive polar mean temperature. Red indicates a significant lagged relationship identified at up to 20 days ($k = 4$). Significance is assessed at 95%.

of Siberia. Granger causality analysis (Figure 2.5d) has a more limited large scale response than that given by lagged regression—notably, Granger causality does not show a significant response over Siberia, and shows a weaker, less spatially homogeneous response in the sub-Arctic region when compared to lagged regression. Previous work has linked changes in midlatitude circulation and sea surface temperatures to warmer Arctic temperatures (e.g., Graversen (2006), Screen et al. (2012), Wettstein and Deser (2014), Baggett and Lee (2015)); however, as Figure 2.5 demonstrates, the details of these circulation changes differ with different methodologies.

2.5 DISCUSSION

In this manuscript, we have tried to present a clear, concise, and compelling argument for an increased use of Granger causality analysis in climate variability studies. We have emphasized Granger causality's superior performance as compared to lagged regression in situations in which one or more variables has substantial memory. However, like any approach, Granger causality analysis has its own limitations. One obvious drawback is the possibility of a confounding variable—that is, an additional process or variable could be driving the modeled variables (for example, in the bivariate case, a third process, Z , could influence the independent (X) and dependent (Y) variables— $Z \rightarrow X, Z \rightarrow Y$). Using the bivariate case as an example, Granger causality may state that X causes Y , even though Z actually drives both X and Y . Similarly, Granger causality does not account for indirect effects, or mediating variables. Returning to the bivariate example, a process X may indirectly drive Y via a third process, Z ($X \rightarrow Z \rightarrow Y$). Again, Granger causality may state that X drives Y without including the necessary link, Z . As discussed here, basic Granger causality analysis also requires assumptions of linear and stationary processes. An out-of-sample approach to Granger causality tests (e.g., Attanasio et al. (2012), Pasini et al. (2012), Attanasio et al. (2013)) provides a framework for applying Granger causality to non-stationary processes. Cointegration (e.g., Johansen and Juselius (1990), Kaufmann and Stern (2002)) is another approach to analyzing causality in non-stationary processes that tend to vary together and have stochastic trends.

Moreover, Granger causality is simply one approach to causal analysis. Granger causality provides an opportunity for incremental improvement to the already-extant lagged regression analysis framework that has gained so much traction in climate variability studies. Multiple regression-based approaches such as vector autoregressive (VAR) models have built upon this Granger causality approach and have been applied to climate variability studies focused on the influence of sea ice on midlatitude circulation (e.g., Strong et al. (2009), Matthewman and Magnusdottir (2011)), intraseasonal variability of sea ice (e.g., Wang et al. (2016)), paleoclimate data (Davidson et al. (2016)), and the relationship between the North Atlantic Oscillation and North Atlantic sea surface temperatures (e.g., Wang et al. (2004)).

Even more recently, probabilistic graphical models based on Pearl causality have been introduced to climate science, and represent the current state of the art in causal detection theory (see Ebert-Uphoff and Deng (2012) for a thorough introduction of graphical models in climate research). This graphical approach to causality was first proposed in the 1980s (e.g., Rebane and Pearl (1987a), Pearl (1988)), and has since been refined and further developed. (e.g., Spirtes et al. (1991)). Granger causality has in fact been incorporated into these graphical models, creating an approach known as graphical Granger models (e.g., Arnold et al. (2007)). Ebert-Uphoff and Deng (2012) and Runge et al. (2014) have demonstrated the utility of these graphical approaches to causality in climate science, and we encourage readers to refer to these papers for more thorough discussions of these graphical models and their advantages in climate variability studies. While lagged regression is a straightforward, popular, and often effective analysis technique in climate variability studies, it is vulnerable to overstating causal relationships in situations in which one or more data sets has significant memory (e.g., Runge et al. (2014)). We use a Monte Carlo model to demonstrate that:

- (1) Granger causality outperforms (that is, lowers the risk of false detection) lagged linear regression when one or more variables has substantial memory;
- (2) Granger causality and lagged linear regression yield similar results when there is a true causal relationship between the variables (except in the case of very high autocorrelation);
- (3) Granger causality analysis is only slightly more challenging to implement than traditional lagged linear regression analysis, as it simply consists of a lagged autoregression and a lagged multiple linear regression.

These general differences between lagged regression and Granger causality are also shown to be relevant for two large-scale climate dynamics examples, demonstrating that Granger causality analysis has useful and viable applications in climate variability studies.

Sincere thanks to Greg Herman, Thomas Birner, Eric Maloney, David Thompson, and Lauren McGough for their suggestions and feedback regarding this work. Many thanks also to the three anonymous reviewers and the editor, whose thorough reviews have greatly strengthened this work. The MERRA-2 data used in this study have been provided by the Global Modeling and Assimilation Office (GMAO) at NASA Goddard Space Flight Center. MCM and EAB are supported by the National Science Foundation under Grant AGS-1545675.

3 Granger and Pearl Causality Models for Climate Science¹

This chapter provides an overview of the graphical methods that are used in this chapter and Chapter 4. It then discusses three analysis approaches—vector autoregression (VAR), regularized regression (the LASSO method), and a method based on causal calculus (the PC algorithm)—and their implementation in some detail. These three methods are then used to study the sub-monthly relationships between the Arctic and the midlatitude jet streams. Ultimately, several feedback loops between the Arctic and the jet streams are identified. An anomalously strong jet in the North Pacific drives warm Arctic temperature anomalies, which further reinforce the strong jet anomalies; in the North Atlantic, the opposite relationship was identified, where weak jet anomalies reinforce warm Arctic temperatures. Similarly, an anomalously equatorward jet in the North Pacific drives warm Arctic anomalies, which reinforce the jet position anomalies.

3.1 INTERVENTION AND AN OVERVIEW OF GRAPHICAL METHODS

Probabilistic graphical models are a compact and visual representation of relationships between variables, and illustrate the relationships that are modeled by causal calculus (e.g., Rebane and Pearl (1987b), Pearl (1988)). Ebert-Uphoff and Deng (2012) provide an excellent overview of probabilistic graphical models and causal discovery aimed at climate scientists; a very basic overview will be provided here, but interested parties should consult Ebert-Uphoff and Deng (2012) for a more thorough exploration of this topic. A graph is made up of *nodes*, which represent the variables of interest, and *edges*, which connect nodes. *Directed* graphs are graphs whose edges have unique directions, while *undirected* graphs have directionless edges. *Acyclic* graphs do not contain any cycles—that is, one cannot start at a node, follow the directions of the edges, and return to that same node. *Cyclic* graphs, on the other hand, do contain cycles. In an undirected graph, nodes that share edges are considered *neighbors*. In a directed graph, if the arrow points

¹This chapter contains material that has been published in *Environmetrics* as: Samarasinghe, S., M. McGraw, E. A. Barnes, and I. Ebert-Uphoff: A study of links between the Arctic and the midlatitude jet-stream using Granger and Pearl causality. *Environmetrics*, e2540, <https://doi.org/10.1002/env.2540>.

from a to b , a is a *parent* of b , while b is a *child* of a . Figure 3.1 shows an example of a directed, acyclic graph. a , b , c , and d are nodes; a is a parent of b and c , and c is a parent of d .

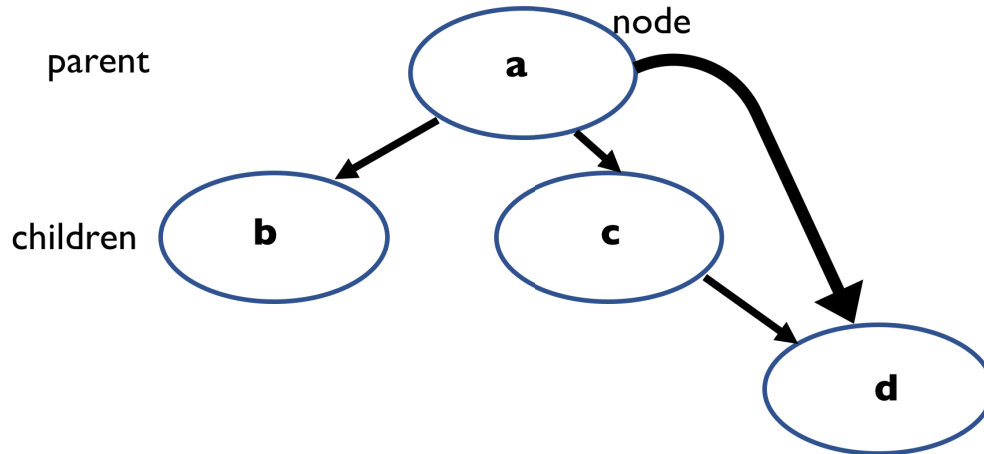


Fig. 3.1. Example of a directed, acyclic graph.

Cause-effect relationships are typically investigated using two different types of causal analysis—observational analysis and intervention analysis. True intervention analysis (e.g., Pearl (1988, 2000); Spirtes et al. (2000)) stems from causal calculus (Rebane and Pearl (1987b)). Intervention analysis can be used to definitively prove or disprove causal relationships, but it requires the ability to actually perform interventions in the system of interest—that is, the investigators must be able to change the state of a given variable, and observe how that change impacts other variables. These interventions are challenging to perform in climate science, requiring the use of dynamical models and specific, well-constrained experimental designs (e.g., Hannart et al. (2016a)). So, while well-designed modeling experiments can truly intervene in the earth’s climate system, studies using observations, reanalysis data, or output from fully coupled climate models cannot perform true intervention analysis. In this dissertation, we focus solely on an observational-type analysis, where we study causal relationships using reanalysis and climate model output from simulations that have already been performed. However, we can still use the graphical modeling framework from Pearl (1988).

In causal analysis, we are often interested in *necessary* and *sufficient* conditions. Some process a may be required for b to happen, but other processes may also be required for b to happen—this

means that a is a *necessary* condition for b . For a to be a sufficient condition for b , a would always drive b by itself, but other factors could also drive b . Often, these other factors are *hidden common causes*, or *latent variables*. For example, consider a system in which two variables, b and c , appear to be related solely because some third variable, z , impacts both of them; in this situation, z would be the latent variable, or hidden common cause. A true intervention analysis could correctly identify the presence of z and conclude that b and c are not directly connected, while an observational analysis may not be able to identify that relationship. For example, in Figure 3.2, an observational analysis (Figure 3.2a), may incorrectly identify a causal relationship between b and c , while failing to identify a hidden common cause, z . A true intervention analysis, on the other hand, should be able to identify the latent variable, z , that drives both b and c , while also correctly recognizing that c does not drive b .

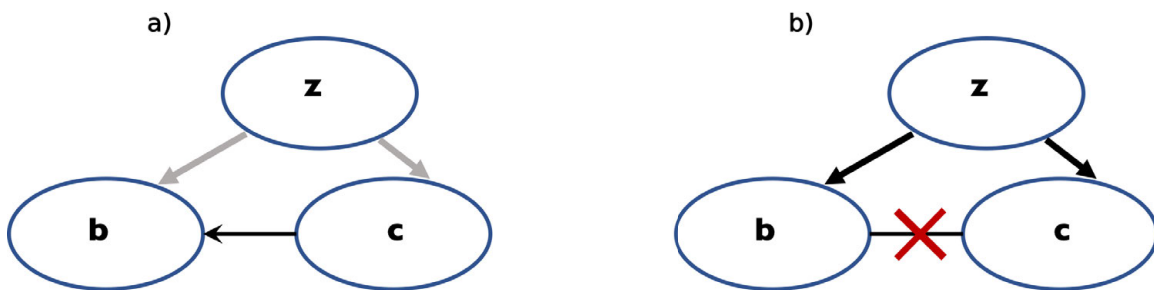


Fig. 3.2. Example of a graph with hidden common causes. In a), an observational analysis fails to identify the hidden common cause, z , that drives both b and c ; it instead incorrectly assumes that c drives b . In b), an intervention analysis does correctly identify the hidden common cause, z , while also correctly recognizing that c is not a driver of b .

We use methods formulated in two different causality frameworks—Granger causality and Pearl causality. Granger causality, as discussed in the previous section, is based on predictability. A variable, X is said to Granger-cause another, Y if past values of X provide additional information about the present state of Y *beyond Y 's ability to predict itself*. If the inclusion of X significantly improves the prediction of Y , X can be said to Granger-cause Y . We build upon our Granger causality model described in Chapter 2 by extending it to a vector autoregression (VAR) model, which will be discussed in Section 3.2; modifications to this model will be discussed in Section 3.3. A more in-depth discussion of Pearl causality and the PC-stable method can be found in Section 3.4.

3.2 VECTOR AUTOREGRESSION (VAR) MODEL

Vector autoregression (VAR) is a regression model that performs a multivariate regression on many variables with declaring explicit predictors or predictands. That is, all variables are treated the same way. A p -th order VAR model estimates $\mathbf{z}_t \in \mathbb{R}^k$ (all variables of interest, \mathbf{z}_t are contained in \mathbb{R}^k). $\mathbf{z}_t \in \mathbb{R}^k$ is calculated in terms of its p lags,

$$\mathbf{z}_t = \mathbf{c} + \mathbf{A}_1 \mathbf{z}_{t-1} + \dots + \mathbf{A}_p \mathbf{z}_{t-p} + \mathbf{e}_t \quad \text{for } t = (p+1), \dots, T, \quad (3.1)$$

where:

- vector $\mathbf{z}_t = [z_{1t}, \dots, z_{kt}]'$ contains the values of k considered variables at time t ;
- $\mathbf{c} = [c_1, \dots, c_k]'$ contains the model intercepts;
- \mathbf{A}_i are the $(k \times k)$ coefficient matrices (for $i = 1, \dots, p$);
- and $\mathbf{e}_t = [e_{1t}, \dots, e_{kt}]'$ is the vector containing the residual terms.

The error terms are assumed to be independent, to be identically distributed with $E[\mathbf{e}_t] = 0$, and to have a non-singular covariance matrix of the form $E[\mathbf{e}_t \mathbf{e}_t'] = \Sigma_e$. If we want to analyze the relationships between two univariate time series X and Y , we simply set $k = 2$, and define $\mathbf{z}_t = [x_t, y_t]'$. We note here that in this model, we do *not* permit instantaneous connections between variables.

We solve Equation 3.1 and estimate its parameters (\mathbf{c} and \mathbf{A}_i) with an ordinary least-squares approach (e.g., Lütkepohl (2007)). Once we obtain a model in the form of Equation 3.1, we can validate the model by ensuring its stability, and by extension, its stationarity. That is, we check that all roots of the characteristic polynomial lie outside the complex unit circle (see Lütkepohl (2007), Pfaff et al. (2008) for a more thorough discussion of this process). We derive a VAR model for several different values of p , and select the best value of p using a selection criterion such as the Akaike information criterion (AIC) or the Bayesian information criterion (BIC) (e.g., Ivanov and Kilian (2005); Lütkepohl (2007); Nicholson et al. (2017)).

The selection of a model order (that is, a maximum lag) is an important aspect of creating a VAR model. Selecting p necessitates a trade off between a value of p that is large enough

to account for all of the physically relevant relationships, but small enough to yield an easily interpretable model. We identify p with both the AIC and the BIC (e.g., Ivanov and Kilian (2005); Lütkepohl (2007); Nicholson et al. (2017)),

$$AIC(p) = \ln \left| \hat{\Sigma}_e^p \right| + \frac{2k^2p}{N}, \quad (3.2)$$

$$BIC(p) = \ln \left| \hat{\Sigma}_e^p \right| + \frac{\ln N k^2 p}{N}, \quad (3.3)$$

where k indicates the number of variables, N is the effective sample size, and $|\hat{\Sigma}_e^p|$ is the determinant of the estimated error covariance matrix. This term accounts for the accuracy of the different models at different values of p . The second term ($\frac{2k^2p}{N}$ in Equation 3.2, $\frac{\ln N k^2 p}{N}$ in Equation 3.3) penalizes the model based on the number of parameters it needs to estimate. The best value of p corresponds with the lowest AIC/BIC. Overall, the formulae for AIC and BIC are quite similar, with the only difference being the second term ($2k^2p$ versus $\ln N \cdot k^2p$). Both provide a means for model selection and balance the risks of overfitting and underfitting. Theoretically, the AIC estimates the distance between the “true“ model (unknown) and the fitted model, while the BIC essentially estimates the posterior probability of a model being true. In both cases, a lower AIC/BIC is more likely to be a true model. The AIC (blue) and BIC (orange) for estimates of $p = 1, \dots, 10$ can be seen in Figure 3.3, with Figure 3.3a showing the estimates for Arctic temperature (\mathcal{T}) and jet speed (\mathcal{S}), and Figure 3.3b showing the estimates for Arctic temperature (\mathcal{T}) and jet position (\mathcal{L}).

Note that in Figure 3.3, the magnitude of AIC for a given value of p is always larger than that of BIC. In practice, the BIC imposes a larger penalty on a more complex model ($\ln N \cdot k^2p$ in BIC, versus $2k^2p$ in AIC); this means that there are occasions where AIC might choose a higher value of p than BIC. Conversely, while BIC is unlikely to choose a model whose order is too high, it is more likely to choose a model order that is too small. When the main objective in model selection is to minimize the likelihood of a false negative, AIC is preferable; if the main objective is to minimize the probability of a false positive, BIC is preferable. In many situations, AIC and BIC can be used together, providing a narrow range of acceptable values for p . Based on Figure 3.3, we see that AIC and BIC are both minimized for values of p between 3 and 5. We select $p = 5$ for both models, as $p = 5$ will give us a desirable model based on AIC/BIC, and will also allow us to

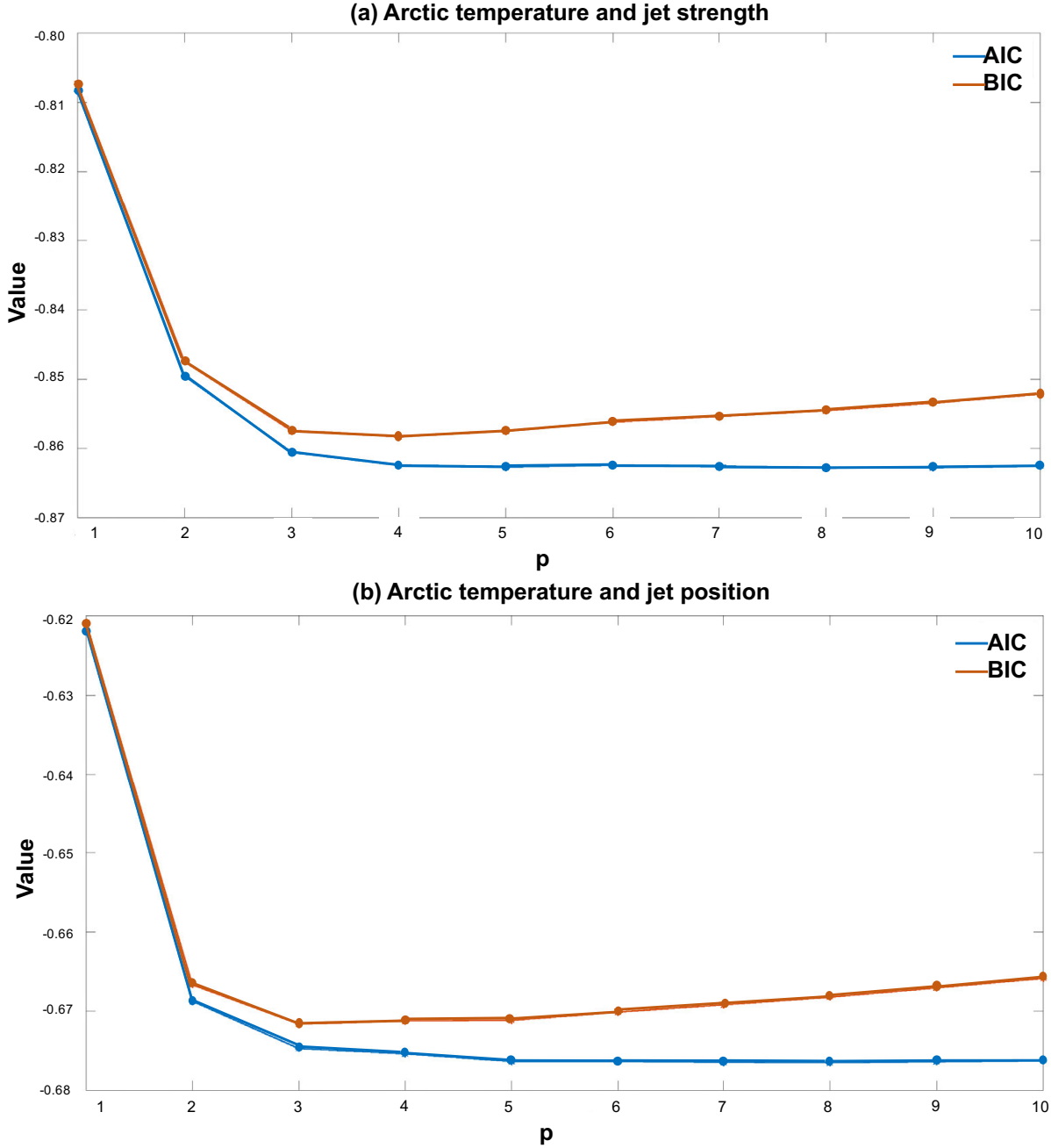


Fig. 3.3. AIC (blue) and BIC (orange) values for VAR models of varying p between (a) Arctic temperature (\mathcal{T}) and jet speed (\mathcal{S}), and (b) Arctic temperature (\mathcal{T}) and jet position (\mathcal{L}).

explore a slightly greater range of lags.

We can assess the physical system described by the VAR model for Granger causality via inspection of the coefficients in \mathbf{A}_i . Assume that a_{lm}^i is the element of row l and column m of matrix \mathbf{A}_i . The time series $\{z_{l,t}\}$ denotes the l th variable without a lag, while $\{z_{m,t-i}\}$ indicates the

m th variable with lag i . Thus, a_{lm}^i denotes the effect of $\{z_{m,t-i}\}$ on $\{z_{l,t}\}$. For normalized data, a_{lm}^i indicates the amount of change to expect in $\{z_{l,t}\}$ for a change of one standard deviation of $\{z_{m,t-i}\}$. For $l \neq m$, $\{z_{m,t-i}\}$ is a useful predictor of $\{z_{l,t}\}$, if and only if $a_{lm}^i \neq 0$. Thus, the m th variable, $\{z_m\}$, can be considered a *Granger-cause* of the l th variable, $\{z_l\}$, if and only if at least one of the coefficients $a_{lm}^i \neq 0$ for any lag $i = 1, \dots, p$.

One practical consideration for a VAR model is the fact that many coefficients may be very close to, but not exactly zero, due to noise. If the system is well-known and a natural threshold for the magnitudes of the coefficients can be easily defined, this can be a reasonable approach; however, typically, a user-defined threshold is required, which can be highly sensitive and subjective. A regularized regression approach such as the one discussed in the next section can combat the sensitivity of using a user-defined threshold, while also helping to eliminate (that is, set to zero), non-essential regression coefficients.

3.3 REGULARIZED REGRESSION MODEL (LASSO)

A regularized regression approach can be used to obtain a sparse model that consists of the subset of predictors that have the strongest impact on the predictability of the responses. Here, we use the Least Absolute Shrinkage and Selection Operator, or LASSO, approach (Tibshirani (1996); Hastie et al. (2015); Nicholson et al. (2017)). LASSO finds a least squares solution that is subjected to an ℓ_1 norm constraint on the coefficients. This ℓ_1 norm constraint imposes a bound on the sum of the absolute values of the coefficients, while also shrinking the overall values of the regression coefficients (the mathematics of this ℓ_1 norm constraint will be discussed in more detail in the following paragraphs). The LASSO approach sets many coefficients exactly to zero to obtain a more generalized and sparse solution—that is, coefficients are either non-zero (significant) or exactly zero (not significant). Thus, a LASSO model results in a model of the exact same form as Equation 3.1, but with many of the coefficients set to exactly zero. Setting many of the coefficients to zero makes the model more interpretable, especially when the number of predictors is large, and makes it easier to identify Granger-causal relationships. A regularized model such as a LASSO model also shows improved prediction accuracy compared to the ordinary least-squares solution,

as it reduces the likelihood of overfitting the model (Tibshirani (1996)).

Consider a simple linear regression model,

$$\mathbf{Y} = \mathbf{X}\beta^0 + \epsilon, \quad (3.4)$$

where $\mathbf{Y} \in \mathbb{R}^n$ is the vector of predictands contained in \mathbb{R}^n (z_t in Equation 3.1); $\mathbf{X} \in \mathbb{R}^{n \times p}$ is the design matrix that contains the model intercepts (\mathbf{c} in Equation 3.1) and the predictors; $\beta^0 \in \mathbb{R}^p$ is a vector containing the true regression coefficients; and ϵ is the error vector. When $p > n$ (we have more predictors than predictands, i.e., we use many lagged variables to predict the present), our system is underdetermined, meaning it has no unique solutions. In order to find the correct solution on an underdetermined system in Equation 3.4, we must imply additional constraints. One possible constraint is that we assume that β^0 is sparse,

$$\min_{\beta \in \mathbb{R}^p} \|\beta\|_0 \text{ such that } \mathbf{Y} = \mathbf{X}\beta, \quad (3.5)$$

that is, we want to find a solution to Equation 3.4 that sets as many entries in β^0 to zero as possible (the ℓ^0 -norm constraint). Equation 3.5 represents the best subset selection; however, solving Equation 3.5 can also be computationally intensive. The ℓ^1 -norm, given as,

$$\|\beta\|_1 = \sum |\beta_j|, \quad (3.6)$$

can be used instead. The ℓ^1 -norm when applied to vectors or matrices is referred to as the sum of absolute differences, or SAD,

$$SAD(\mathbf{x}, \mathbf{y}) = \|\mathbf{x} - \mathbf{y}\|_1 = \sum |\mathbf{x}_i - \mathbf{y}_i|, \quad (3.7)$$

or, when applied to more general scalar differences, it is calculated as the mean-absolute error (MAE),

$$MAE(x_1, x_2) = \frac{1}{n} \|x_1 - x_2\|_1 = \frac{1}{n} \sum |x_{1,i} - x_{2,i}|, \quad (3.8)$$

We also briefly note that the ℓ^2 -norm constraint is even more ubiquitous than the ℓ^0 -norm and ℓ^1 -norm constraints, as the ℓ^2 -norm constraint is the mean-squared error (MSE), or the sum of squared

differences (SSD). For LASSO, we apply an ℓ^1 -norm constraint, meaning we aim to minimize Equation 3.6. Thus, with this in mind, we use the ℓ^1 -norm constraint to help apply a regularization scheme to our ordinary least-squares regression model (Equation 3.1). Following Tibshirani (1996), Hastie et al. (2015), we adjust our ordinary least-squares model with our LASSO estimator, $\hat{\beta}$,

$$\hat{\beta} = \min_{\beta \in \mathbb{R}^k} \left\{ \frac{1}{n} \|\mathbf{Y} - \mathbf{X}\beta\|_2^2 + \lambda \|\beta\|_1 \right\}, \quad (3.9)$$

where $\hat{\beta}$ is the LASSO operator, \mathbf{Y} is the predictand, \mathbf{X} is the predictor, $\|\cdot\|_1$ represents the ℓ^1 -norm, \mathbb{R}^k contains all possible values of β , and λ is our regularization parameter ($\lambda \geq 0$). Put another way, the $\frac{1}{n} \|\mathbf{Y} - \mathbf{X}\beta\|_2^2$ term is what a typical ordinary least squares regression minimizes; the λ term is the penalty term, which is based on the ℓ^1 -norm of our regression coefficients ($\|\beta\|_1$). λ controls the amount of shrinkage applied to the regression model, reducing some of the regression coefficients to be exactly zero. In a LASSO model, the regularization parameter, λ , is what determines the sparsity of the model. When $\lambda = 0$, the LASSO model is equivalent to the ordinary least-squares solution. A large value of λ gives a very sparse solution. The goal of LASSO is the optimal selection of λ . The LASSO estimator seeks to penalize the ordinary least-squares solution according to the operator $\hat{\beta}$. Ideally, λ selection is a tradeoff between a small enough value that all physically relevant relationships are represented in the model, and a large enough value that yields an optimally sparse, easily-interpretable model.

In this study, we use a version of the group LASSO approach. While a standard LASSO approach is often adequate to perform a basic Granger causality analysis, the group LASSO approach (e.g., Hastie et al. (2015); Nicholson et al. (2017)) can be preferable in situations where the predictors show a natural group structure. This natural group structure is often seen in time series data, where past values of a given variable often influence present values of that variable. This approach treats a group of coefficients as a collective entity, and constrains the group, rather than individual coefficients. This approach forces entire groups of coefficients to be zero, rather than individual coefficients. Practically speaking, we can solve our entire model (Equation 3.1) simultaneously, with one value of λ (otherwise, we could have different values of λ for each predictor). This approach also makes it easier to represent our results in a concise, graphical manner. In this

work, the groups are based on the predictor variables (where, following the notation of Equation 3.1, predictor variables = $\{\{z_{m,t-i}\}_{t=p+1}^T \mid i = 1, \dots, p \text{ and } m = 1, \dots, k\}$). The coefficients of any particular predictor are all set to 0 if that predictor does not contribute to the predictability of *any* of the response variables. The specific implementation used here, following the notation of Equation 3.1, solves the optimization problem given in Eq. (3.10), where $a_{\cdot,m}^i$ denotes the m th column in \mathbf{A}_i and $N = (T - p)$ is the effective sample size,

$$\min_{\mathbf{A}, \mathbf{c}} \frac{1}{2N} \sum_{t=p+1}^T \|\mathbf{z}_t - \mathbf{c} - \sum_{i=1}^p \mathbf{A}_i \mathbf{z}_{t-i}\|_2^2 + \lambda \sum_{i=1}^p \sum_{m=1}^k \|a_{\cdot,m}^i\|_2 \quad \lambda \geq 0, \quad (3.10)$$

Equation 3.10 changes the penalty term to be a sum over the ℓ^2 -norms. When each predictor is in its own group, Equation 3.10 reduces to the standard LASSO model (Equation 3.9).

For the analysis that follows, we use the same maximum lag, p , for the LASSO model that we used for the VAR model ($p = 5$). We select λ using a K -fold cross validation scheme, with $K = 10$. The selected value of λ corresponds to the *one-standard-error rule* (e.g., Hastie et al. (2015), Melkumova and Shatskikh (2017)). Figure 3.4 shows the error curves for $K = 10$ for \mathcal{T} and \mathcal{S} (Figure 3.4a) and \mathcal{T} and \mathcal{L} (Figure 3.4b). First, we find the λ that corresponds to the minimum mean squared error of the test data (green lines in Figure 3.4). We then increase the value of λ slightly (that is, we increase the penalty in Equation 3.10), and select the value of λ that corresponds to one standard error above the minimum MSE (blue lines in Figure 3.4). Finally, we note that we also tested our model with an elastic net regularization technique. An elastic net incorporates both ℓ^1 -based (minimizing the mean absolute error) and ℓ^2 -based (minimizing the mean-squared error) constraints, and can sometimes be preferable to LASSO when predictors are highly correlated, as climate variables can be (e.g., Hastie et al. (2015)). We compared our results using both a LASSO model and an elastic net model, and our conclusions remained unchanged.

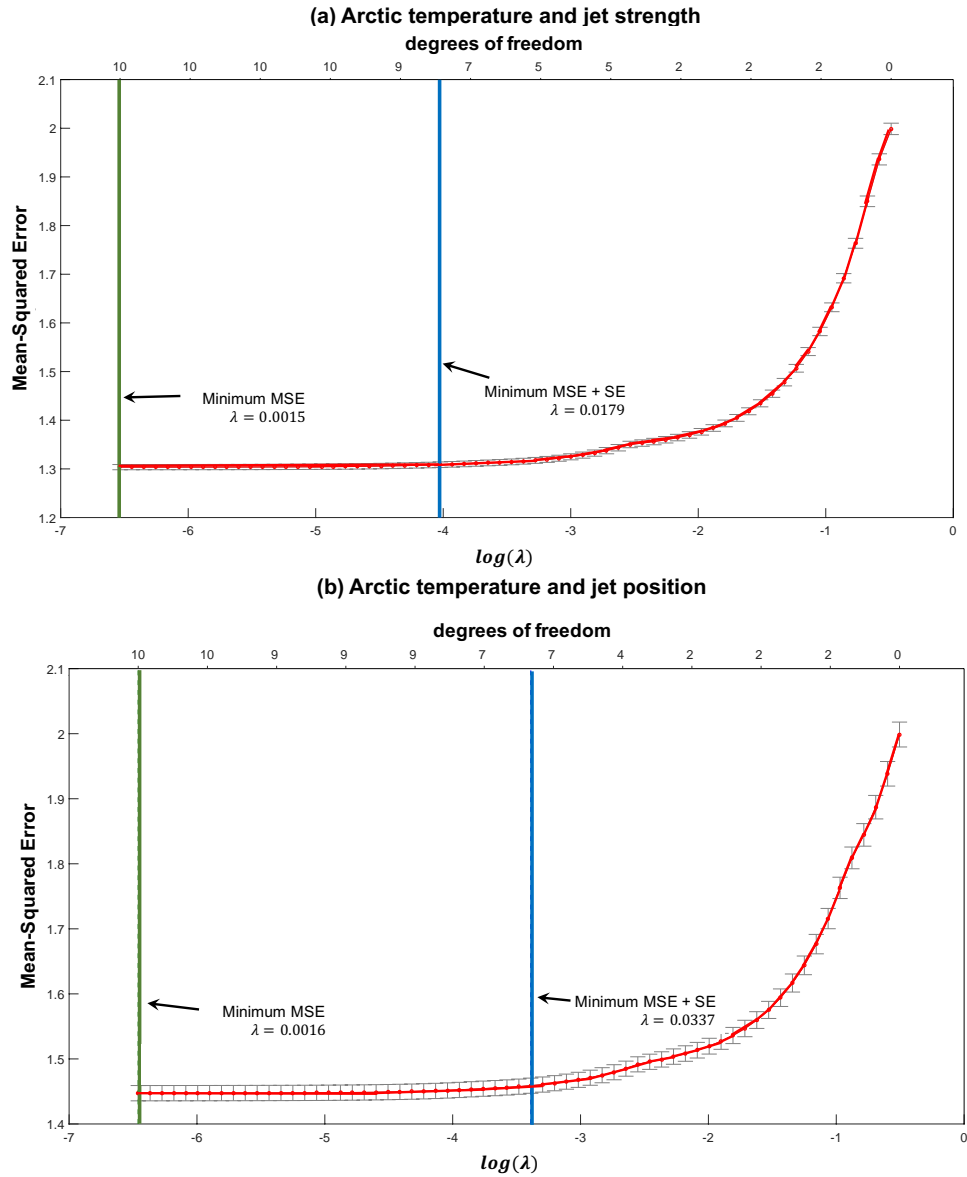


Fig. 3.4. k -folds cross-validation error curves for LASSO for $K = 10$. (a) Arctic temperature (\mathcal{T}) and jet speed (\mathcal{S}), (b) Arctic temperature (\mathcal{T}) and jet position (\mathcal{L}). Degrees of freedom indicates the number of non-zero regression coefficients. Green (blue) lines indicate values of λ that correspond to the minimum mean-squared error (minimum mean-squared error + 1σ).

3.4 PEARL CAUSALITY AND THE PC-STABLE ALGORITHM

The previous two methods—VAR and LASSO—are formulated based on a Granger definition of causality. However, Pearl (1988) describes an alternate framework for causality that is derived from causal calculus (Rebane and Pearl (1987b)). This framework is based on interventions. Where interventions are possible, the Pearl causality framework provides both *sufficient* and *necessary* conditions for causal relationships, allowing one to say with certainty that some variable X is a cause of Y . However, as previously discussed, true intervention is challenging in the field of climate science, and this analysis, like many others, is performed as an observational analysis. Even for observational analyses, Pearl causality can be used to highlight *necessary* conditions for causality—that is, it illuminates which conditions have to be satisfied in order for X to be a possible cause of Y . While we cannot prove causal sufficiency in observational analyses due to the potential effects of hidden common causes, we can still use the necessary condition to eliminate most possible connections. This elimination method assumes that all possible cause-effect connections exist, and then uses conditional independence tests to establish necessary causality and thus delete connections. Figure 3.5 provides an illustrated example of this process. The first part of the process (Figure 3.5a) shows the graph created at the beginning of the analysis—all nodes are assumed to be related to all other nodes. In the second step (Figure 3.5b), conditional independence tests are performed on each connection; relationships that fail this test are considered to be non-causal and are eliminated. In this way, we can reproduce the “true” graph of the system, given in Figure 3.1.

There are many computational algorithms that utilize the approach illustrated in Figure 3.5. The best-known algorithm for this purpose, and the one used here, is the classic *PC* algorithm (Spirtes and Glymour (1991)), named for the first names of the two authors, Peter Spirtes and Clark Glymour. The PC algorithm generally yields a small set of potential cause-effect relationships; the set of *true* causal relationships is a subset of the potential cause-effect relationships. This approach is an example of *constraint-based structure learning*, as we are seeking to constrain (that is, construct a boundary set for) the set of true causal relationships. Here, we specifically use the

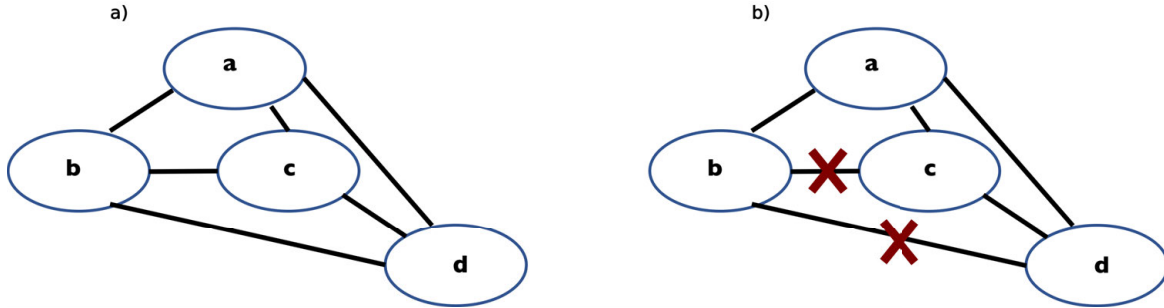


Fig. 3.5. An illustration of the elimination method. For the first step, (a), the model assumes that all potential causal relationships exist. In the second step, (b), connections are eliminated based on conditional independence tests.

temporal version (e.g., Chu et al. (2005); Ebert-Uphoff and Deng (2012)) of the *PC-stable* algorithm (Colombo and Maathuis (2014)). This is simply a more robust, easily parallelized variant of the original *PC* algorithm. This algorithm is available in the TETRAD software package (available at <http://www.phil.cmu.edu/projects/tetrad/>); a simpler implementation is also available in the `learn_struct_pdag_pc` function of the MATLAB Bayes Net Toolbox (BNT, Murphy (2014)). We use the Fisher's Z test for our conditional independence test, although we note that other options for the conditional independence test are available. The Fisher's Z test is based on partial correlation, and works well for continuous variables. Significance is evaluated at 95% confidence ($\alpha = 0.05$); our results are not sensitive to variations in α between 0.01 and 0.1. For more details about the *PC-stable* algorithm and its implementation, readers are referred to Ebert-Uphoff and Deng (2012); hereafter, the *PC-stable* algorithm will be referred to simply as *PC*.

As with the VAR and LASSO models, we do not allow instantaneous connections between variables. We run the *PC* model with 11 time slices, matching our model selection of $p = 5$ for the VAR and LASSO models. We use the original variables $\{z\}$ and 10 time-shifted versions of $\{z\}$; the variables are shifted by $-5, -4, \dots, -1, +1, \dots, +5$ lags (e.g., Ebert-Uphoff and Deng (2012)). We ensure that the model has converged to a solution following the criteria laid out in Ebert-Uphoff and Deng (2012).

3.5 CLIMATE MODEL DATA

We first test our three causal discovery methods using univariate data. We analyze daily model output from the Community Earth System Model–Large Ensemble (CESM-LE, Kay et al. (2015)). CESM is a fully-coupled general circulation model (GCM). Here, we use years 402 to 2,200 of the pre-industrial control run (all external forcing is fixed at 1850 levels). This results in 656,634 days (1,798 years) of output that acts as a proxy for a long observational record. The pre-industrial control run output is gridded at a 1° horizontal grid spacing, 0.9° latitude by 1.25° longitude. The seasonal cycle is removed from the model output by removing the mean and first four Fourier harmonics of the calendar-day climatology. Then, the daily anomalies are averaged into non-overlapping 5-day chunks to smooth out higher frequency variability (our results are not especially sensitive to this averaging period). We determine the optimal maximum lag, p , for the VAR and LASSO models using the Akaike and/or Bayesian information criteria (AIC and BIC, respectively). Here, we have determined that $p = 5$, corresponding to a maximum lag of 25 days for our 5-day averaged data. Thus, all of our models will be evaluated at lags of up to 25 days, with 5 day intervals. For the PC model, this means that the time-shifted versions of $\{z\}$ correspond to lags of -25, -20, ..., -5, +5, ..., +25 days.

After we apply the 5-day averaging, we standardize each time series (subtract its mean and divide by its standard deviation). In this analysis, we focus on Northern Hemisphere winter, defined as December-February (DJF). The Arctic-midlatitude teleconnections are strongest in the winter (e.g., Wallace and Gutzler (1981)), and extratropical storm track activity itself is strongest in the winter (e.g., Hoskins and Hodges (2002), Wettstein and Wallace (2010)). In this section, we limit our focus to the North Pacific (120° - 240° E, 15 - 65° N) and North Atlantic (80 - 0° W, 15 - 75° N); however, in subsequent chapters, we extend our analysis to the entire Northern Hemisphere.

In the long-term, the model output is stationary, as it was generated by a control run with no external forcing. We have also removed the impacts of the seasonal cycle by subtracting the first four Fourier harmonics. Since we focus only on one season (DJF), we can assume that any impacts of

periodic correlation (e.g., Lund et al. (1995)) are sufficiently small. As we are interested in Arctic-midlatitude connections, we select a variable that represents the Arctic, and one that represents the midlatitude circulation. We create the three following univariate time series, each consisting of 32,381 5-day averages:

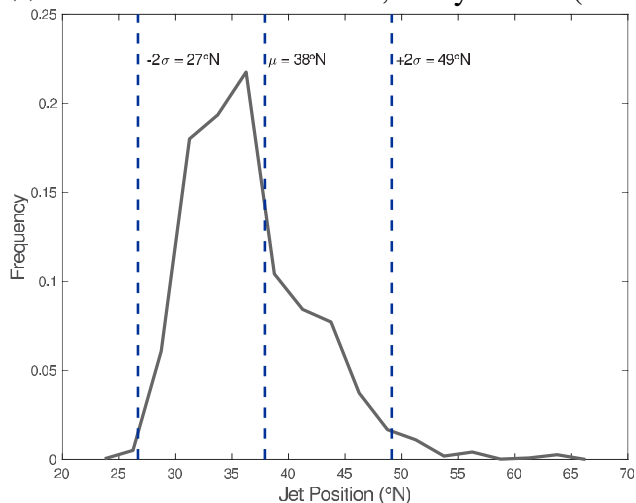
- jet latitude, \mathcal{L} ;
- jet speed, \mathcal{S} ;
- 850 hPa Arctic temperature averaged over 70°N-90°N at all longitudes, \mathcal{T} .

Jet latitude, \mathcal{L} , and jet speed, \mathcal{S} , indicate the position and strength of the eddy-driven jet, respectively. These variables are often used as proxies for the position and strength of the jet-streams. We calculate \mathcal{L} and \mathcal{S} by establishing the maximum position and strength of the zonal winds at 850 hPa, following the procedure outlined in Woollings et al. (2010). For example, consider defining the North Pacific jet. First, we zonally average the 850 hPa zonal winds over the North Pacific basin to create a zonal-mean profile of the zonal wind. Then, we interpolate the zonal-mean zonal wind profile to an 0.01°latitude grid. We then fit a quadratic polynomial around the maximum of the interpolated wind profile. The maximum of this polynomial is the jet speed (\mathcal{S}), while the latitudinal position of the maximum is the jet position (\mathcal{L}). Figure 3.6 shows the distributions of the position (Figure 3.6a) and strength (Figure 3.6b) of the wintertime jet position and speed over the North Pacific in the CESM pre-industrial control simulation. The vertical lines in Figure 3.6 indicate the means (μ) and spreads ($\pm 2\sigma$) of the jet position and strength. Note that we have NOT removed the means or seasonal cycles from jet position and speed distributions in Figure 3.6, so as to show the actual physical values of wintertime jet position and speed over the North Pacific.

3.6 APPLICATION OF CAUSAL DISCOVERY METHODS TO ARCTIC-JET STREAM CONNECTIONS

We model the causal relationships between the Arctic and the midlatitude jet streams by separately exploring the relationships between jet speed (\mathcal{S}) and Arctic temperature (\mathcal{T}), and jet position (\mathcal{L}) and Arctic temperature (\mathcal{T}). We apply all three methods described previously—VAR, LASSO, and PC. We note that VAR and LASSO show both the strength of the relationships (the

(a) North Pacific Jet Position, 5 day means (DJF)



(b) North Pacific Jet Strength, 5 day means (DJF)

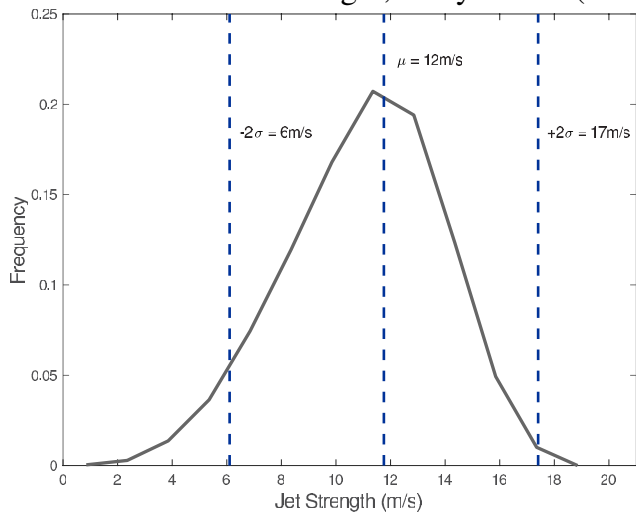


Fig. 3.6. Distributions of (a) jet position and (b) jet strength over the North Pacific in DJF. μ indicates the mean value for jet position and speed, while $\pm 2\sigma$ indicates two standard deviations above and below the mean (μ).

magnitude of the regression coefficients), and the sign of the relationships (the sign of the regression coefficients); PC gives us neither pieces of information. Thus, the advantages of VAR and LASSO are that they provide directed graphs with information regarding both the strength and the sign of the regression coefficients. The advantage of PC is that it imposes a more stringent criteria for causality. Causal relationships that exist in all three models can be considered to be robust. For

VAR, we note that we show all coefficients; for LASSO, only the significant (nonzero) coefficients are shown.

3.6.1 North Pacific

Figure 3.7 displays the results of the VAR (Figure 3.7a), LASSO (Figure 3.7b), and PC (Figure 3.7c) models for jet speed (\mathcal{S}) and Arctic temperature (\mathcal{T}) for the North Pacific. A comparison of the VAR (Figure 3.7a) and LASSO (Figure 3.7b) models makes it clear that the VAR and LASSO models are quite similar—the coefficients that appear in both models have largely the same signs, and similar magnitudes (although we note that by design, LASSO shrinks the overall values of the coefficients; thus, the LASSO coefficients are often smaller than their VAR counterparts). The lags with the strongest regression coefficients are the same in VAR and in LASSO. In the LASSO and VAR models, we can see that \mathcal{S} and \mathcal{T} are both autocorrelated (curved arrows in Figure 3.7). The autocorrelation coefficients are strongest at shorter lags, and decay at longer lags, but remain non-zero.

Of primary interest in this study are the cross-correlation terms—that is, how \mathcal{S} drives \mathcal{T} , and how \mathcal{T} drives \mathcal{S} . We see that at lag day 5, \mathcal{T} drives \mathcal{S} (Figure 3.7a,b); this coefficient is positive, indicating that warm Arctic temperature anomalies drive faster jet speeds in the North Pacific. LASSO and VAR also show significant \mathcal{T} driving \mathcal{S} relationships for lag days 10-20, although the values of these coefficients are much smaller. We also see that in both VAR and LASSO, \mathcal{S} drives a response in \mathcal{T} at a lag of 5 days; this regression coefficient is negative, indicating that a weaker jet drives warm Arctic temperature anomalies (and conversely, a faster jet drives cold Arctic temperature anomalies). While the relationship of \mathcal{S} driving \mathcal{T} is negative at a lag of 5 days, at lag days 15-25, the relationship between \mathcal{S} has changed. At lag days 15-25, faster jets drive warm Arctic temperature anomalies (that is, the regression coefficient for \mathcal{S} driving \mathcal{T} is positive). This hints at the potential existence of a positive feedback loop between jet speed (\mathcal{S}) and Arctic temperature (\mathcal{T})—at longer lags, faster jets drive positive Arctic temperature anomalies, which reinforce the stronger jet, possibly leading to further warming.

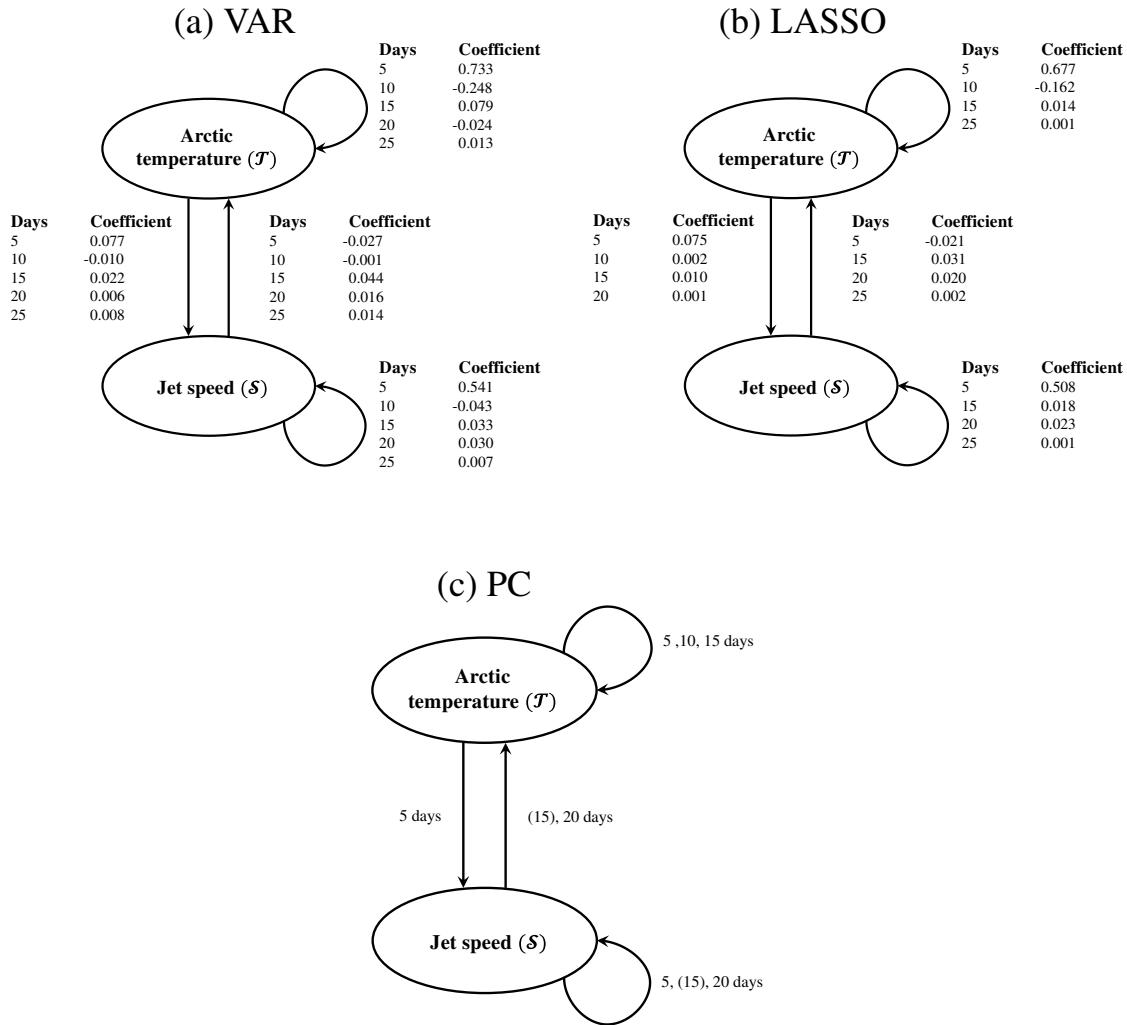


Fig. 3.7. Arctic temperature (\mathcal{T}) and North Pacific jet speed (\mathcal{S}) relationships as described by (a) VAR ($p = 5$), (b) LASSO ($\lambda = 0.0179, p = 5$) and (c) PC (11 time slices, $\alpha = 0.05$) models. Parentheses in PC results denote weak relationships. Curved arrows denote autocorrelation relationships.

The PC model (Figure 3.7c) agrees well with the results of the LASSO (Figure 3.7b) and VAR (Figure 3.7a) models, although by design it does not provide information about the magnitude or sign of the relationships. PC identifies significant relationships for \mathcal{T} driving \mathcal{S} at lag day 5 only; and significant relationships for \mathcal{S} driving \mathcal{T} at lag days 15 and 20. The lags that are significant in the PC model match the lags with the largest coefficients in LASSO.

The results of the VAR, LASSO, and PC models for jet latitude (\mathcal{L}) and Arctic temperature (\mathcal{T}) are shown in Figure 3.8. In the VAR (Figure 3.8a) and LASSO (Figure 3.8b) models, the \mathcal{T} driving \mathcal{L} relationship is negative at lag day 5, and positive at lag day 10. However, as the PC

model (Figure 3.8c) shows that the \mathcal{T} driving \mathcal{L} relationship is only significant at lag day 5, we will only consider the coefficients at lag day 5. The negative coefficient for \mathcal{T} driving \mathcal{L} at lag day 5 implies that warm Arctic temperature anomalies drive an equatorward jet shift in the North Pacific.

While the \mathcal{T} driving \mathcal{L} relationship is relatively weak, the \mathcal{L} driving \mathcal{T} relationship is stronger. Both LASSO and VAR show that \mathcal{L} drives \mathcal{T} with negative coefficients at most lags, implying that an anomalously equatorward jet drives warmer Arctic temperature anomalies (and conversely, an anomalously poleward jet drives cold Arctic temperature anomalies). This relationship is greatest at lag day 5, and strengthens again at lag day 25 in the VAR model. The PC model (Figure 3.8c) shows a similar relationship to the LASSO model, with \mathcal{L} driving \mathcal{T} at lag day 5, and re-emerges at lag day 20-25.

The results of Figures 3.7 and 3.8 are summarized in Figure 3.9. In Figure 3.9, the colors of the arrows indicate the sign of the relationship (determined from VAR and LASSO), while the significant lag days are determined by including only lags that are significant in both the LASSO and PC models. Figure 3.9a summarizes the results between Arctic temperature and jet speed. Collectively, the LASSO and PC results imply that a positive (or *reinforcing*) feedback loop exists between jet speed and Arctic temperatures. Strong jet anomalies at lag days 20-25 drive warm temperature anomalies in the Arctic; these warm Arctic temperature anomalies reinforce the strong jet anomalies at shorter lags, further reinforcing Arctic temperature anomalies. Similarly, the Arctic temperature and jet latitude relationship (Figure 3.9b) suggests a reinforcing feedback loop, although the signs of both regression coefficients are negative in this case. Here, an anomalously equatorward jet at lag days 20-25 drives warm Arctic temperature anomalies. At shorter lags, these warm anomalies reinforce the existing equatorward anomalies. Dynamically, an anomalously equatorward jet could act to enhance Arctic warming via mechanisms such as increases in cyclonic Rossby wave breaking activity on the poleward flank of the jet (e.g., Barnes and Hartmann (2012)). Changes in Rossby wave breaking have possible implications for moisture transport (e.g.,

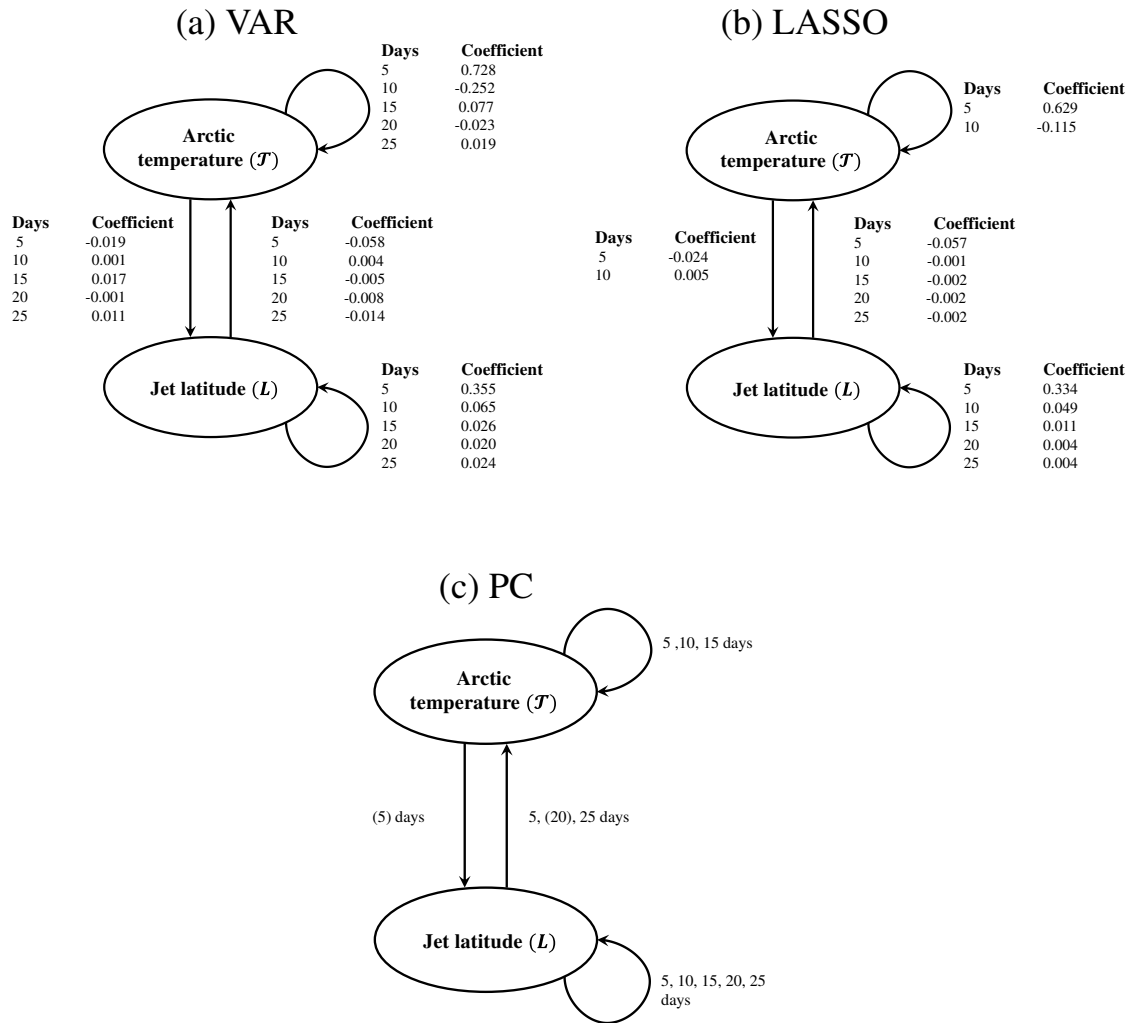


Fig. 3.8. Arctic temperature (\mathcal{T}) and North Pacific jet latitude (\mathcal{L}) relationships as described by (a) VAR ($p = 5$), (b) LASSO ($\lambda = 0.0337, p = 5$) and (c) PC (11 time slices, $\alpha = 0.05$) models. Parentheses in PC results denote weak relationships.

Woods et al. (2013), Liu and Barnes (2015)) and advection into the Arctic. The role of changes in Rossby wave breaking and Arctic temperature will be explored in detail in a later chapter.

3.6.2 North Atlantic

Figure 3.10 displays the results of the VAR (Figure 3.10a), LASSO (Figure 3.10b), and PC (Figure 3.10c) models for jet speed (\mathcal{S}) and Arctic temperature (\mathcal{T}) for the North Atlantic in the wintertime. Again, the LASSO and VAR models look similar, with the largest coefficients in VAR generally appearing in LASSO, and coefficients exhibiting consistency in their signs. In the LASSO and VAR models, we can see that \mathcal{S} and \mathcal{T} are both autocorrelated (curved arrows in

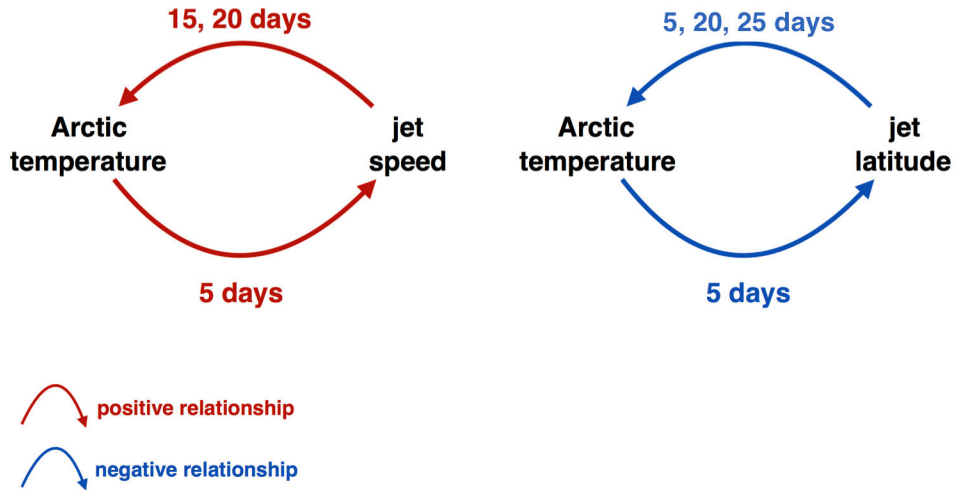


Fig. 3.9. Minimalist graphs showing the dominant feedback loops and their time lags identified by all three methods when applicable. Note that the two positive relationships between Arctic temperature and jet speed result in a positive (i.e. reinforcing) feedback loop. Similarly, the two negative relationships between Arctic temperature and jet latitude together also result in a positive feedback loop.

Figure 3.7). The autocorrelation coefficients are stronger at shorter lags, and decay at longer lags.

In the North Atlantic, \mathcal{T} drives a negative response in \mathcal{L} —that is, a warmer Arctic drives a weakening of the jet. In both VAR and LASSO (Figures 3.10a,b), the \mathcal{T} driving \mathcal{L} coefficients are negative at all lags (all significant lags for LASSO). This is in contrast to the North Pacific, where warm Arctic temperature anomalies drive a stronger jet (Figure 3.7). The \mathcal{L} driving \mathcal{T} relationship is also negative in the North Atlantic—all lags that are included in both VAR (Figure 3.10a) and LASSO (Figure 3.10b) show negative regression coefficients, indicating that an anomalously weak jet drives warm Arctic temperature anomalies.

In the PC model for the North Atlantic jet strength–Arctic temperature relationship (Figure 3.10c), only a few lags are shown to be significant. Arctic temperature drives a significant response in jet strength at lags of 5 and 20 days. However, the response at 5 days is characterized as weak in PC, and the 5 day lag is not significant in LASSO; thus, we only consider the \mathcal{T} driving \mathcal{L} relationship at lag day 20. Jet strength drives a significant response in Arctic temperature at lag day 10.

The results for the VAR (Figure 3.11a), LASSO (Figure 3.11b), and PC (Figure 3.11c) models of jet position and Arctic temperature (\mathcal{L} and \mathcal{T}) are seen in Figure 3.11. Again, both variables

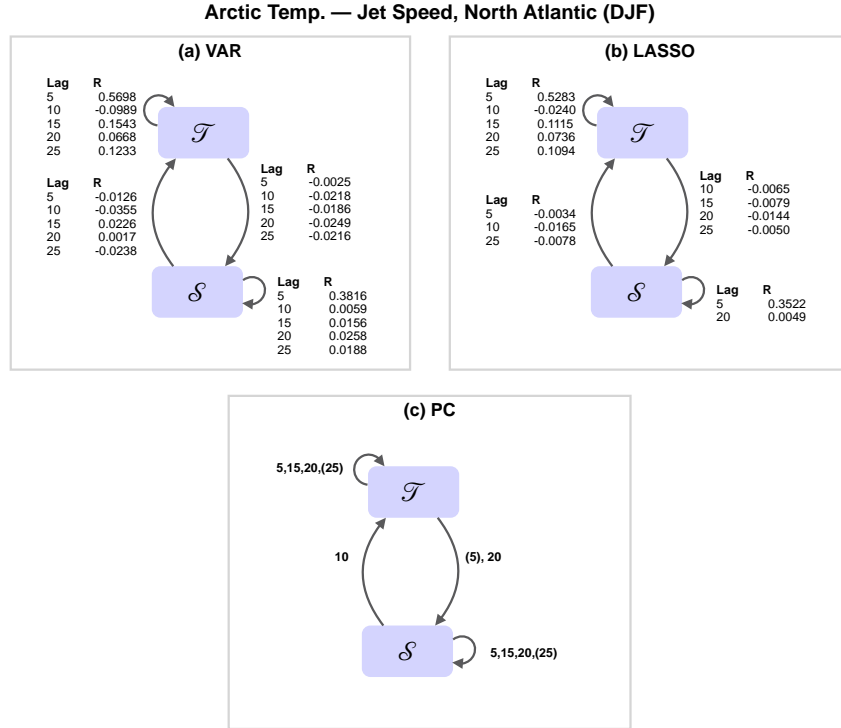


Fig. 3.10. Arctic temperature (\mathcal{T}) and North Atlantic jet speed (\mathcal{S}) relationships as described by (a) VAR ($p = 5$), (b) LASSO ($p = 5$) and (c) PC (11 time slices, $\alpha = 0.05$) models. Parentheses in PC results denote weak relationships. Curved arrows denote autocorrelation relationships.

show autocorrelation that is strongest at shorter lags and weakens at larger lags. Arctic temperature's influence on North Atlantic jet latitude is weaker than in the North Pacific—the VAR coefficients are all very small (Figure 3.11a), while the LASSO model shows no significant coefficients for \mathcal{T} driving \mathcal{L} (Figure 3.11b). North Atlantic jet latitude drives a negative response in Arctic temperature at lag day 5 and lag days 20–25, and a positive response in Arctic temperature at lag days 10 and 15 (Figure 3.11a). In the LASSO model, \mathcal{L} drives a response in \mathcal{T} at lag days 10 and 25 (Figure 3.11b). Thus, at lag day 10, an anomalously poleward jet drives warm Arctic temperature anomalies, while at lag day 25, an anomalously equatorward jet drives warm temperature anomalies in the Arctic. The PC model for \mathcal{L} and \mathcal{T} shows no significant lags for \mathcal{T} driving \mathcal{L} , while only lag day 10 is significant for \mathcal{L} driving \mathcal{T} .

Arctic Temp. — Jet Position, North Atlantic (DJF)

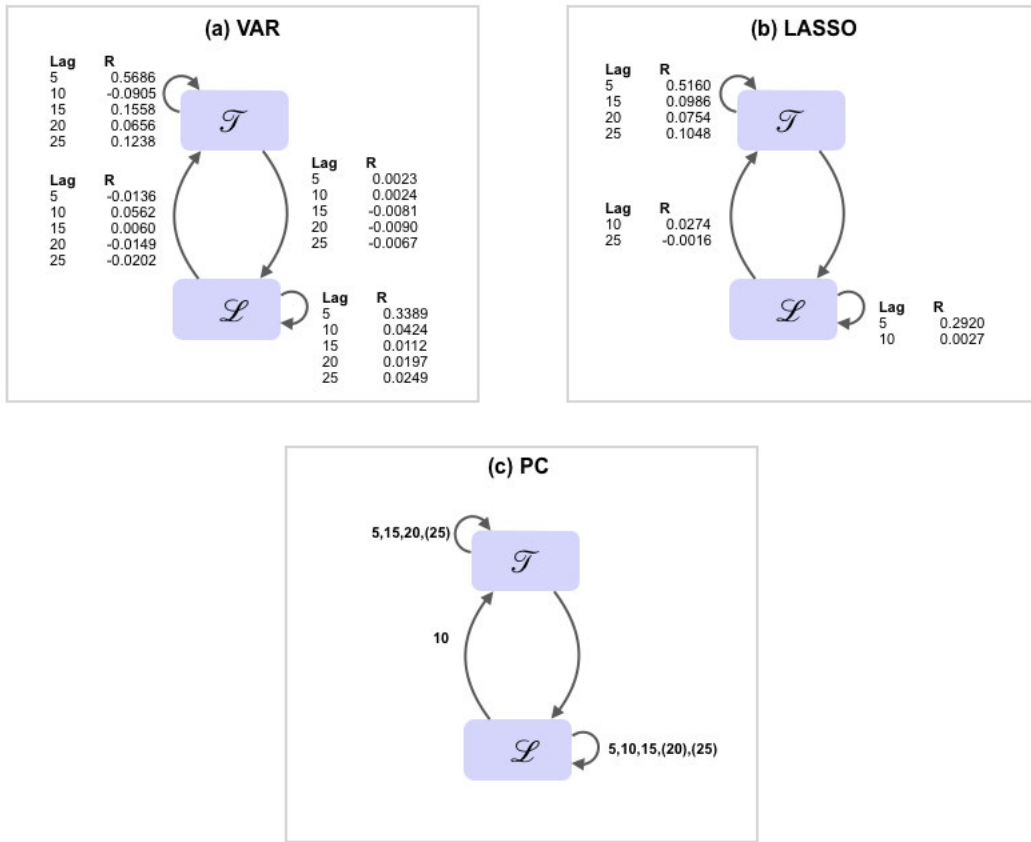


Fig. 3.11. Arctic temperature (\mathcal{T}) and North Atlantic jet latitude (\mathcal{L}) relationships as described by (a) VAR ($p = 5$), (b) LASSO ($p = 5$) and (c) PC (11 time slices, $\alpha = 0.05$) models. Parentheses in PC results denote weak relationships. Curved arrows denote autocorrelation relationships.

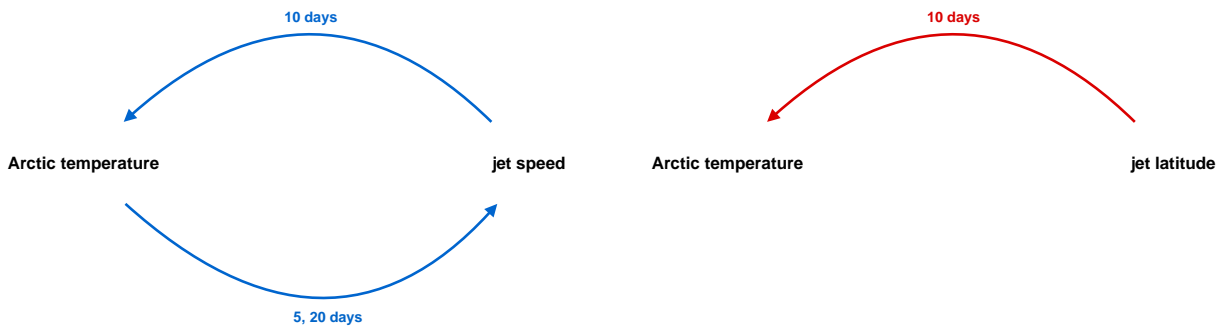


Fig. 3.12. Minimalist graphs showing the dominant feedback loops and their time lags identified by all three methods for the North Atlantic. The two negative relationships between Arctic temperature and jet speed result in a positive (i.e., reinforcing) feedback loop. Arctic temperature did not exert a significant influence on North Atlantic jet latitude in either the PC or LASSO models.

Figure 3.12 summarizes the results of Figures 3.10 and 3.11. In Figure 3.12, the colors of the arrows show the sign of the relationship (determined from VAR and LASSO), and the significant lag days are determined by including only lags that are significant in both the LASSO and PC models. Figure 3.12a summarizes the results between Arctic temperature and jet speed in the North Atlantic. Collectively, the LASSO and PC results suggest that a reinforcing feedback loop exists between North Atlantic jet speed and Arctic temperatures. Warm temperature anomalies in the Arctic at lag day 20 drive a weakening of the jet; this weaker jet drives more warm Arctic temperature anomalies at lag day 10, and these warm temperature anomalies drive further weakening of the jet at lag day 5. A more poleward North Atlantic jet drives warm Arctic temperature anomalies at a lag of 10 days (Figure 3.12b); the LASSO and PC models did not identify any significant lagged relationships for \mathcal{T} driving \mathcal{L} over the North Atlantic. Some studies have linked Arctic warming to a weaker, wavier jet stream (e.g., Liu et al. (2012), Francis and Vavrus (2012)), particularly over the Atlantic; this hypothesis, however, has been debated (e.g., Barnes (2013), Woollings et al. (2014), Barnes and Screen (2015)). While the results from Figure 3.12 do not indicate a strong relationship between Arctic temperatures and the position of the North Atlantic jet, they do connect a warmer Arctic with a weaker jet in the North Atlantic on 5-25 day timescales.

3.7 CONCLUSIONS

We have used three different causal discovery approaches—VAR, LASSO, and PC—quantified robust positive feedback loops between the jet position and strength in the North Pacific and North Atlantic, and Arctic temperatures on 5-25 day timescales. In the North Pacific, a faster jet drives warm Arctic temperature anomalies, which act to reinforce the faster jet. An anomalously equatorward jet also drives warm Arctic temperature anomalies; these warm anomalies drive a reinforcement of the equatorward jet position, leading to further warming. In the North Atlantic, warm Arctic anomalies drive weak anomalies in the jet; and these weak jet anomalies reinforce the Arctic warming.

Throughout this study, we have focused on the linear relationships between Arctic temperatures and the jet stream. Our Granger causality models (VAR and LASSO) are at heart linear regression

models, while the Pearl causality model (PC) uses conditional independence tests based on partial correlation (which measures linear dependence). However, relationships in the climate system can be complex and nonlinear. Nonlinear regression models such as nonlinear random forests (e.g., Papagiannopoulou et al. (2017)) provide a path forward for identifying nonlinear Granger dependencies between variables. Similarly, the conditional independence tests in the PC algorithm could be altered—as an example, entropy-based measures such as mutual information could perhaps identify nonlinear Pearl causal relationships.

We also note that all observational analyses, regardless of their causal framework, are limited in their ability to identify hidden common causes. Thus, we caution that the results from this study should be interpreted carefully—these results are best thought of as *hypotheses* that can be studied more closely using tools such as targeted climate modeling studies. For example, one could possibly test the positive feedback loop outlined in Figure 3.9a using a set of transient model experiments that vary the speed of the jet, and examine the Arctic temperature response. Currently, work is being done to improve the Fast Causal Inference (FCI) algorithm (an extension of the PC algorithm, Spirtes et al. (2000)) by improving its ability to identify hidden common causes.

The work described here is only the beginning of a larger effort that aims to apply causal discovery techniques to large-scale climate dynamics problems, such as Arctic-midlatitude dynamics. Future chapters of this dissertation will outline some of the work that has built upon these preliminary results. Outside of this dissertation, current research is focusing on using similar tools to explore causal pathways between the Madden-Julian Oscillation (MJO) and the North Atlantic Oscillation (NAO); on improving the FCI algorithm’s ability to identify hidden common causes (Samarasinghe et al. (2018a)); and in the broad dissemination of the algorithms described here, and the ideas behind them, to the atmospheric and climate science communities.

Support for this work was provided by National Science Foundation (NSF) grants AGS-1545675 (Barnes and McGraw) and AGS-1445978 (Ebert-Uphoff and Samarasinghe) under the Climate and Large-scale Dynamics program.

4 New Insights on Subseasonal Arctic-Midlatitude Causal Connections from a Regularized Regression Model¹

Arctic-midlatitude teleconnections are complex and multifaceted. By design, modeling studies typically focus only on one direction of influence—usually, the midlatitude atmospheric response to a changing Arctic. The two-way, coupled feedbacks between the Arctic and the midlatitude circulation on sub-monthly timescales are explored using a regularized regression model formulated around Granger causality, or added predictive power. The regularized regression model indicates that there are regions in which Arctic temperature drives a midlatitude circulation response, and regions in which the midlatitude circulation drives a response in the Arctic; however, these regions rarely overlap. In many regions, on sub-monthly timescales, the midlatitude circulation drives Arctic temperature variability, highlighting the important role the midlatitude circulation can play in impacting the Arctic. In particular, the regularized regression model results support recent work that indicates that the observed high pressure anomalies over Eurasia drive a significant response in the Arctic on sub-monthly timescales, rather than being driven by the Arctic.

4.1 INTRODUCTION

As the Arctic continues to warm at a pace that outstrips the rest of the globe, questions of Arctic influence on the weather and climate of lower latitudes abound. Often, Arctic-midlatitude climate studies emphasize the impacts of Arctic variability upon the midlatitude circulation, with numerous studies linking Arctic warming to changes in midlatitude temperature variability and extremes (e.g., Screen et al. (2015a), Ayarzagüena and Screen (2016), Blackport and Kushner (2017)); the jet streams (e.g., Deser et al. (2010), Butler et al. (2010), Peings et al. (2017), Ronalds et al. (2018), Zappa et al. (2018), Screen et al. (2018)); and large-scale circulation patterns (e.g., Overland et al.

¹This chapter contains material that has been submitted to the *Journal of Climate* as: McGraw, M.C. and E.A. Barnes: New Insights on Subseasonal Arctic-Midlatitude Causal Connections from a Regularized Regression Model, submitted to *Journal of Climate*, 02/2019.

(2015), Blackport and Kushner (2017), Screen et al. (2018)). However, the midlatitude circulation also impacts Arctic weather and climate. Moist air intrusions from lower latitudes have been linked to reductions in sea ice extent and thickness (e.g., Park et al. (2015a), Park et al. (2015b), Woods and Caballero (2016), Mortin et al. (2016), Burt et al. (2016)), Arctic surface temperature variability (e.g., Woods et al. (2013), Messori et al. (2018)), and changes in upper ocean heat content (e.g., Park et al. (2015a)). These moisture intrusions into the Arctic have been attributed to the large-scale midlatitude circulation features, such as Rossby wave breaking (e.g., Woods et al. (2013), Liu and Barnes (2015)), atmospheric rivers (e.g., Newman et al. (2012), Baggett et al. (2016)), and even tropical convection (e.g., Lee (2014), Baggett and Lee (2017)). Warming in the Arctic has also been driven by latent energy transport (e.g., Graversen and Burtu (2016)) and warm air advection (e.g., Messori et al. (2018)). Thus, the Arctic and the midlatitudes influence and drive variability in each other, with both directions having substantial impacts.

Such issues of cause and effect are often explored in targeted modeling studies, where the model is externally forced (for example, by sea ice loss), and the atmospheric response to that forcing is evaluated. However, despite their many advantages, these studies also have their own limitations—namely, they are limited to analyzing only one direction of influence. In the case of Arctic-midlatitude interactions, for example, most targeted modeling experiments explore the influence of a warmer or sea ice-reduced Arctic on the midlatitude circulation. They simulate Arctic warming and/or sea ice loss through many approaches, such as adjusting surface heat fluxes to mimic a reduced-ice ocean (e.g., Oudar et al. (2017)); continually nudging sea ice to some target value (e.g., Smith et al. (2017), McCusker et al. (2017)); reducing the albedo of the sea ice (e.g., Blackport and Kushner (2016), Blackport and Kushner (2017)); or simply applying a warm anomaly to the lower atmosphere (e.g., Butler et al. (2010)) (see Box 1 in Screen et al. (2018) for more discussion of the different approaches to modeling Arctic warming and sea ice loss). These different approaches have one thing in common—the Arctic is continually forced to a certain state (warm air temperatures, increased heat fluxes, or a certain sea ice state), regardless of what the atmosphere may be doing. Thus, while the Arctic is able to modify the atmospheric circulation, the atmospheric circulation is ultimately limited in its ability to impact the Arctic. However, we

know that the atmospheric circulation does impact the Arctic climate—and thus, a comprehensive understanding of Arctic-midlatitude climate dynamics must ultimately account for the circulation’s ability to modify Arctic climate.

While targeted modeling studies can generally only analyze one direction of influence, causal discovery-based approaches can augment model experiments by facilitating the simultaneous analysis of both directions of influence—Arctic on midlatitude circulation, and midlatitudes on Arctic. Causal discovery methods strive to identify cause and effect relationships in climate data, and represent them with graphical models (see Ebert-Uphoff and Deng (2012) for an overview of causal discovery analysis in climate sciences). One approach to causality uses the Granger causality framework (Granger (1969)). This approach studies existing model output or reanalysis products to determine cause-effect relationships based on evaluation of added variance explained—that is, does the incorporation of some lagged variable X significantly improve the predictability of some variable Y , beyond Y ’s ability to predict itself? The Granger causality framework has been applied to climate science problems in recent years (see Attanasio et al. (2013) and McGraw and Barnes (2018) (Chapter 2), and references therein); and in particular, to Arctic-midlatitude climate dynamics. Strong et al. (2009) and Matthewman and Magnusdottir (2011) study the relationship between sea ice and large-scale Northern Hemisphere atmospheric variability with a vector autoregression (VAR) model. Kretschmer et al. (2016) identify key Arctic predictors of the wintertime circulation using a graphical model-based approach that uses Granger causality to assess the strength of the predictors. Samarasinghe et al. (2018b) (Chapter 3) study the relationship between Arctic temperatures and the jet streams using three different causal discovery approaches, and identify positive feedback loops between Arctic temperature and North Pacific jet position and strength on sub-monthly timescales.

In this paper, similar to the works mentioned in the previous paragraph, we apply a regression model formulated around Granger causality in order to explore the sub-monthly, two-way feedbacks between the Arctic and the midlatitude circulation. Our approach allows for the simultaneous analysis of the two-way feedbacks between the Arctic and the midlatitude circulation that are not fully represented in targeted climate model experiments. In contrast to reanalysis-based

studies that typically use standard lagged linear regression analysis, our use of the Granger causality framework accounts for the persistence of memory due to autocorrelation and frames these relationships in terms of added predicted power. As in Samarasinghe et al. (2018b) (Chapter 3), we apply our model in such a way to allow for the analysis of two-way feedbacks, rather than focusing on more specific predictor-predictand relationships. We refine a standard vector autoregression (VAR) model by applying a regularization criteria; the advantages of this approach and the details of its implementation are discussed in section 4.2.3. Furthermore, nearly all previous explorations of Arctic-midlatitude connections using Granger causality and VAR methods have been performed on univariate time series data. Here, instead of representing the midlatitude circulation with univariate climate indices, we analyze the midlatitude circulation in a full spatiotemporal field by creating an individual regression model of 500 hPa geopotential height at each gridpoint. Thus, the approach detailed here inherently accounts for the regional variability that is key to a lush, vibrant, and full understanding of Arctic-midlatitude dynamics without making any a priori assumptions about key regions.

4.2 DATA AND METHODS

4.2.1 Data

We use NASA’s Modern-Era Retrospective analysis for Research and Applications, Version 2 (MERRA-2, GMAO (2015)). We represent the midlatitude circulation with 500 hPa geopotential height at every gridpoint (Z_{500}). Z_{500} has dimensions of [longitude \times latitude \times time], and is analyzed over the Northern Hemisphere only. The Arctic is represented by the 850 hPa temperature from 70°-90° N (T_{polar}). T_{polar} is averaged both zonally and meridionally and thus has dimensions of [1 \times time]. For both variables, we use the years 1980-2017. We remove the seasonal cycle from the daily data by subtracting the mean and the first four Fourier harmonics. The daily data are then averaged into non-overlapping 5-day chunks to smooth out higher-frequency variability. For this work, we focus only on boreal winter (December-February).

4.2.2 Granger Causality

Throughout this manuscript, we work within the framework of Granger causality (Granger (1969)). Granger causality frames causal relationships in terms of added predictability—that is, it assesses whether or not a given variable adds predictive power beyond the predictand’s ability to forecast itself (see McGraw and Barnes (2018), Chapter 2 in this dissertation, for a more thorough discussion of Granger causality). First developed as a predictive econometric modeling tool, Granger causality has more recently found applications in climate science, including, but not limited to, the influence of sea surface temperature on atmospheric variability (e.g., Mosedale et al. (2006)) and hurricane strength (e.g., Elsner (2006), Elsner (2007)); snow cover’s influence on surface temperature (e.g., Kaufman et al. (2003)); the impact of ENSO on the Indian Monsoon (e.g., Mokhov et al. (2011)); and detection and attribution of global temperature increases (see Attanasio et al. (2013) and references therein). By requiring that the predictor must explain a significant amount of variance beyond that of the predictand, Granger causality thus imposes a more stringent criteria for identifying a causal relationship than a standard lagged linear regression, and is less likely to overreport significant relationships due to its accounting for the effects of autocorrelation. In order to evaluate whether or not T_{polar} Granger-causes variability in Z_{500} (and vice-versa), we set up a vector autoregression (VAR) model, similar to Strong et al. (2009), which we then further modify with a regularization scheme.

4.2.3 Deriving the LASSO Model

We model the relationship between Z_{500} and T_{polar} with a p th-order vector autoregression (VAR) model, which predicts each model variable using lagged values of all the model variables (e.g., ?). We further modify the VAR model with a regularization scheme, which reduces a full VAR model to a sparse model that selects only the predictors that have the strongest impact on the predictability of the response (e.g., Hastie et al. (2001)). That is, a regularized regression model identifies only the most important predictors, and reduces the likelihood of overfitting the model. Here, we use the LASSO (Least Absolute Shrinkage and Selection Operator, e.g., Tibshirani (1996), Hastie et al. (2015), Nicholson et al. (2017)) approach to identify only the key

predictors.

First, we create our full, non-regularized VAR model. Here, as we are interested in the two-way relationships between Z_{500} and T_{polar} , we apply a two-variable p th-order VAR model to the anomalies of Z_{500} and T_{polar} ,

$$Z_{500}(t) = a_1 Z_{500}(t-1) + a_2 Z_{500}(t-2) + \dots + a_p Z_{500}(t-p) + \dots \quad (4.1a)$$

$$b_1 T_{polar}(t-1) + b_2 T_{polar}(t-2) + \dots + b_p T_{polar}(t-p) + \epsilon_{1,t}$$

$$T_{polar}(t) = c_1 Z_{500}(t-1) + c_2 Z_{500}(t-2) + \dots + c_p Z_{500}(t-p) + \dots \quad (4.1b)$$

$$d_1 T_{polar}(t-1) + d_2 T_{polar}(t-2) + \dots + d_p T_{polar}(t-p) + \epsilon_{2,t},$$

where $\epsilon_{1,t}$ and $\epsilon_{2,t}$ are error terms. We note that we do not allow Z_{500} and T_{polar} to influence each other simultaneously, which allows us to use the simpler form of VAR seen in Equation A1. Equation A1a uses lagged values of Z_{500} and T_{polar} to predict Z_{500} —the a coefficients quantify Z_{500} 's influence on itself, while the b coefficients quantify the influence of T_{polar} on Z_{500} . Similarly, in Equation A1b, lagged values of Z_{500} and T_{polar} are used to predict T_{polar} —the c coefficients quantify Z_{500} 's influence on T_{polar} , while the d coefficients quantify the influence of T_{polar} on itself. We then assess Equation A1 for added predictive power by, for example, comparing predictions of Z_{500} with and without T_{polar} . That is, we compare Equation A1 to a version of Equation A1 in which the b coefficients are set to zero. If including information about T_{polar} significantly improves our ability to predict Z_{500} , we can say that T_{polar} is a Granger-cause of Z_{500} .

Often, the full, non-regularized VAR model is assessed collectively for Granger causality using a metric such as an F-test or a likelihood score to determine added predictive power (see Sims (1980), and discussion in Appendix A). This means that regression coefficients cannot be identified as significant or not significant on an individual basis. For example, in Equation A1, when we evaluate if T_{polar} is a Granger-cause Z_{500} , we ask whether or not all b coefficients collectively increase our ability to predict Z_{500} . Thus, by design, either *all* b coefficients will be significant, or none of them will be. One limitation of such an approach is the fact that many coefficients are close to, but not exactly zero. But as we are not evaluating the significance of the coefficients

individually, it is difficult to determine which coefficients are the most important predictors, and which are simply noise. A user-defined threshold on the magnitude of the coefficients could be applied—coefficients above this threshold would be retained, while coefficients smaller than this threshold would be discarded. However, such a user-defined threshold can be highly subjective.

Regularized regression provides a less arbitrary approach for identifying key coefficients from a VAR model. When we modify the VAR model with a LASSO regularization scheme, we can simplify Equation A1 to a sparse model that contains only the most important predictors. The LASSO approach finds a least squares solution that imposes a bound, λ , on the sum of the absolute values of the regression coefficients; the sparsity of the model (that is, the number of coefficients set to zero) is controlled by the value of λ . Practically speaking, this constraint generates a model that is of the same form as Equation A1, but with many coefficients equalling exactly zero. This means that significant coefficients are non-zero, while all coefficients that are not significant are exactly zero. Since this approach retains only the most important regression coefficients, it is more easily interpreted, and improves the model’s prediction accuracy compared to an ordinary least squares approach (e.g., Tibshirani (1996)). In this work, we use a version of the group LASSO approach (that is, an approach that is designed for predictors with a natural group structure, such as time series data (e.g., Hastie et al. (2015), Nicholson et al. (2017))), which is detailed in Chapter 3.

The LASSO model requires careful selection of the regularization parameter, λ . When $\lambda = 0$, the LASSO approach is identical to Equation A1; and as λ approaches ∞ , the solution becomes very sparse (that is, nearly all coefficients are zero). λ selection is thus critical. Here, we select the λ using a K-fold cross-validation scheme ($K = 10$); the selected λ corresponds to the minimum mean squared error plus one standard deviation (e.g. Hastie et al. (2015), Melkumova and Shatskikh (2017), Samarasinghe et al. (2018b)). We note that this paper focuses on a discussion of the results of the LASSO model, but results from the VAR model alone (Equation A1, with $\lambda = 0$) are presented in Appendix A.

Selecting the maximum lag, represented by p , is also important for any lagged regression model. The optimal value of p represents a trade off between a model with a value of p that is large enough to account for all physically relevant relationships and a model with a value of p

that is small enough to yield a model that is easily interpretable. Here, we use a model order of $p = 5$ —that is, 5 chunks of 5-day means, implying lagged timescales of up to 25 days. We establish our optimum p using the Akaike information criterion (Ivanov and Kilian (2005)), and by noting that we are interested in processes that occur over timescales of about 1 month.

4.3 RESULTS

We first analyze the results of the LASSO model applied in two dimensions— Z_{500} at every gridpoint, and T_{polar} averaged over the polar cap—in section 4.3.1. This two-dimensional approach allows us to clearly identify both regions that are influenced by the Arctic (T_{polar} driving Z_{500}), and regions that influence the Arctic (Z_{500} driving T_{polar}), as well as how these regions vary with different lags. After we characterize the full spatiotemporal Arctic-midlatitude relationships in section 4.3.1, we select key regions for further analysis in section 4.3.2. We separate these regions into those dominated by T_{polar} driving Z_{500} , and those dominated by Z_{500} driving T_{polar} . We discuss the implications of these results in section 4.4.

4.3.1 Two-Dimensional LASSO Model

We use the LASSO model described in section 4.2.3 to explore the relationship between Arctic temperatures (T_{polar}) and the midlatitude circulation (Z_{500}) in the MERRA-2 reanalysis. As discussed in section 4.2.3, in a LASSO model, regression coefficients are either zero (not significant) or non-zero (significant); thus by definition, any coefficient seen in Figures 4.1 and 4.2 is significant, and viewed as a Granger-cause of T_{polar} or Z_{500} , respectively.

We note that both Z_{500} and T_{polar} exhibit autocorrelation (a and d coefficients, respectively, in Equation A1; not shown). Like many variables, temperature and geopotential height are typically modeled as “red noise” processes—that is, they have some memory of their past states. As expected, this autocorrelation is strongest at shorter lags and decays at longer lags. The VAR model separates the prediction of, for example, Z_{500} into an autocorrelated component (i.e., Z_{500} predicting Z_{500} , a coefficients in Equation A1a) and a cross-correlated component (i.e., T_{polar} predicting Z_{500} , b coefficients in Equation A1a); thus, the influence of autocorrelation on the cross-correlated

components is limited, and our Granger definition of causality (based on additional predictability beyond autocorrelation, as discussed in section 4.2.2) is satisfied.

Figure 4.1 shows the results of the LASSO model of T_{polar} driving Z_{500} in units of standardized regression coefficients ($\frac{\sigma_{Z_{500}}}{\sigma_{T_{polar}}}$, based on the b terms in Equation A1a). That is, Figure 4.1 indicates the regions in which variability in Arctic temperatures Granger-cause variability in the local 500 hPa heights. Red gridpoints in Figure 4.1 indicate a positive lagged relationship, in which warm Arctic temperature anomalies drive high height anomalies at that gridpoint; blue gridpoints in Figure 4.1 indicate a negative lagged relationship in which warm Arctic temperature anomalies drive low height anomalies at that gridpoint. At lag day 5 (Figure 4.1a), a few regions show a sensitivity to T_{polar} —warm Arctic temperature anomalies drive positive height anomalies over much of Greenland, far eastern Russia and Kamchatka, and the subtropical Pacific. Warm Arctic temperature anomalies also drive negative height anomalies over the tropical Atlantic at a lag of 5 days (Figure 4.1a). At lag day 10 (Figure 4.1b), the positive relationship between Arctic temperatures and Z_{500} remains over a smaller region of the subtropical Pacific, and over southern Greenland; there are also sparse areas of significant relationships over central Europe and the Urals. By lag day 15, few regions' circulation anomalies appear to be significantly driven by Arctic temperatures (Figure 4.1c).

We note that we only explore relatively short timescales here, at lags of 25 days or shorter. Many recent studies have focused on a stratospheric pathway of influence from the Arctic to the midlatitudes—broadly speaking, this hypothesis purports that warm temperature anomalies in the Arctic (with a particular emphasis on the Barents-Kara Sea region) drive changes in vertical wave activity, which act to modify and disrupt the stratospheric polar vortex, ultimately affecting the tropospheric circulation (e.g., Peings and Magnusdottir (2014), Sun et al. (2015), Wu and Smith (2016), Screen (2017), Zhang et al. (2018a)). 25 days is likely not a sufficient amount of time to capture the impacts of these lower-frequency processes; and thus, our results do not preclude the possibility of Arctic temperatures indirectly influencing the midlatitude circulation indirectly via the stratosphere on longer timescales.

T_{polar} driving Z_{500}

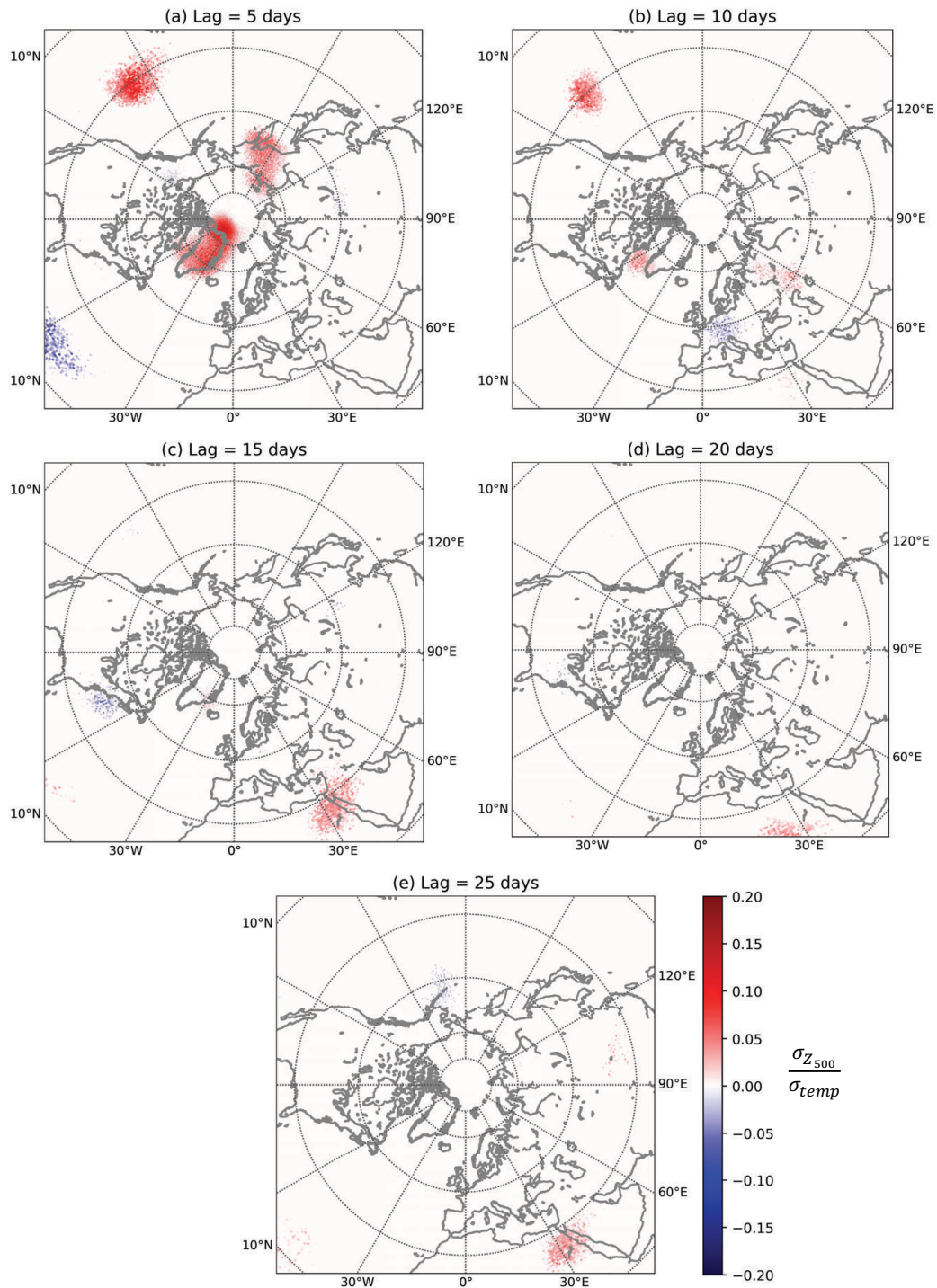


Fig. 4.1. LASSO model of T_{polar} driving Z_{500} at each gridpoint at lags of (a) 5 days to (e) 25 days. The shading is in units of standardized regression coefficients ($\sigma_{Z_{500}}/\sigma_{temp}$).

Figure 4.2 displays the LASSO model of Z_{500} driving T_{polar} in units of standardized regression coefficients ($\frac{\sigma_{T_{polar}}}{\sigma_{Z_{500}}}$, based on the c terms in Equation A1b). Figure 4.2 highlights the regions in which the circulation at each gridpoint (represented by Z_{500}) Granger-causes Arctic temperature variability. Again, red gridpoints indicate a positive lagged relationship (high height anomalies at that gridpoint driving warm Arctic temperature anomalies), and blue gridpoints indicate a negative lagged relationship (low height anomalies at that gridpoint driving warm Arctic temperature anomalies). At lag day 5 (Figure 4.2a), many regions show a significant relationship between local Z_{500} (that is, Z_{500} at that gridpoint) and polar temperatures. Over Alaska, the Beaufort Sea, and the east Pacific, as well as Siberia and the Barents-Kara Seas, high Z_{500} anomalies drive warm Arctic anomalies; over the Sea of Okhotsk and the western Pacific, and eastern Canada, the North Atlantic, and Greenland and Iceland, low Z_{500} anomalies drive warm Arctic anomalies (Figure 4.2a). Remotely, at lag day 5, high height anomalies over the subtropical Atlantic also drive warm Arctic anomalies (Figure 4.2a). The wave-2-like anomalies in Figure 4.2a resemble an enhancement of the zonally asymmetric circulation (defined as the time-mean of Z_{500} with the zonal mean removed; seen in Figure 4.3a), with the notable exception of over western Europe, where there is no significant relationship in the LASSO model. Previous studies (e.g., Baggett et al. (2016), Graversen and Burtu (2016), Messori et al. (2018)) have also linked Arctic warming with enhancement of the climatological planetary-scale wave activity, and increased warm air advection into the Arctic.

The pattern seen at lag day 5 is largely absent from lag day 10 (Figure 4.2b)—the high height anomaly over Alaska and the Beaufort Sea has shifted eastward. The region of low height anomalies over the Sea of Okhotsk has also shifted eastward at lag day 10, although the anomalies are weaker, less cohesive, and also shifted northward (Figure 4.2b). Z_{500} anomalies over Alaska and the Beaufort Sea remain influential at lag days 15 and 20 (Figure 4.2c,d), with low Z_{500} anomalies in this region driving warm Arctic temperatures, and high Z_{500} anomalies over Hudson Bay and in the subtropical Pacific driving warm Arctic temperatures at lag day 15 (Figure 4.2c). Around lag day 20, a signal begins to re-emerge over Siberia, with high Z_{500} anomalies driving warm Arctic

Z_{500} driving T_{polar}

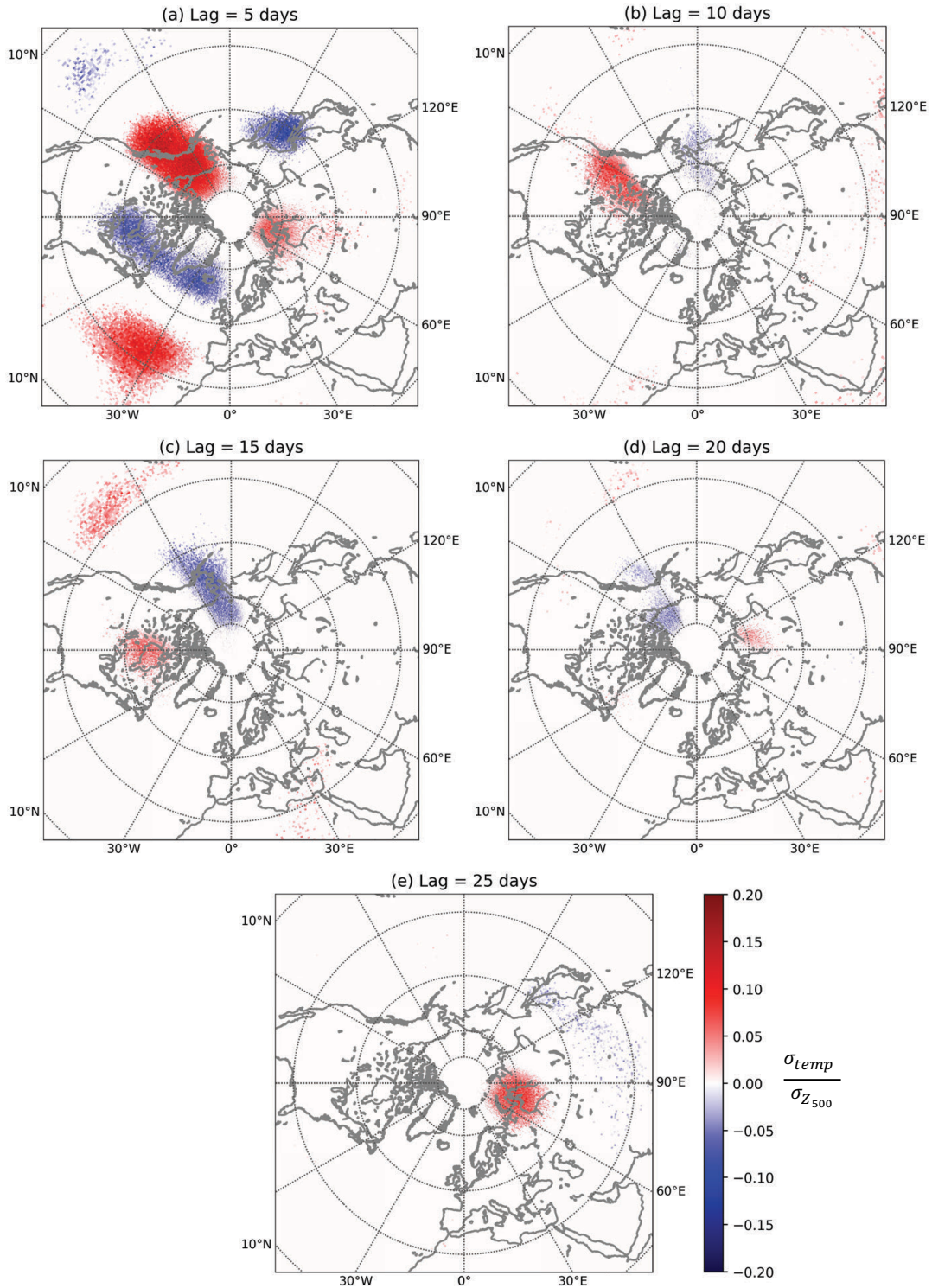


Fig. 4.2. LASSO model of Z_{500} at each gridpoint driving T_{polar} at lags of (a) 5 days to (e) 25 days. The shading is in units of standardized regression coefficients ($\sigma_{temp}/\sigma_{Z_{500}}$).

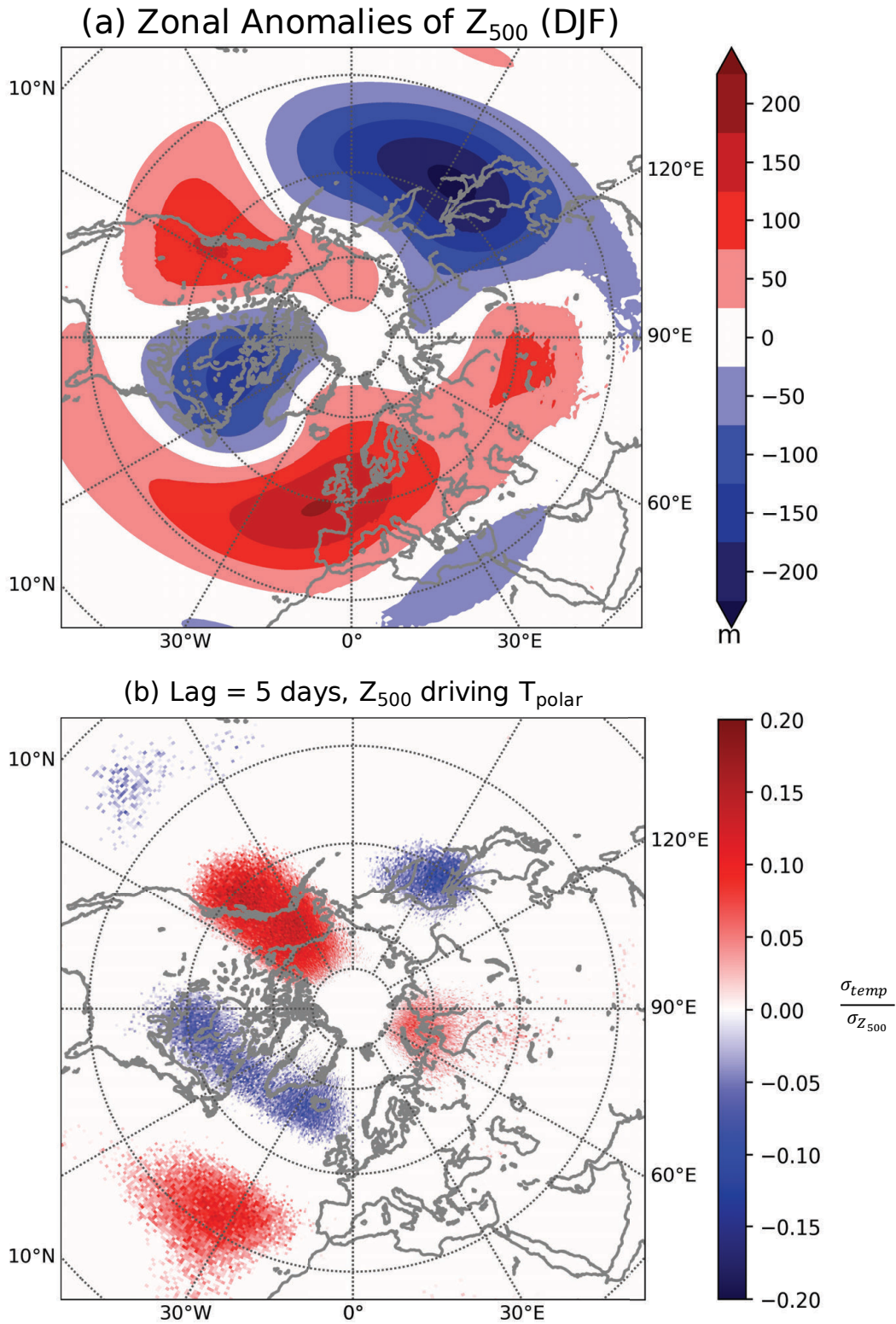


Fig. 4.3. (a) Zonal anomalies of the time-mean 500 hPa geopotential heights in DJF. (b) Panel a of Figure 4.2 (LASSO model of Z_{500} at each gridpoint driving T_{polar} at lag day 5), reprinted for comparison.

temperatures (Figure 4.2d). While this region of positive regression coefficients is small at lag day 20, by lag day 25, the region of positive regression coefficients is much larger and stronger, linking high height anomalies over Siberia and the Barents-Kara Sea to warm Arctic temperatures 25 days later (Figure 4.2e).

Figures 4.1 and 4.2 display the results of the LASSO models for T_{polar} driving Z_{500} , and Z_{500} driving T_{polar} , respectively. In the case of both models, 37 years of MERRA-2 reanalysis shows significant results for 5-25 day timescales in many regions. Additionally, the regions in which Arctic temperatures drive variability in the midlatitude circulation are *not* the same regions as those where the midlatitude circulation drives Arctic temperature variability. More specifically, Arctic temperatures Granger-cause significant circulation responses over eastern Russia, the subtropical Pacific, and Greenland at lags of up to 10 days (Figures 4.1a,b), and have little influence over the midlatitude circulation at greater lags (Figures 4.1c-e). The midlatitude circulation, however, Granger-causes a significant Arctic temperature response via enhancement of the existing stationary wave pattern at lag day 5 (Figure 4.2a); Z_{500} anomalies over eastern Russia up to lag day 10, Hudson Bay up to lag day 15, and Alaska and the Beaufort Sea at lags of up to 20 days (Figures 4.2b-d). Beginning at lag day 20, the signal over Siberia begins to re-emerge, with positive height anomalies over Siberia and the Barents-Kara Seas driving warm Arctic anomalies at lag days 20-25 (Figure 4.2d,e).

4.3.2 Regional Analysis

The results of Figures 4.1 and 4.2 emphasize the regional variability of Arctic-midlatitude teleconnections. For example, sea ice loss in specific regions has been linked to large-scale midlatitude circulation anomalies. Atlantic and Pacific ice loss produce not only different but opposing responses in the North Atlantic Oscillation (e.g., Sun et al. (2015), Pedersen et al. (2016)); Koenigk et al. (2016) and Screen (2017) provide more extensive regional analyses of the impact of Arctic sea ice loss on the midlatitude circulation, using correlation analysis on ERA-Interim reanalysis (Koenigk et al. (2016)) and a suite of AGCM experiments forced by sea ice loss (Screen (2017)). We note that these studies focus almost exclusively on the variability of the atmospheric response

to sea ice loss in different regions rather than two-way responses; and that they are primarily concerned with this response on longer timescales than we consider here.

Table 4.1. Region definitions.

Region	Latitude	Longitude
1. Subtropical Atlantic	25-40° N	15-55° W
2. Greenland	55-75° N	0-60° W
3. Siberia	50-75° N	50-100° E
4. West Pacific	45-70° N	120-180° E
5. East Pacific	45-75° N	110-180° W
6. Subtropical Pacific	20-50° N	120-160° W
7. North America	40-65° N	60-100° W

In contrast to previous studies (e.g., Sun et al. (2015), Pedersen et al. (2016), Koenigk et al. (2016), Screen (2017)), we additionally focus on how different regions’ circulation patterns (as represented by Z_{500}) impact pan-Arctic climate on sub-monthly timescales. In this way, we can more closely examine Arctic-midlatitude relationships in terms of two-way feedbacks, and how the midlatitude circulation and the Arctic simultaneously impact each other. To do this, we identify key regions based on the results of Figures 4.1 and 4.2 for regional analysis. The regions of interest are listed in Table 4.1, and they can be geographically identified in Figure 4.6d. Z_{500} is averaged over the area of each region in Table 4.1, giving it the dimensions of $[1 \times \text{time}]$. As in the previous section, T_{polar} is averaged over all longitudes from 70-90° N, with dimensions of $[1 \times \text{time}]$. Thus, instead of applying the LASSO model to each gridpoint separately, we simply have one LASSO model for each region. By simplifying our variables to two time series, we are able to represent our results in graphical form (see Ebert-Uphoff and Deng (2012) for a thorough discussion of the application of graphical methods to climate science). That is, our variables, Z_{500} and T_{polar} are represented as nodes on a graph, while the edges delineate the connections between the nodes. Our regions are defined based on the results of Figures 4.1 and 4.2; nevertheless, they are not overly sensitive to the exact location of the region boundaries (not shown). As in Figures 4.1 and 4.2, the results are presented as standardized regression coefficients ($\frac{\sigma}{\sigma}$).

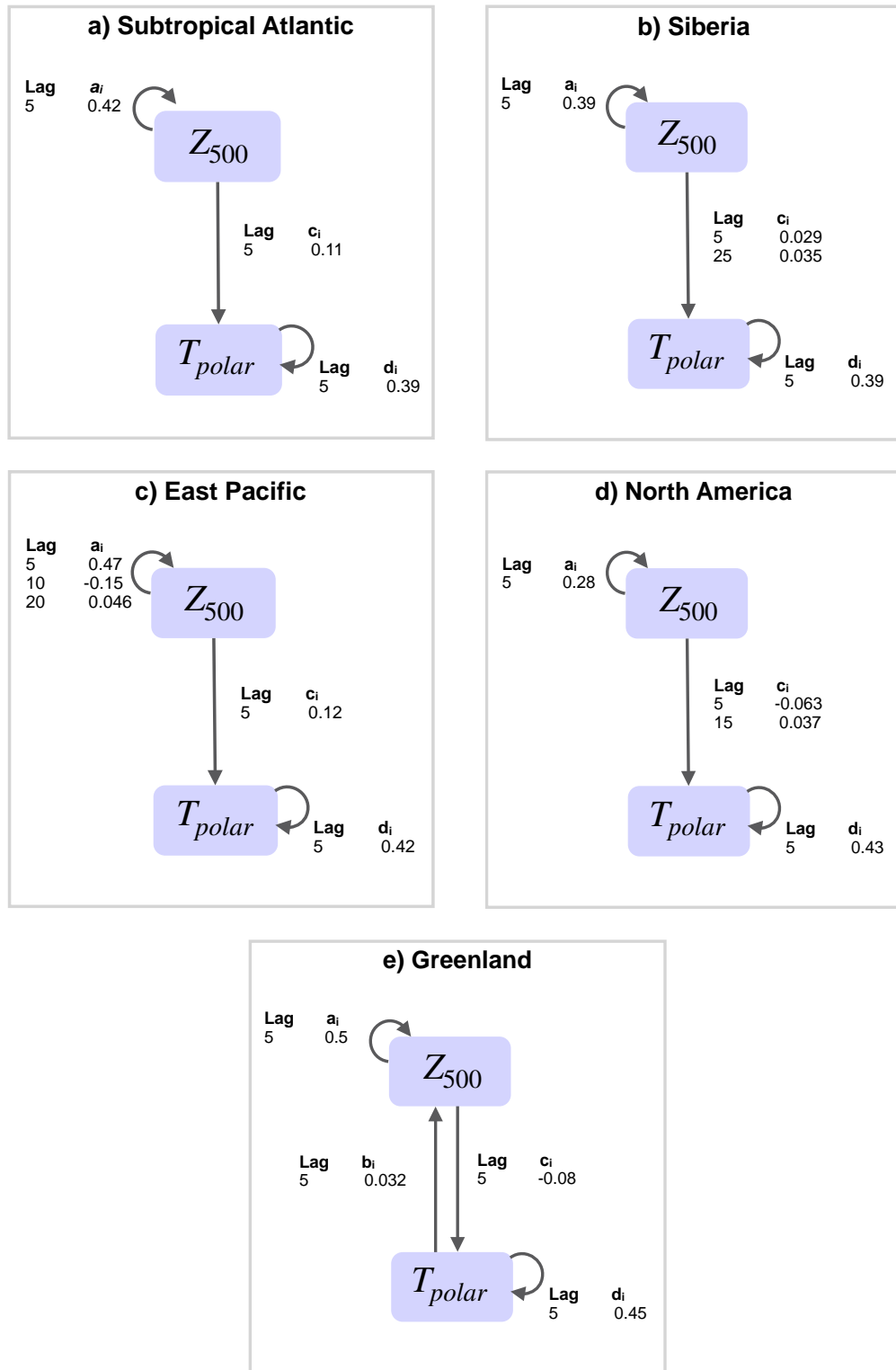


Fig. 4.4. Graphical representation of Arctic-midlatitude causal connections for regions in which Z_{500} drives T_{polar} . Region boundaries are given in Table 4.1. Curved arrows represent autocorrelation, while straight arrows represent the cross-correlation terms.

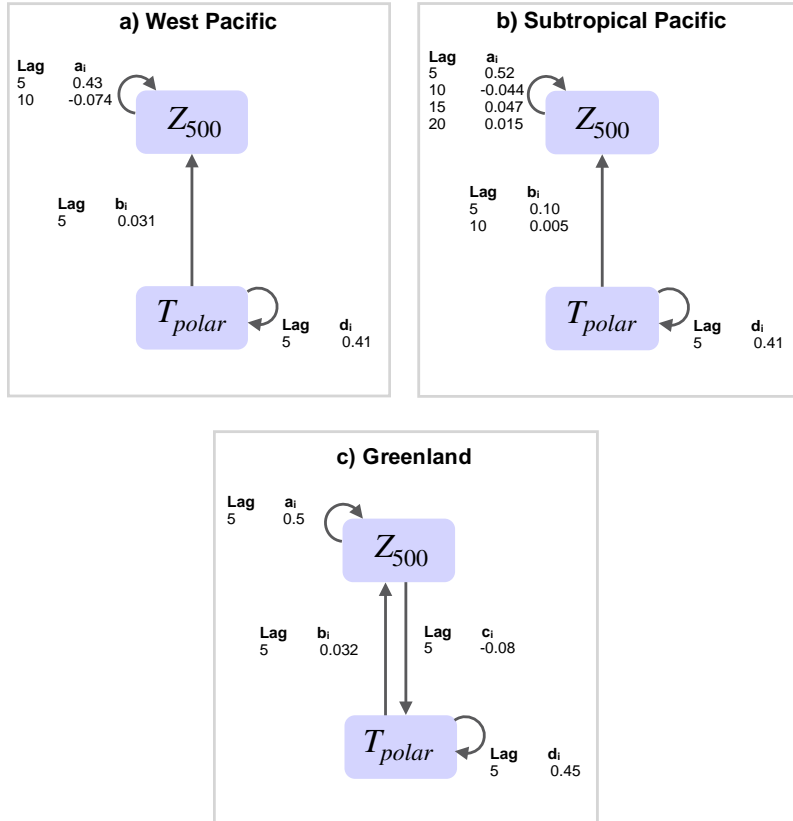


Fig. 4.5. Graphical representation of Arctic-midlatitude causal connections for regions in which T_{polar} drives Z_{500} . Region boundaries are given in Table 4.1. Curved arrows represent autocorrelation, while straight arrows represent the cross-correlation terms.

Figures 4.4 and 4.5 show the results of the one-dimensional LASSO model applied to each region in Table 4.1. Figure 4.4 contains the regions in which Z_{500} drives T_{polar} , while Figure 4.5 contains the regions in which T_{polar} drives Z_{500} ; these relationships will be discussed shortly. Greenland appears in both Figure 4.4 and Figure 4.5 because it shows both Z_{500} driving T_{polar} and T_{polar} driving Z_{500} .

As expected, both Z_{500} and T_{polar} exhibit autocorrelation in all regions (curved arrows in Figures 4.4 and 4.5), with the largest autocorrelation occurring at lag day 5, and decreasing at longer lags. For Z_{500} , at lag day 5, the autoregression coefficients range from 0.28 (about 8% variance explained) to 0.52 (about 27% of variance explained), meaning that for a given region, the circulation explains about 10-25% of its own variance at lag day 5. In some regions (specifically, the west, east, and subtropical Pacific), significant autocorrelation in Z_{500} persists at lags up to 20 days. For

T_{polar} , significant memory only exists up to 5 days, with an autoregression coefficient around 0.4 (about 20% of variance explained).

An examination of the Z_{500} driving T_{polar} (Figure 4.4) and T_{polar} driving Z_{500} (Figure 4.5) coefficients (c and b coefficients in Equation A1) reveals that in most regions, there is one dominant relationship—that is, either Arctic temperatures Granger-cause significant variability in the mid-latitude circulation (Figure 4.5), *or* the midlatitude circulation Granger-causes significant Arctic temperature variability (Figure 4.4). In the subtropical Atlantic, Siberia, the east Pacific, and North America, the midlatitude circulation drives anomalies in Arctic temperature, but Arctic temperature does not drive any significant anomalies in the local circulation in these regions (Figure 4.4a-d; regions 1, 3, 5, and 7 in Table 4.1). Over the subtropical Atlantic, Siberia, and the east Pacific, at lag day 5, high local height anomalies drive warm anomalies in Arctic temperature (Figure 4.4a-c; regions 1, 3, and 5 in Table 4.1). Over North America, at lag day 5, the relationship is opposite—low height anomalies over North America drive warm anomalies in Arctic temperature (Figure 4.4d; region 7 in Table 4.1). At lag day 15, however, high height anomalies over North America drive warm Arctic temperature anomalies. As seen in Figure 4.2e, there is a re-emergence of a signal over Siberia at the longest lags—at lag day 25, high height anomalies over Siberia are also significant drivers of warm Arctic temperature anomalies (Figure 4.4b; region 3 in Table 4.1).

By contrast, over the west and subtropical Pacific, Arctic temperature predominantly drives a response in Z_{500} (Figure 4.5). Warm Arctic temperature anomalies drive positive Z_{500} anomalies at lag day 5 for both regions, and lag day 10 for the subtropical Pacific (Figure 4.5a,-b; regions 4 and 6 in Table 4.1). Greenland (represented in both Figures 4.4e, 4.5c; region 2 in Table 4.1) is the one region that does show a two-way feedback—at lag day 5, warm Arctic temperature anomalies drive high Z_{500} anomalies over Greenland; which drive cold Arctic temperature anomalies in 5 days time. The strength of the regression coefficient (in units of $\frac{\sigma}{\sigma}$) for Z_{500} driving T_{polar} is more than double that of T_{polar} driving Z_{500} , suggesting that this two-way feedback is not of equal strength.

Figure 4.6 summarizes the results of Figures 4.4, 4.5 in the form of maps. All regions show at least one causal relationship at lag day 5 (Figure 4.6a), while the connections are much more

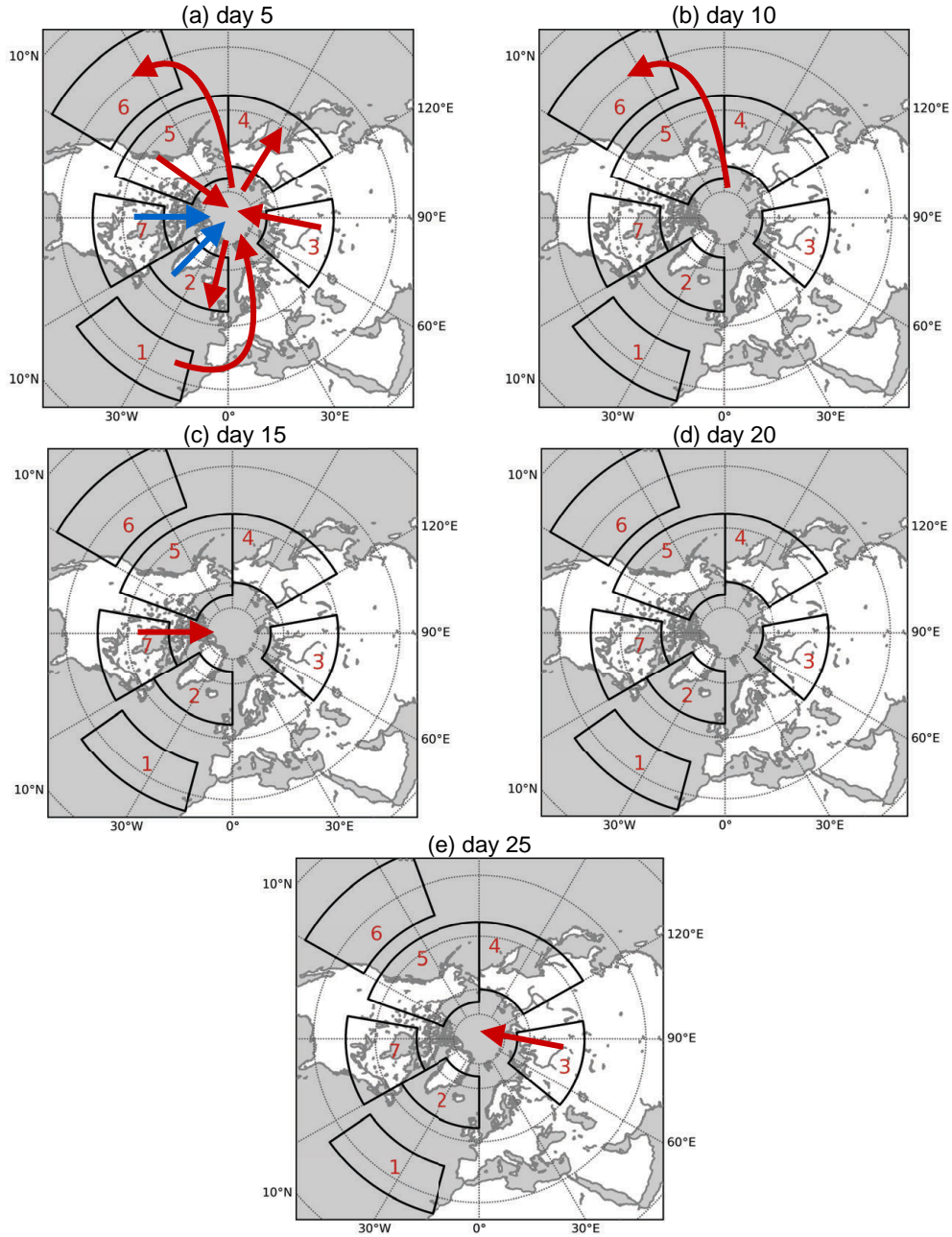


Fig. 4.6. Simplified schematic of LASSO model results for Arctic-midlatitude causal connections at lags of (a) 5 to (e) 25 days. Arrows pointing into the Arctic indicate regions in which the local circulation (Z_{500}) is a Granger-cause of Arctic temperatures; arrows pointing out of the Arctic indicate regions in which Arctic temperature is a Granger-cause of the local circulation (Z_{500}). Colors indicate the sign of the relationship—red arrows indicate a positive regression coefficient (warm Arctic temperature anomalies drive high geopotential height anomalies, and high height anomalies drive warm Arctic temperature anomalies), while blue arrows indicate a negative regression coefficient (warm Arctic temperature anomalies drive low geopotential height anomalies, and low height anomalies drive warm Arctic temperature anomalies).

limited at longer lags. There are causal connections not only between the Arctic and the continental midlatitude regions, but also the Arctic and the subtropical ocean basins. Arctic temperatures do not impact variability in Z_{500} beyond lag day 10 (Figure 4.6b), while the circulation in some regions impacts Arctic variability up to lag day 25 (Figure 4.6e). Greenland is the only region that shows two-way feedbacks (at lag day 5; Figure 4.6a); in all the other regions studied in Figure 4.6, one direction dominates.

4.4 DISCUSSION

The results of the LASSO model applied to T_{polar} and Z_{500} emphasize several points. First, we note that the regions in which Arctic temperature is a Granger-cause of variability in Z_{500} are different from the regions in which Z_{500} Granger-causes variability in Arctic temperature. In fact, the LASSO model suggests that on sub-monthly timescales, many midlatitude regions influence Arctic temperatures rather than are influenced by them. Targeted modeling studies that primarily explore the atmospheric response to Arctic warming or sea ice loss have many advantages, chief among them being that they encourage the thorough testing of physical hypotheses. However, both directions of influence must be considered in order to comprehensively understand the full implications of Arctic-midlatitude teleconnections, thus emphasizing the advantages of approaches like the LASSO model outlined here.

As an example, in recent years, reanalyses have shown a marked cooling and high pressure anomaly over Siberia (e.g., Ogawa et al. (2018)). The role of Arctic amplification and sea ice loss in driving this particular feature has been a topic of some scientific interest, with several studies suggesting that anomalously warm Arctic temperatures and/or anomalously low sea ice concentrations (particularly in the Barents-Kara Sea region) could be responsible for driving these cold temperature and high pressure anomalies over Siberia on interannual timescales (e.g., Honda et al. (2009), Inoue et al. (2012), Tang et al. (2013), Mori et al. (2014), Kug et al. (2015), Overland et al. (2015), Luo et al. (2016)). These studies primarily apply composite analysis (Inoue et al. (2012), Overland et al. (2015), Luo et al. (2016)) or regression or correlation-based models (Honda et al.

(2009), Tang et al. (2013), Kug et al. (2015), Overland et al. (2015), Luo et al. (2016)) to reanalysis output. While these approaches can show covariability, their capability in determining the direction of the relationship is limited—that is, they can show that warm Arctic temperatures or low sea ice are correlated with cold temperatures or high pressures over Siberia, but they struggle to establish which process drives which in the presence of autocorrelation.

It is in such situations that an approach based in Granger causality, such as the LASSO model utilized in this study, may provide a more robust assessment of causality. The existence of a Granger-causal relationship is established based on the predictor's ability to explain additional variance beyond the autocorrelation of the predictand, imposing a more stringent criteria for establishing a significant relationship (e.g., Runge et al. (2014), McGraw and Barnes (2018)). Indeed, our results provide evidence that rather than warm Arctic temperature anomalies driving a strengthening of the Siberian high, it is in fact the other way around—a stronger Siberian high drives a warm temperature anomaly in the Arctic on sub-monthly timescales. Several recent studies using large ensembles of climate model simulations (e.g., McCusker et al. (2016), Sun et al. (2016), Ogawa et al. (2018)) have also suggested that Arctic warming and sea ice loss do not drive significant continental cooling or high pressure responses over Eurasia—rather, the observed cooling is simply a manifestation of internal variability. Current studies of sea ice reductions (e.g., Luo et al. (2017), Kelleher and Screen (2018)) and extreme Arctic temperature events (e.g., Messori et al. (2018)) in reanalysis have also hypothesized that high pressure over Eurasia drives a large response in the Arctic on daily to monthly timescales.

The LASSO model results presented here have several novel advantages. This approach can be applied to both climate model output and reanalysis, allowing for a more straightforward comparison between the two. Since the LASSO model is based on a Granger causality approach, it is able to make a stronger statement about causal relationships between Arctic temperatures and the midlatitude circulation than a standard lagged linear regression approach. Specifically, the Granger causality approach also allows the midlatitude atmosphere to feed back upon and modify the Arctic climate—a pathway that is not fully represented in many targeted modeling studies, as they force Arctic temperatures or sea ice to a certain state. Furthermore, the LASSO model as formulated

here inherently takes regional variability into account (Figures 4.1 and 4.2), without having to run large numbers of model simulations.

While there are many advantages to the Granger causality approach employed in this study, we note several important caveats. First, this study is focused entirely on timescales of 25 days or fewer—we do not make any claims regarding interannual or decadal variability, or how these relationships might change in the face of climate change. Our emphasis on sub-monthly timescale variability also means that we do not explore the hypothesis that Arctic warming indirectly affects the tropospheric circulation by disturbing the stratospheric polar vortex (e.g., Sun et al. (2015), Wu and Smith (2016), Zhang et al. (2018b), Zhang et al. (2018a)). Second, we note that the regression coefficients in Figures 4.1, 4.2, 4.4, and 4.5 are small, with Z_{500} explaining at most around 1% of additional variance of Arctic temperature, and vice versa. Some of this is likely due to the nature of the LASSO regression, which acts to reduce the values of the regression coefficients overall (e.g., Hastie et al. (2015)); the VAR results, without the LASSO regularization criteria applied, do exhibit somewhat larger values for regression coefficients (see Appendix A). However, the overall low values of regression coefficients are consistent with the results of Barnes and Simpson (2017), who found that Arctic temperatures explained only 1-3% of additional variance in the midlatitude jet streams on subseasonal timescales—that is, compared to internal variability, the strength of these Arctic-midlatitude teleconnections is not especially large.

4.5 CONCLUSIONS

We have applied a regularized regression model formulated on Granger causality, and its emphasis on added predictive power, to MERRA-2 reanalysis to study sub-monthly relationships between Arctic temperatures and the midlatitude circulation. The regularized regression model shows evidence of both Arctic temperatures driving midlatitude circulation responses, and midlatitude circulation driving Arctic temperature responses, but rarely in the same location. Arctic temperatures primarily drive circulation responses over the Pacific and Greenland at lags of 10 days or shorter; we do not see evidence of Arctic temperatures driving significant responses over North America or most of Eurasia on sub-monthly timescales. When we focus on specific regions, we

find that the circulation in most regions is either driven *by* Arctic temperatures (the west Pacific, the subtropical Pacific), or is a *driver* of Arctic temperatures (the subtropical Atlantic, Siberia, the east Pacific, North America). In particular, our results over Siberia support the hypothesis that recent observed Eurasian cooling and high pressure anomalies are not driven by warm Arctic anomalies, but rather are drivers of warm Arctic temperature anomalies. Greenland is the exception, and the only region in which the regularized regression model shows evidence of two-way feedbacks on sub-monthly timescales. We emphasize that the midlatitude circulation drives significant variability in Arctic temperatures as well, and must be considered when fully evaluating Arctic-midlatitude dynamics.

The authors thank Savini Samarasinghe and Imme Ebert-Uphoff for their essential assistance in developing and implementing the VAR and LASSO models used in this paper, and for their always helpful discussions of and improvements to our causal discovery methods. Randal Barnes aided us in the implementation of the VAR model. Thanks also to Jingyuan Li for suggestions and feedback regarding this manuscript. The MERRA-2 data used in this study have been provided by the Global Modeling and Assimilation Office (GMAO) at NASA Goddard Space Flight Center. MCM and EAB are supported by the National Science Foundation under grants AGS-1545675 and AGS-1749261.

5 Changes in Arctic Moisture Transport Over the North Pacific Associated with Sea Ice Loss¹

Recent work has emphasized the important role of midlatitude moisture fluxes in enhancing Arctic warming and sea ice loss. Conversely, less attention has been paid to the impact of Arctic warming and sea ice loss on midlatitude moisture fluxes. Analysis of an atmosphere-only general circulation model indicates that sea ice loss promotes changes in the large-scale midlatitude atmospheric circulation that have a substantial impact on moisture transport into and out of the Arctic. While poleward moisture transport into the Arctic does increase in a reduced sea ice climate, the increase in equatorward moisture transport out of the Arctic is larger, particularly in boreal winter over the North Pacific. A decomposition of the meridional moisture transport reveals that this increase in equatorward moisture transport is driven, at least in part, by changes in the background circulation. Specifically, sea ice loss drives a series of large-scale tropospheric circulation changes, including an increase in cyclonic Rossby wave breaking over the North Pacific that results in a preferential enhancement of equatorward moisture transport out of the Arctic.

5.1 INTRODUCTION

Arctic temperatures have increased substantially faster than the global mean surface temperature in recent decades, a phenomenon known as Arctic amplification (e.g., Serreze and Barry (2011), Cohen et al. (2014), Walsh (2014)). Climate model projections indicate that Arctic amplification will continue as global temperatures rise (e.g., Manabe and Stouffer (1980), Hansen et al. (1984), Holland and Bitz (2003), Collins et al. (2013)). This warmer Arctic is accompanied by sea ice loss, and thus, further warming due to an increase in absorbed solar radiation, increased heat exchange between the ocean and the atmosphere, and other processes (e.g., Manabe and Wetherald (1975), Deser et al. (2010), Serreze and Barry (2011), Serreze et al. (2012), Kapsch et al. (2016),

¹This chapter contains material that has been submitted to *Climate Dynamics* as: McGraw, M.C., Baggett, C.F., Liu, C., and B.D. Mundhenk: Changes in Arctic moisture transport over the North Pacific associated with sea ice loss, *Climate Dynamics*, submitted 02/2019.

Burt et al. (2016)).

Atmospheric water vapor can also substantially impact Arctic temperatures. The water vapor feedback is described by the Clausius-Clapeyron relationship—as temperatures increase, the atmosphere is capable of holding more water vapor (e.g., Held and Soden (2006)). Because atmospheric water vapor is a highly effective greenhouse gas, it can trap outgoing longwave radiation and re-emit that radiation downward, leading to surface warming (e.g., Francis and Hunter (2006), Burt et al. (2016)). Even small increases in atmospheric water vapor could have a large impact on Arctic climate through a positive feedback loop where surface warming induces sea ice loss and a subsequent enhancement of latent heat fluxes (and thus, atmospheric water vapor) from the ocean to the atmosphere, ultimately leading to further warming (e.g., Screen and Simmonds (2010), Ghatak and Miller (2013), Burt et al. (2016)).

Increased atmospheric water vapor in the Arctic has been linked to moist intrusions from lower latitudes. These intrusions lead to a reduction in sea ice extent and thickness (e.g., Park et al. (2015a), Park et al. (2015b), Woods and Caballero (2016), Mortin et al. (2016), Burt et al. (2016)); an earlier melt onset for sea ice (e.g., Park et al. (2015b), Mortin et al. (2016)); changes in Arctic surface temperature variability (e.g., Woods et al. (2013), Messori et al. (2018)); and an increase in upper ocean heat content (e.g., Park et al. (2015a)). Moist intrusions into the Arctic are closely related to the midlatitude and tropical circulations through Rossby wave breaking and atmospheric blocking (e.g., Woods et al. (2013), Liu and Barnes (2015)), atmospheric rivers (e.g., Newman et al. (2012), Baggett et al. (2016)), planetary wave activity (e.g., Goss et al. (2016), Graversen and Burtu (2016), Franzke et al. (2016)), and tropical convection (e.g., Lee (2014), Baggett and Lee (2017)). Changes in moisture transport into the Arctic also have strong implications for the Arctic's future climate, as moisture transport into the Arctic is expected to increase in a warmer climate (e.g., Serreze and Barry (2005), Graversen (2006), Langen and Alexeev (2007)). Thus, changes in circulation that affect Arctic moisture transport could directly impact future Arctic warming.

While the midlatitude circulation can substantially impact moisture transport into the Arctic, a warmer Arctic can alter the midlatitude circulation itself. In prior work, a warmer Arctic has been linked to changes in extreme temperature events (e.g., Screen et al. (2015a), Ayarzagüena

and Screen (2016)), reductions in overall temperature variability (e.g., Screen (2014), Blackport and Kushner (2017)), and an equatorward shift and weakening of the midlatitude jet streams (e.g., Deser et al. (2010), Butler et al. (2010), Screen et al. (2018)), although the subtleties of these responses have been refined more recently (e.g. Peings et al. (2017), Ronalds et al. (2018), Zappa et al. (2018)). Arctic warming has also been connected to changes in midlatitude sea level pressure and 500 hPa geopotential heights (e.g., Overland et al. (2015), Blackport and Kushner (2017), Screen et al. (2018), Zappa et al. (2018)), planetary wave patterns (e.g., Francis and Vavrus (2015)), and the warm Arctic-cold continents pattern (e.g., Kug et al. (2017)), although some of these connections have been debated (e.g. Barnes (2013), Barnes and Screen (2015), McCusker et al. (2016), Sun et al. (2016)). Recent work has also suggested that the Arctic is capable of influencing the midlatitudes indirectly via changes in the stratospheric polar vortex (e.g., Sun et al. (2015), Wu and Smith (2016), Kretschmer et al. (2016)). The Arctic's ability to influence the midlatitudes can be modulated by changes in the background state of the ocean (e.g., Deser et al. (2016), Screen and Francis (2016), Sung et al. (2016), Smith et al. (2017)) and sea ice (e.g., Screen (2017), Screen et al. (2018)). Ultimately, these changes in the midlatitude circulation can feed back upon the Arctic, further modifying Arctic weather and climate.

The midlatitude circulation can warm the Arctic via moisture intrusions, and changes in Arctic climate can modify the midlatitude circulation. Thus, if the Arctic can drive changes in the midlatitude circulation, do these changes in the midlatitude circulation further modify moisture transport into the Arctic? We explore this question using a set of atmosphere-only general circulation model simulations from Sun et al. (2015), described in more detail in Section 2. In Section 2, we define moisture transport into and out of the Arctic and briefly explain our Rossby wave breaking detection algorithm. In Section 3, we discuss our key results linking the response of the large-scale, midlatitude circulation to changes in Arctic moisture fluxes, including changes in the behavior of the eddy-driven jet and Rossby wave breaking. We summarize our results in Section 4.

5.2 METHODS

5.2.1 Climate Model Experiments

Our analysis is conducted on the output of a pair of atmospheric general circulation model experiments performed by Sun et al. (2015). Both experiments use the Community Atmospheric Model, version 4 (CAM4), with a horizontal resolution of 1.9° latitude by 2.5° longitude, 26 vertical levels from the surface to 3.5 hPa, and prescribed stratospheric ozone. The first experiment, which we denote as CTRL (CONTROL in Sun et al. (2015)), is forced with a prescribed sea ice concentration (SIC) and sea surface temperature (SST) that have been derived from the average over the years 1980-1999. The SIC and SST seasonal cycles are obtained from the average of a three-member ensemble of twentieth-century simulations of the fully coupled version of the Whole Atmosphere Chemistry-Climate Model (WACCM). The second experiment, which we denote as PERT (TOTAL in Sun et al. (2015)), is forced with SIC and SST derived from the years 2080-2099. The 2080-2099 SIC and SST are calculated from a one-member fully coupled 21st century WACCM experiment under Representative Concentration Pathway 8.5 (RCP8.5) conditions, the scenario with highest warming carried out in the Climate Model Intercomparison Project, Version 5 (CMIP5) studies. At gridpoints where CTRL has sea ice but PERT does not, SSTs are prescribed from the WACCM RCP8.5 simulation. In both scenarios, sea ice has a prescribed thickness of 2 meters, and there are no changes in Antarctic sea ice, although we note that changes in sea ice thickness are a critical component of Arctic warming (e.g., Burt et al. (2016)). We use 40 years of daily mean model output to explore the subseasonal circulation changes associated with sea ice loss. When we compared the changes in the circulation with 40 and 60 years of daily mean model output, we drew similar conclusions. The difference in SIC (Figure 5.1a) and 1000 hPa temperature (Figure 5.1b) in the boreal cold season (September-February, hereafter SONDJF) between PERT and CTRL can be seen in Figure 5.1.

The CAM4 simulations analyzed here are low-top simulations—that is, their highest pressure level is only at 3.5 hPa. Moreover, their vertical resolution is relatively coarse, meaning that CAM4’s stratospheric dynamics are not as well-resolved as those in a high-top model like

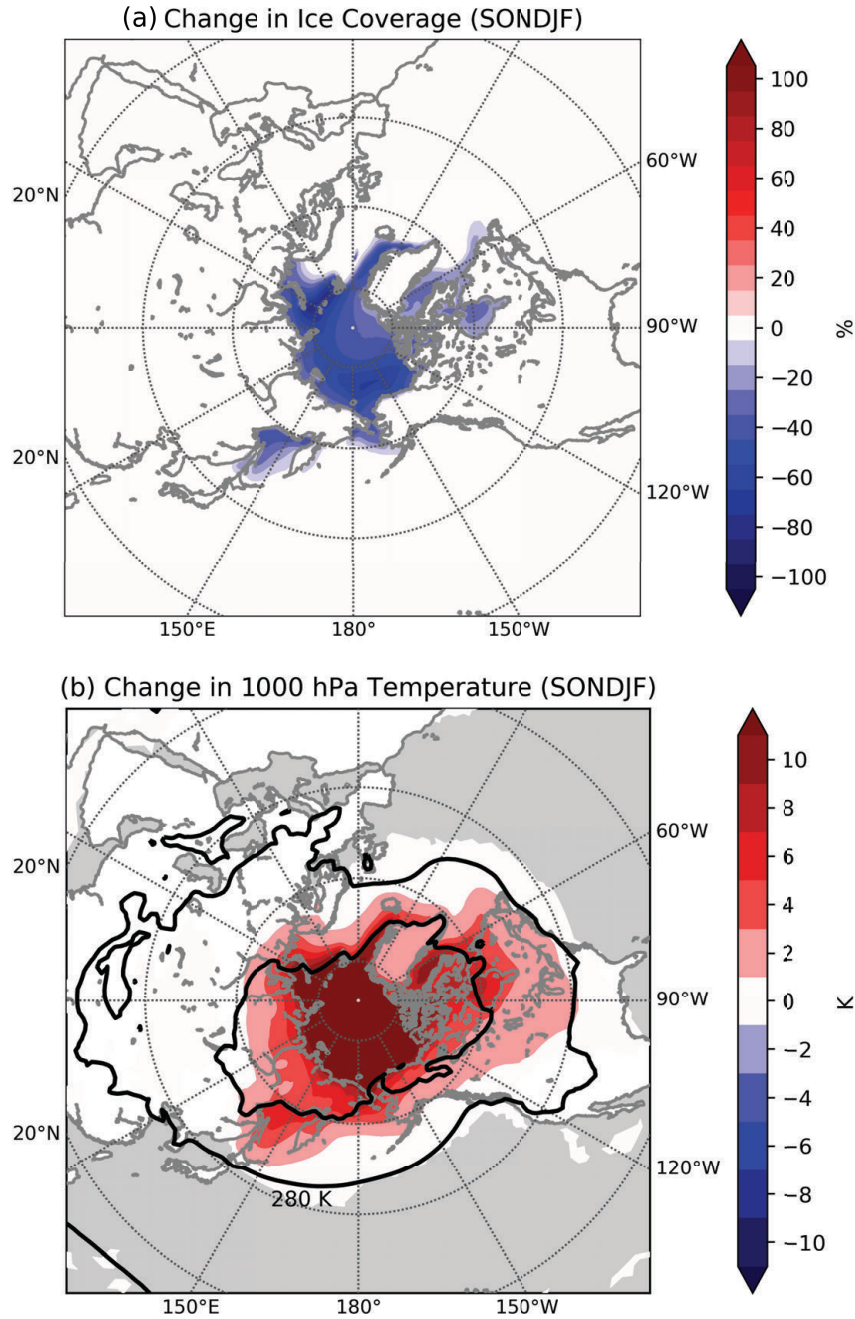


Fig. 5.1. (a) Change (PERT - CTRL) in percent of grid box covered by sea ice for associated with sea ice loss in SONDJF. (b) Change (PERT - CTRL) in 1000 hPa temperature. Only gridpoints where the changes in temperature are significant at 95% confidence are shaded. Black contours show the 1000 hPa temperature in CTRL, contoured every 20 K from 260 to 300 K.

WACCM. These features are noteworthy, as prior studies have found that the stratospheric polar vortex can influence the tropospheric response to sea ice loss and Arctic warming (e.g., Peings and Magnusdottir (2014), Kim et al. (2014), Feldstein and Lee (2014), Wu and Smith (2016)). However, a comparison between the low-top CAM4 and the high-top WACCM indicates that, while the magnitude of the tropospheric response to sea ice loss is weaker in CAM4 as compared to WACCM, the overall pattern of the response is similar in both models (Sun et al. (2015)). In addition, previous work has highlighted the importance of planetary-scale wave activity, as well as primarily tropospheric phenomena in understanding the atmospheric circulation response to sea ice loss (e.g., McKenna et al. (2018)). Therefore, our analysis is conducted under the assumption that the overall structure of the circulation and moisture flux responses to sea ice loss are largely robust to using the low-top model versus the high-top model.

5.2.2 Defining IVT

In this work, moisture transport is measured using vertically integrated water vapor transport ($I\vec{V}T$). $I\vec{V}T$ is calculated according to Mundhenk et al. (2016),

$$I\vec{V}T = \left(\frac{1}{g} \int_{1000}^{300} u q dp \right) \hat{i} + \left(\frac{1}{g} \int_{1000}^{300} v q dp \right) \hat{j}, \quad (5.1)$$

where g is the gravitational acceleration, u is zonal wind, v is meridional wind, q is specific humidity, and dp is the pressure difference between adjoining pressure levels. Here, we integrate from 1000 to 300 hPa, but $I\vec{V}T$ is not highly sensitive to the upper or lower boundaries of the integral, as the largest values of water vapor are primarily confined to the lowest levels of the atmosphere, and the largest contributions to $I\vec{V}T$ derive from the ocean basins. In Figure 5.2, we diagnose total moisture transport into and out of the Arctic by focusing only on the meridional (\hat{j}) component of $I\vec{V}T$ averaged along 70° N, which we will simply refer to as meridional IVT. We will also decompose meridional IVT into poleward and equatorward components. In this decomposition, poleward IVT refers to the daily average of vq across all grid points along 70° N such that we set $vq = vq$ at grid points where $v > 0$ and $vq = 0$ at grid points where $v \leq 0$.

Conversely, we define equatorward IVT as the daily average of vq across all points along 70° N such that $vq = vq$ at grid points where $v \leq 0$ and $vq = 0$ at grid points where $v > 0$.

5.2.3 Rossby Wave Breaking Algorithm

Rossby wave breaking events are identified with the algorithm of Liu et al. (2014), which is based on that of Strong and Magnusdottir (2008). Briefly, potential temperature is interpolated to the 2-potential vorticity unit (PVU, $1 \text{ PVU} = 10^{-6} \text{ K kg}^{-1} \text{ m}^{-2} \text{ s}^{-1}$) surface. The 2-PVU surface serves as an approximation for the tropopause in the extratropics and is useful for diagnosing Rossby wave breaking events (e.g. Franzke et al. (2011), Liu and Barnes (2015)). The algorithm diagnoses Rossby wave breaking events by identifying regions of overturning potential temperature contours on the 2-PVU surface whose enclosed areas exceed a certain threshold (i.e., greater than 25° in an equirectangular projection). Rossby wave breaking events are classified as anticyclonic or cyclonic wave breaking events based on their direction of overturning. In the Northern Hemisphere, anticyclonic Rossby wave breaking events occur when cresting waves are tilted in a southwest to northeast orientation and overturn in a clockwise direction. Cyclonic Rossby wave breaking events occur when cresting waves are tilted in a southeast to northwest orientation and overturn in a counterclockwise direction (see Figure 5 in Liu and Barnes (2015) for an example of each).

5.3 RESULTS

5.3.1 Changes in Meridional IVT

The seasonal and longitudinal variability of meridional IVT across 70° N is explored in Figure 5.2. Figure 5.2 shows the changes in total meridional (black lines), poleward (red lines), and equatorward (blue lines) IVT across 70° N associated with sea ice loss (that is, PERT - CTRL). The results of Figure 5.2 are not highly sensitive to the 70° N boundary and are broadly similar for 65° N and 60° N (Figure 5.10, 5.11). Poleward IVT increases in PERT as compared to CTRL (red line in Figure 5.2a), particularly in September-February (SONDJF). This increase in poleward IVT into the Arctic suggests a positive relationship between sea ice loss and moisture fluxes, in

which sea ice loss (Figure 5.1a) is associated with an increase in moisture transport into the Arctic, which could lead to an increase in downwelling longwave radiation and warmer Arctic temperatures. However, PERT also shows an increase in equatorward IVT across 70° N—that is, moisture flux *out* of the Arctic (blue line in Figure 5.2a). The equatorward IVT actually increases *more* than the poleward IVT.

When meridional IVT across 70° N is broken down by longitude (Figure 5.2b) during SONDJF, it is clear that much of the increase in equatorward IVT (blue line in Figure 5.2b) occurs in the North Pacific region (120° E–240° E, indicated by the orange shading in Figure 5.2b), with about 54% of the total equatorward IVT in SONDJF occurring between 120–240° E. As with the Northern Hemisphere mean, this change in equatorward moisture flux in the North Pacific is greatest in SONDJF (blue line in Figure 5.2c). These changes in meridional IVT (vq) can be further understood by breaking down vq into time and zonal means, and their respective anomalies. The time-mean meridional vapor transport, \overline{vq} , is decomposed following equation 4.9 of Peixóto and Oort (1992),

$$\overline{vq} = \overline{v} \cdot \overline{q} + \overline{v'q'} = [\overline{v}] \cdot [\overline{q}] + [\overline{v}] \cdot \overline{q^*} + \overline{v^*} \cdot [\overline{q}] + \overline{v^*} \cdot \overline{q^*} + \overline{v'q'}, \quad (5.2)$$

where $\overline{\quad}$ is the time-mean (defined using calendar-month means), $[\quad]$ represents the zonal-mean, $'$ represents the deviations from the time-mean, and $*$ indicates deviations from the zonal-mean. Taking the zonal-mean of equation 5.2 yields,

$$[\overline{vq}] = [\overline{v}] \cdot [\overline{q}] + [\overline{v^*} \cdot \overline{q^*}] + [\overline{v'q'}], \quad (5.3)$$

Equation 5.3 breaks the time-mean, zonal-mean meridional vapor transport into three terms: a component associated with the mean meridional circulation (MMC, $[\overline{v}] \cdot [\overline{q}]$), a component associated with the stationary eddies ($[\overline{v^*} \cdot \overline{q^*}]$), and a component associated with transient eddies ($[\overline{v'q'}]$). Figure 5.3 shows each of these three components—mean meridional, stationary, and transient—separately (yellow, blue, and red lines in Figure 5.3a, respectively). Figure 5.3a demonstrates that the change in $[\overline{vq}]$ associated with sea ice loss (black line) is largely dominated by the changes in the transient vapor transport ($[\overline{v'q'}]$, red line). We will return to the significance of the transient vapor transport in the discussion of Rossby wave breaking events in Section 3.3.

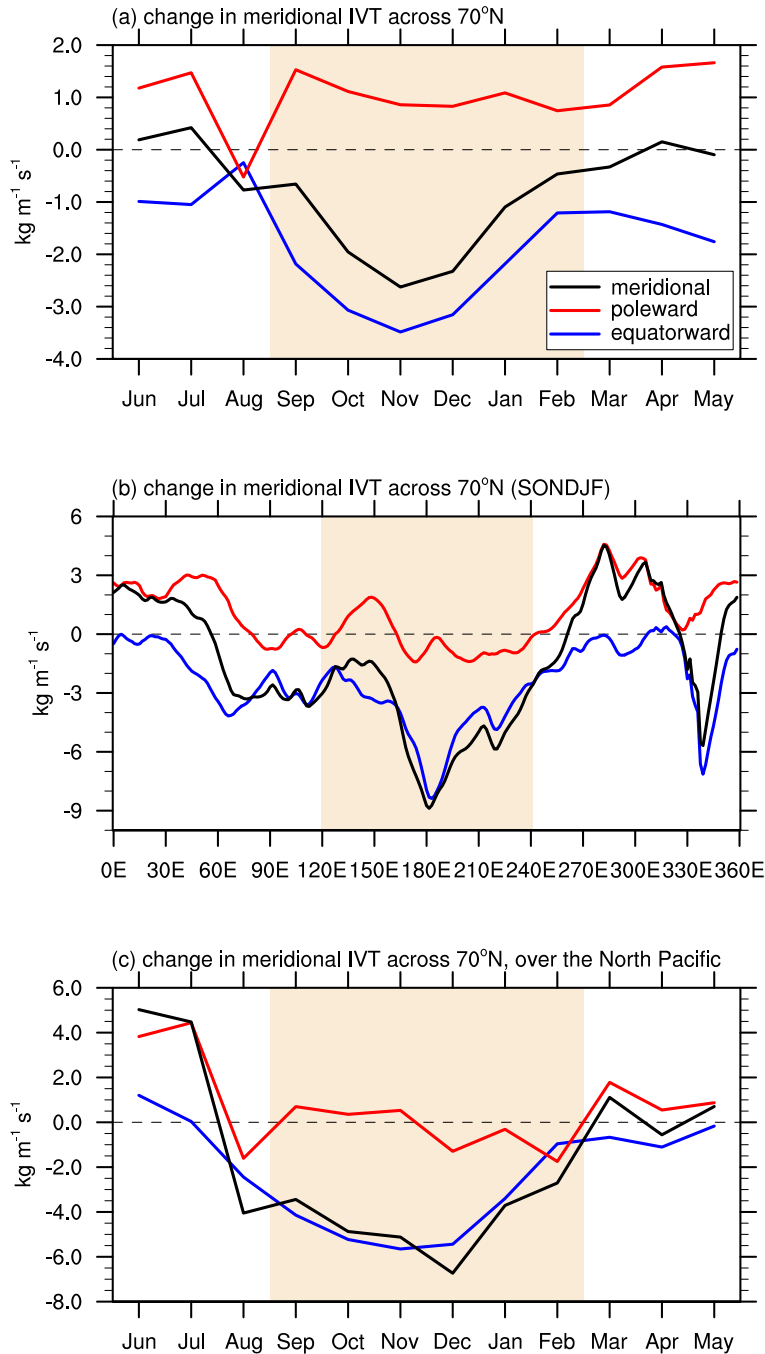


Fig. 5.2. Change (PERT - CTRL) in meridional IVT associated with sea ice loss as a function of (a) month, (b) longitude during SONDJF (highlighted in (a)), and (c) month over the North Pacific region ($120\text{--}240^\circ \text{E}$, highlighted in (b)). Red lines indicate poleward (northward) IVT, blue lines indicate equatorward (southward) IVT, and black lines are the meridional IVT (poleward IVT + equatorward IVT).

In Figure 5.3b, we examine \overline{vq} as a function of longitude (Equation 5.2) during SONDJF. Equation 5.2 indicates that the moisture transport can be divided into a term that describes the advection of the background moisture by the stationary winds ($\overline{v^*} \cdot [\overline{q}]$; dashed blue line in Figure 5.3b), and a term that describes the advection of the stationary moisture field by the background meridional winds ($\overline{q^*} \cdot [\overline{v}]$; dashed red line in Figure 5.3b). Figure 5.3b clearly suggests that the advection of the background moisture by the stationary winds ($\overline{v^*} \cdot [\overline{q}]$; dashed blue line) is a much greater contributor to the total change in meridional IVT (black line) than the advection of the stationary moisture field by the background wind ($\overline{q^*} \cdot [\overline{v}]$).

Figure 5.3b emphasizes the importance of $\overline{v^*} \cdot [\overline{q}]$ (the advection of the background moisture by the stationary winds). However, this term could be dominated by either the changes in the background moisture ($[\overline{q}]$) or changes in the stationary meridional winds ($\overline{v^*}$). Thus, we further break down the change in $\overline{v^*} \cdot [\overline{q}]$,

$$\overline{v^*} \cdot [\overline{q}]|_{PERT} - \overline{v^*} \cdot [\overline{q}]|_{CTRL} = 2\Delta\overline{v^*} \cdot \{[\overline{q}]\} + 2\{\overline{v^*}\} \cdot \Delta[\overline{q}], \quad (5.4)$$

where the $\{\}$ indicates the average of both CTRL and PERT (that is, $\{A\} = \frac{A_{PERT} + A_{CTRL}}{2}$), and the Δ indicates half of the difference between PERT and CTRL (that is, $\Delta A = \frac{A_{PERT} - A_{CTRL}}{2}$). Thus, the change in $\overline{v^*} \cdot [\overline{q}]$ (Equation 5.4) can be expressed as the sum of two terms, where the first term represents the change in moisture advection due to the change in stationary winds ($\Delta\overline{v^*} \cdot \{[\overline{q}]\}$; red line in Figure 5.3c), and the second term represents the change in moisture advection due to the change in background moisture ($\{\overline{v^*}\} \cdot \Delta[\overline{q}]$; black line in Figure 5.3c). Figure 5.3c demonstrates that first term dominates, particularly over the North Pacific (highlighted by the orange box in Figure 5.3c), emphasizing the importance of the changes in the meridional winds. That is, the change in meridional IVT derives principally from a change in the circulation rather than background moisture increases associated with sea ice loss.

Figures 5.2 and 5.3 explore the seasonal and geographic variability of meridional IVT across 70° N, and break meridional IVT down across temporal and spatial scales. We see that the largest changes in meridional IVT across 70° N occur in the boreal cold season (SONDJF, Figure 5.2a), and over the North Pacific (120-240° E, Figure 5.2b). A decomposition of meridional moisture

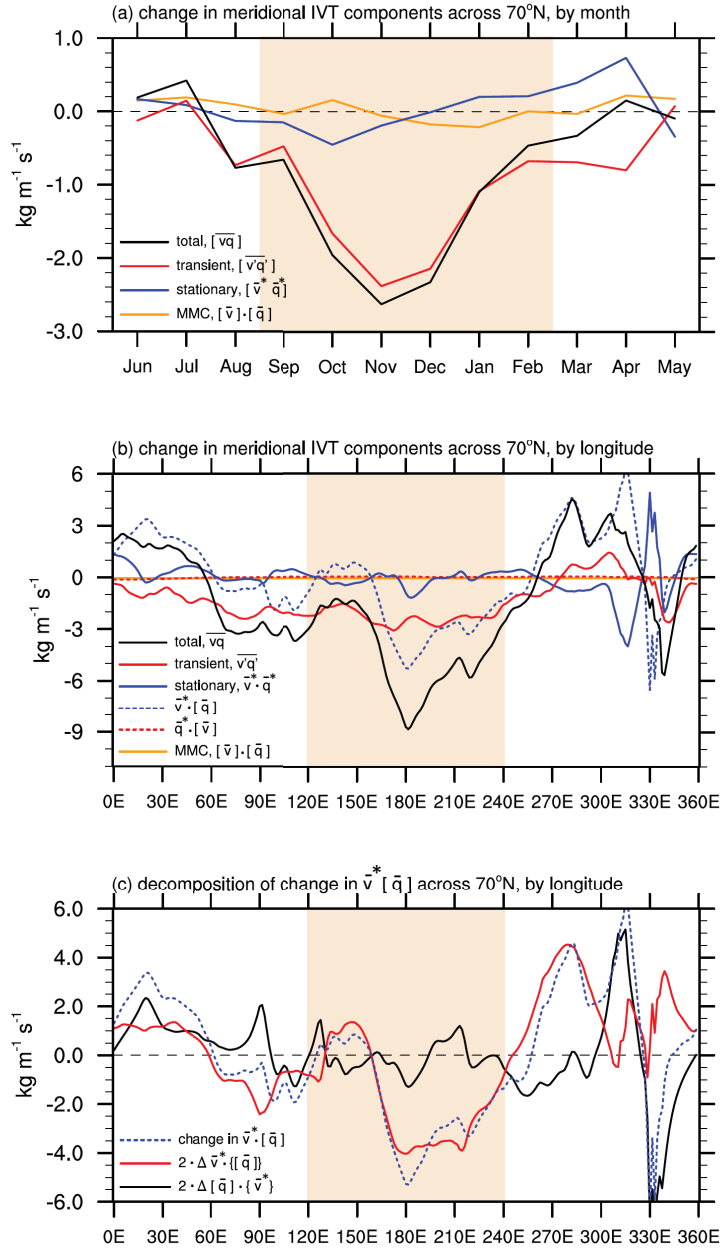


Fig. 5.3. Change (PERT - CTRL) in the components of meridional IVT during SONDJF associated with sea ice loss as a function of (a) month (SONDJF is highlighted in orange), and (b) longitude (the North Pacific is highlighted in orange). In (a), black lines indicate the change in meridional IVT, yellow lines indicate the change in meridional IVT associated with the mean meridional circulation (MMC), red lines indicate the change in meridional IVT associated with the transient waves, and blue lines indicate the change in meridional IVT associated with the stationary waves. In (b), the circulation is broken down further into $\bar{v}^* \cdot [\bar{q}]$ (the advection of background moisture by the stationary meridional winds; dotted blue line) and $\bar{q}^* \cdot [\bar{v}]$ (the advection of the stationary moisture field by the background wind; dotted red line). (c) shows the decomposition of $\bar{v}^* \cdot [\bar{q}]$ into a component associated with the change in meridional winds ($\Delta \bar{v}^* \cdot \{[\bar{q}]\}$, red line) and a component associated with the change in atmospheric water vapor ($\Delta [\bar{q}] \cdot \{\bar{v}^*\}$, black line); orange highlighting indicates the North Pacific.

transport (Equations 5.2-5.3) highlights the role of the transient eddies, and the stationary meridional winds as important components of the overall change in meridional IVT (Figures 5.3b,c). Thus, changes in the circulation associated with sea ice loss are responsible for at least part of the increase in equatorward moisture transport through 70° N. With this in mind, we explore changes in the circulation that could explain Figures 5.2-5.3.

5.3.2 Changes in Large-Scale Circulation

In Figures 4, 5, and 6, we examine changes in the circulation associated with sea ice loss (PERT - CTRL) during SONDJF by focusing on 850 and 300 hPa zonal winds and 500 hPa geopotential heights ($Z500$). Significant changes in the circulation are assessed at 95% confidence using a two-sided student's t -test. In these figures, only gridpoints with significant changes are plotted.

The change in zonal winds at lower (850 hPa, Figure 5.4a) and upper (300 hPa, Figure 5.4b) levels associated with sea ice loss is seen in Figure 5.4. At both 850 and 300 hPa, the largest changes in zonal winds occur poleward of the jet, with a substantial weakening of the winds poleward of about 55° N, and a narrowing and small equatorward shift of the jet. This weakening of the winds on the poleward flank and small equatorward shift of the jet is consistent with recent work associating sea ice loss and Arctic warming with a narrowing of the eddy-driven jet, rather than a pure shift, and a reduction in winds poleward of the jet (e.g., Peings et al. (2017), Ronalds et al. (2018), Zappa et al. (2018)). This broad weakening of the zonal winds on the poleward flank of the jet has implications for the wind shear $\left(-\frac{\partial u}{\partial y}\right)$. As expected from Figure 5.4, the cyclonic wind shear increases between about 40-60° N at both 850 hPa (Figure 5.5a) and 300 hPa (Figure 5.5b). These increases are especially pronounced in the center and western portions of the Pacific, particularly at 300 hPa. This increase in cyclonic wind shear will be linked to changes in Rossby wave breaking in the next section.

As moisture fluxes are largely driven by the mid-level steering pattern, we now turn our attention to the changes in 500-hPa geopotential height ($Z500$) associated with sea ice loss (colored shading in Figure 5.6). As expected, the geopotential height changes over the Arctic are positive,

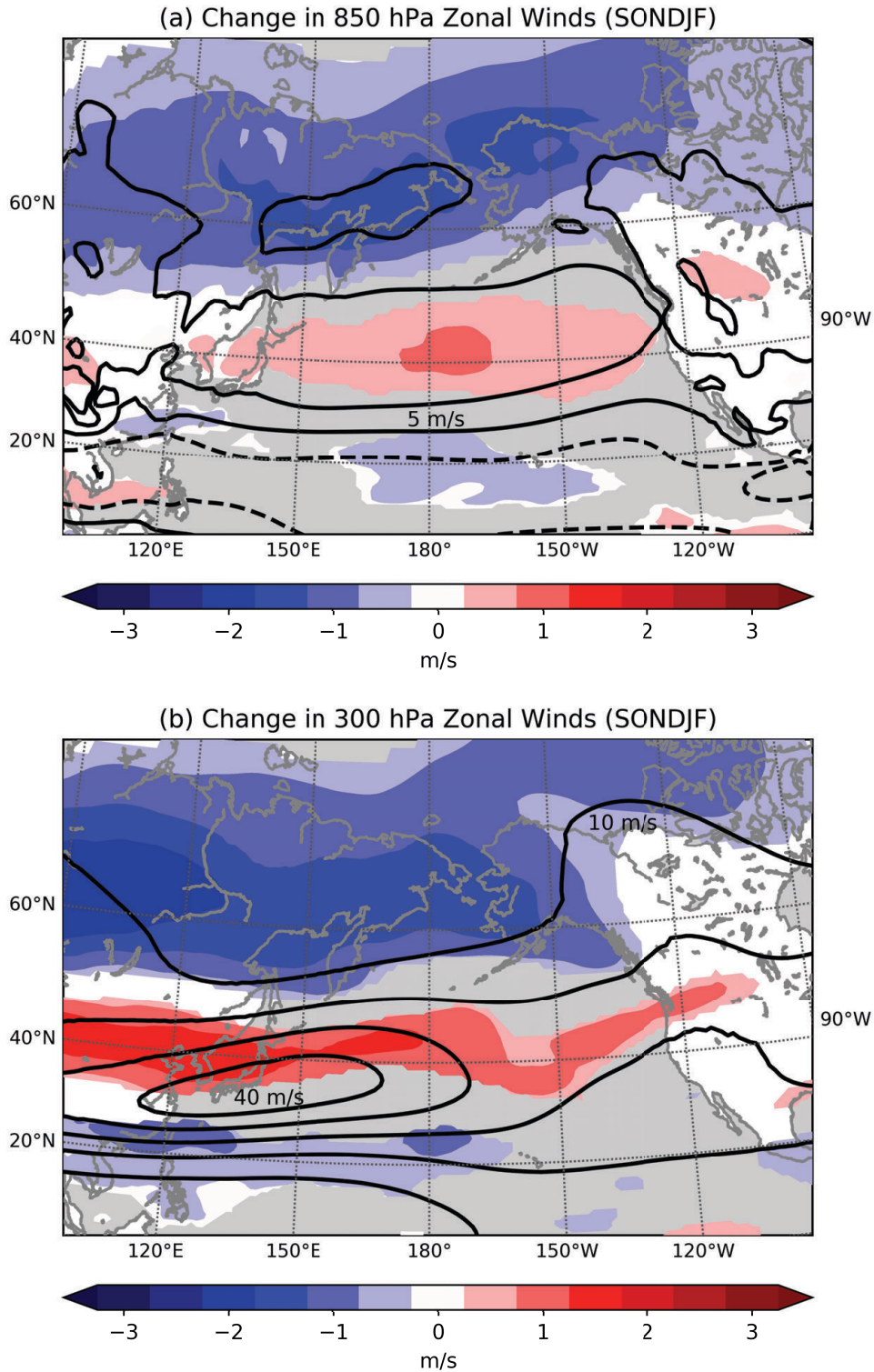


Fig. 5.4. Change (PERT - CTRL) in zonal winds in SONDJF for (a) 850 hPa and (b) 300 hPa. Only gridpoints where the changes in zonal winds are significant at 95% confidence are shaded. Black contours show the zonal winds in CTRL, contoured every 5 m/s from -10 to +10 m/s in (a), and every 10 m/s from 10 to 40 m/s in (b).

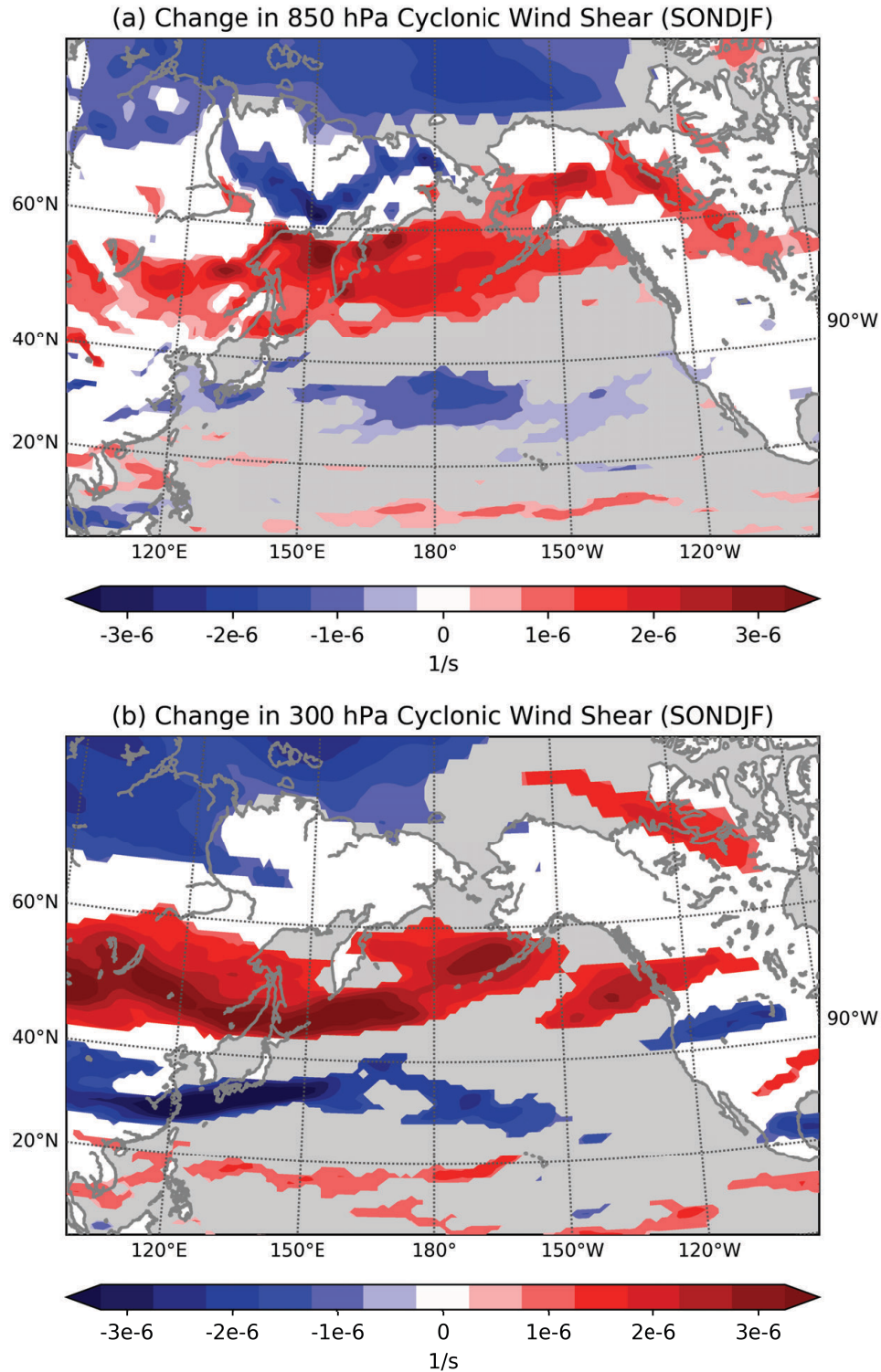


Fig. 5.5. Change (PERT - CTRL) in cyclonic wind shear $\left(-\frac{\partial u}{\partial y}\right)$ at (a) 850 hPa and (b) 300 hPa. Only gridpoints where the changes in wind shear are significant at 95% confidence are shaded.

corresponding to the temperature increases there (Figure 5.1b). In contrast, $Z500$ decreases over interior east Asia, and the eastern half of the North Pacific (roughly corresponding to a strengthening of the Aleutian Low seen in this region in the cold season). Removing the zonal mean component of $Z500$ further emphasizes the role of the zonally asymmetric circulation (Figure 5.6b), whose importance is highlighted in Figure 5.3, where it was shown that changes in $\bar{v}^* \cdot [\bar{q}]$ dominate in the North Pacific. In addition to a strengthening of the low pressure in the Bering Sea and Gulf of Alaska regions seen in Figure 5.6a, Figure 5.6b shows evidence of a strong east-west gradient in $Z500$ between far-eastern Russia and the Bering Strait.

5.3.3 Changes in Rossby Wave Breaking

Thus far, we have observed that there is an increase in equatorward moisture flux (out of the Arctic) associated with sea ice loss over the North Pacific during SONDJF (Figure 5.2). A decomposition of meridional IVT reveals that processes that occur on transient timescales describe most of this increase in equatorward moisture transport (Figure 5.3a) and that changes in the circulation have a substantial impact on the total moisture transport (Figure 5.3b,c). An analysis of changes in the large-scale circulation associated with sea ice loss reveals the following:

- A substantial weakening of the zonal winds poleward of the jet at both lower and upper levels (Figure 5.4);
- An increase in cyclonic wind shear at lower and upper levels, as expected from the weakening of the zonal winds poleward of the jet (Figure 5.5);
- An increase in $Z500$ over the polar cap and a decrease in $Z500$ in the region of the Aleutian low (strengthening an existing quasi-stationary low pressure system; Figure 5.6); and,
- A strong east-west gradient in $Z500$ between far-eastern Russia and the Bering Strait, particularly in the zonally asymmetric component of $Z500$ (Figure 5.6).

These changes in the circulation suggest that Rossby wave breaking could be driving the changes in the meridional moisture transport. Specifically, the increase in cyclonic wind shear on the poleward flank of the jet (Figure 5.5) suggests a corresponding increase in cyclonic Rossby wave breaking in this region (e.g., Thorncroft et al. (1993), Tyrllis and Hoskins (2008)). Additionally, Rossby wave

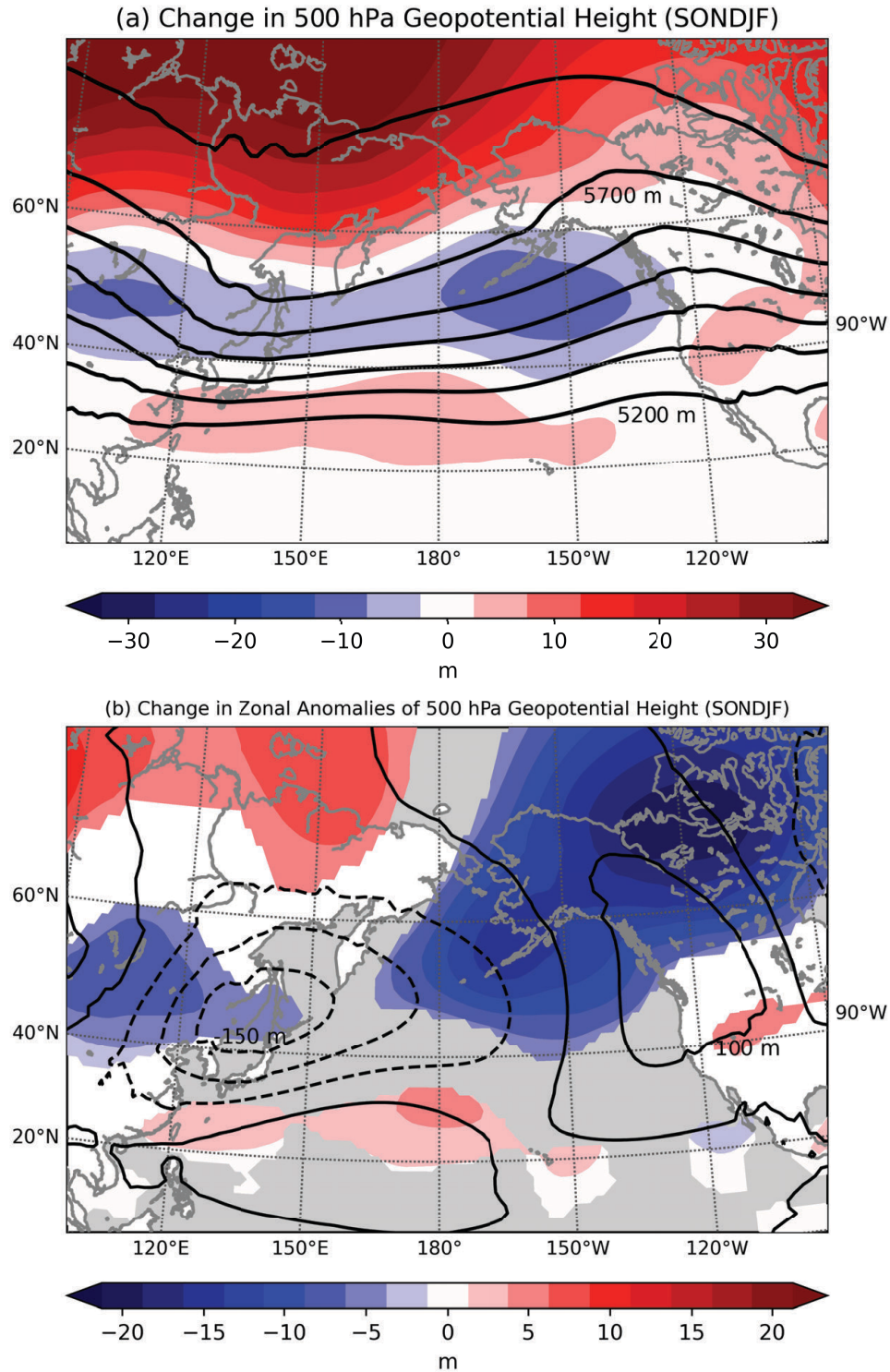


Fig. 5.6. (a) Change (PERT - CTRL) in 500 hPa geopotential height in SONDJF. (b) as in (a), but with the zonal mean removed. Only gridpoints where the changes in 500 hPa geopotential height are significant at 95% confidence are shaded. Black contours in (a) show the geopotential heights in CTRL (contoured every 100m from 5200 to 5800 m); and in (b), with their zonal means removed (contoured every 50 m from -150 to +100 m).

breaking events occur on the transient timescales emphasized in Figure 5.3, further highlighting the possibility of changes in Rossby wave breaking being associated with the increase in equatorward IVT in PERT.

When we calculate the changes in Rossby wave breaking frequency associated with sea ice loss (Figure 5.7), it is clear that there is an increase in cyclonic Rossby wave breaking frequency in the North Pacific (Figure 5.7a) and a corresponding decrease in anticyclonic Rossby wave breaking in the same region (Figure 5.7b). Furthermore, the largest increase in cyclonic Rossby wave breaking occurs on the eastern edge of the Bering Sea, near Kamchatka—corresponding to large increases in cyclonic wind shear (Figure 5.5) and the maximum gradient in $Z500$, particularly in the zonally asymmetric component of $Z500$ (Figure 5.6). Thus, the increase in cyclonic Rossby wave breaking, and a slight westward shift of wave breaking activity compared with CTRL, corresponds with increases in cyclonic wind shear, a narrower and equatorward-shifted jet, and the location of maximum gradients in $Z500$.

While Figures 5.4-5.7 seemingly present a cohesive picture of changes to the large-scale circulation, it must be asked: are the wave breaking events actually driving the moisture fluxes observed in Figures 5.2-5.3, or are they simply coincident with the change in meridional IVT? We address this question by creating lagged composites of moisture transport during cyclonic Rossby wave breaking events. Cyclonic Rossby wave breaking events are classified first by identifying days when cyclonic Rossby wave breaking anomalies exceed one standard deviation over the box $40\text{--}70^\circ\text{ N}$, $150\text{--}200^\circ\text{ E}$ (indicated by the blue lines in Figure 5.7a). Then, only days with the highest amplitude, separated by 14 days from each other, are retained and called cyclonic Rossby wave breaking events. Meridional IVT across 70° N , averaged between 120 and 240° E , is composited at lag days -14 to $+14$ against these events, and divided into poleward and equatorward IVT components. Figure 5.8 shows these anomaly composites for CTRL (Figure 5.8a), PERT (Figure 5.8b), and for their difference (Figure 5.8c). Figure 5.8 shows the variability of both poleward and equatorward moisture fluxes throughout the wave breaking lifecycle.

Previous work (e.g., Liu and Barnes (2015)) has linked cyclonic Rossby wave breaking with more moisture transport into the Arctic. The results shown here may at first glance seem

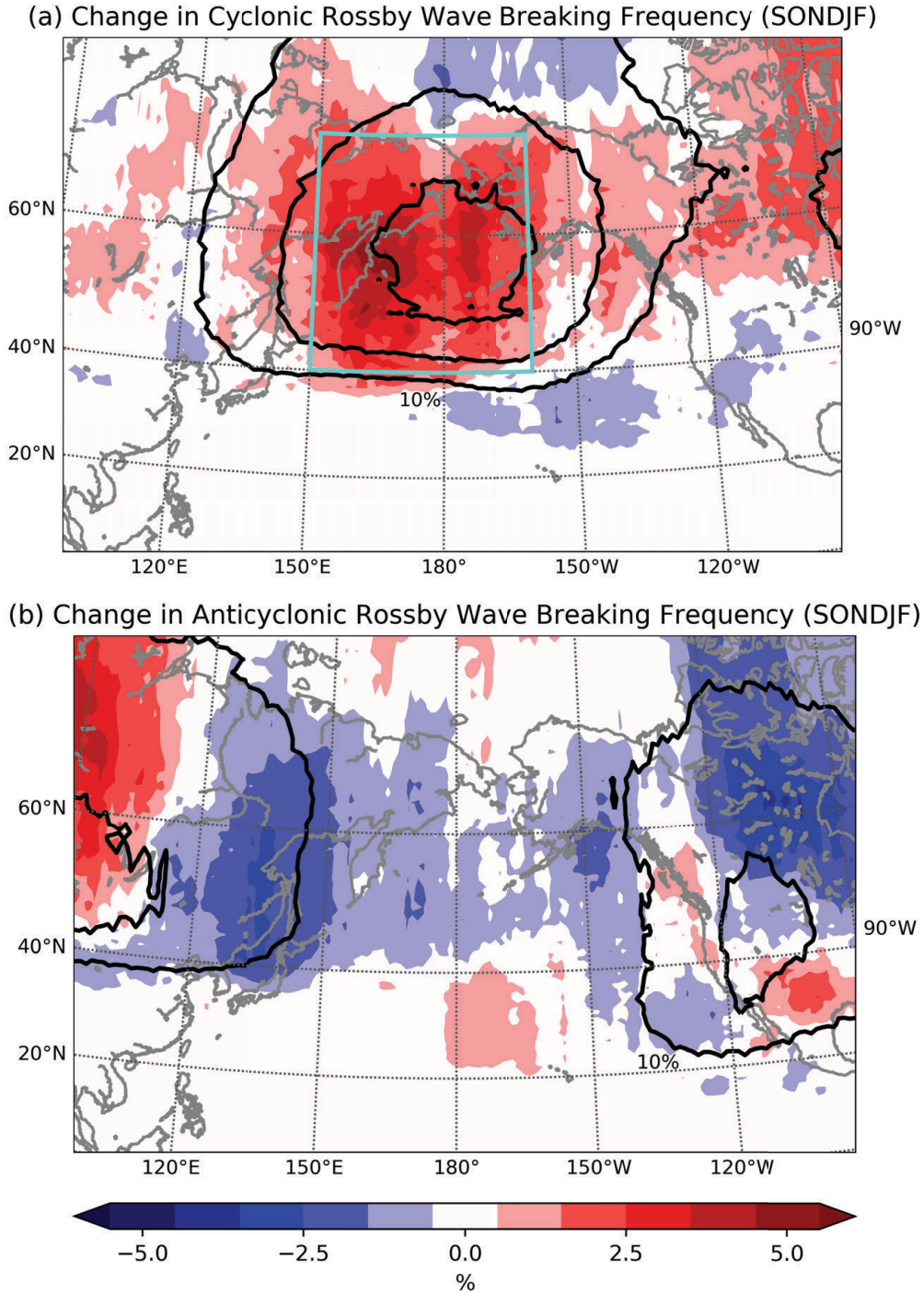


Fig. 5.7. Change (PERT - CTRL) in SONDJF Rossby wave breaking frequency for (a) cyclonic wave breaking and (b) anticyclonic wave breaking events. Only gridpoints where the changes in wave breaking frequency are significant at 95% confidence are shaded. Black contours show the (a) cyclonic and (b) anticyclonic Rossby wave breaking frequency in CTRL, contoured every 5% from 5% to 30%. The blue box in (a) indicates the area encompassing 40-70° N, 150-200° E.

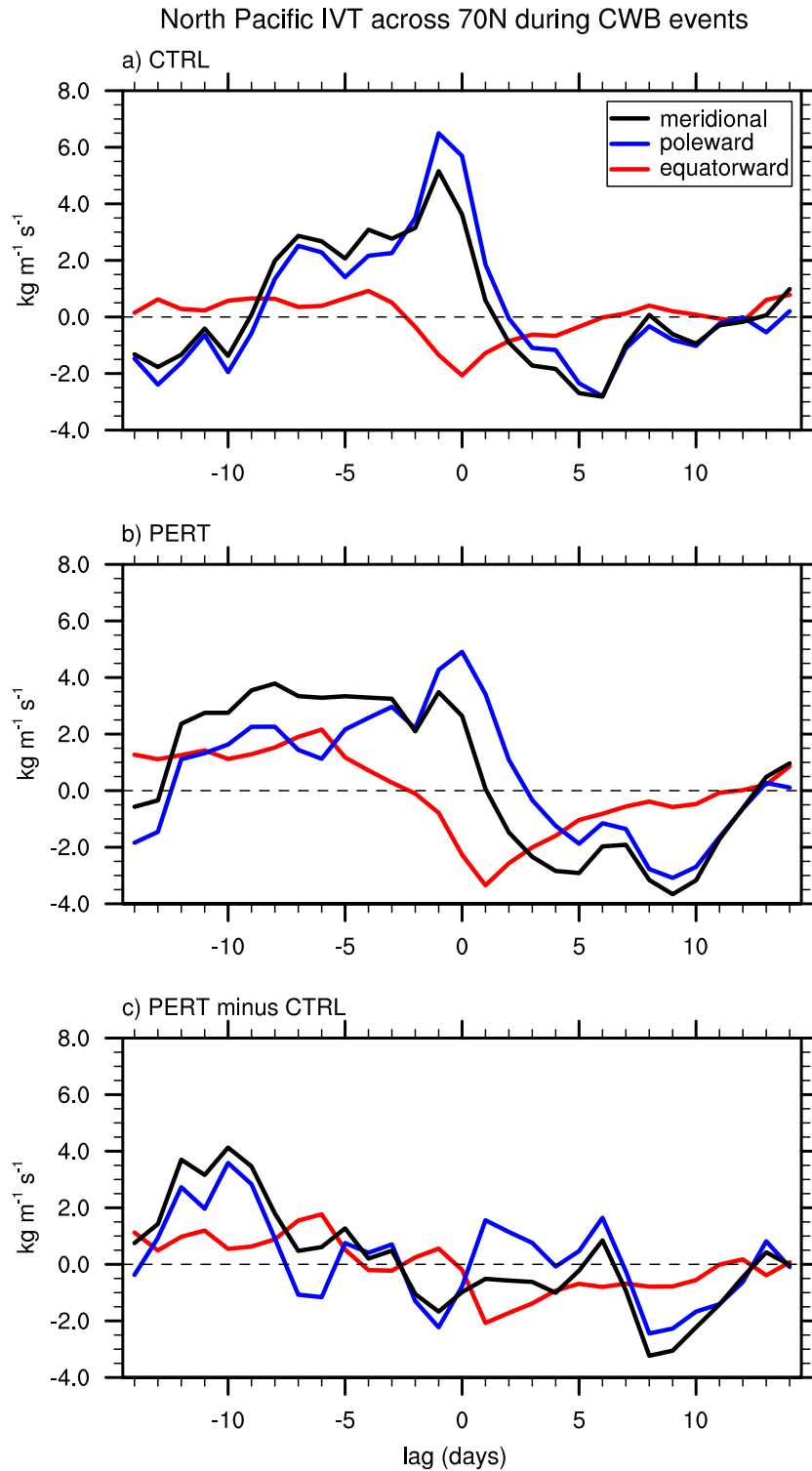


Fig. 5.8. Lagged composites of anomalous moisture transport across 70° N over the North Pacific during cyclonic wave breaking (CWB) events for (a) CTRL, (b) PERT, and (c) PERT - CTRL. See Section 3.3 for a definition of events.

counterintuitive—linking cyclonic Rossby wave breaking with moisture transport *out* of the Arctic. However, Figure 5.8 clearly indicates that cyclonic Rossby wave breaking events are associated with increases in poleward IVT (blue lines in Figures 5.8a-c) shortly before and during the peak of the events, which is in concordance with the results of Liu and Barnes (2015). However, after the peak of the events, there is enhanced equatorward IVT (red lines in Figures 5.8a-c; values of moisture transport that are less than zero indicate an *increase* in equatorward moisture transport), which is especially the case in PERT as compared to CTRL. For example, in CTRL, anomalous equatorward IVT is around $+0.5 \text{ kg}\cdot\text{m}^{-1}\cdot\text{s}^{-1}$ before the event peak (a value greater than 0 indicates anomalously *low* equatorward moisture transport), drops to $-2 \text{ kg}\cdot\text{m}^{-1}\cdot\text{s}^{-1}$ during the event peak, and quickly rebounds, with anomalous equatorward IVT approaching $0 \text{ kg}\cdot\text{m}^{-1}\cdot\text{s}^{-1}$ by lag day +5 (Figure 5.8a). On the other hand, in PERT (Figure 5.8b), anomalous equatorward IVT drops from about $+1 \text{ kg}\cdot\text{m}^{-1}\cdot\text{s}^{-1}$ to $-3.5 \text{ kg}\cdot\text{m}^{-1}\cdot\text{s}^{-1}$, and it remains less than 0 (that is, equatorward IVT is enhanced) up to 10 days after the event peak. We hypothesize that this enhanced equatorward moisture transport in PERT could be related to small but important changes in the circulation. Figure 5.7a shows that the maximum in cyclonic Rossby wave breaking activity shifts slightly westward in PERT relative to CTRL. The changes in cyclonic wind shear (Figure 5.5) and Z500 (Figure 5.6) also support a westward shift. If the maximum in this equatorward moisture transport were to occur over the Bering Strait region with more open ocean, as opposed to land (especially land with complex topography, like that of interior Alaska), this could explain, at least in part, the enhancement of equatorward moisture flux in PERT.

In order to investigate this hypothesis, we create lagged composites of Z500 and $I\vec{V}T$ anomalies over the North Pacific during the cyclonic Rossby wave breaking life cycle. Panels in Figure 5.9 show 3-day running means of Z500 and $I\vec{V}T$ anomalies for cyclonic Rossby wave breaking events, ranging from lag days -7 to +13. In the days preceding cyclonic Rossby wave breaking events, PERT and CTRL show broadly similar patterns, with some small differences. Both CTRL and PERT show high Z500 anomalies over Alaska and the east Pacific and low Z500 anomalies over east Asia and the west Pacific (Figures 5.9a-b), although these anomalies are slightly stronger in PERT. The overall changes (PERT - CTRL) in $I\vec{V}T$ around 70° N are relatively small up to 2

days before the cyclonic wavebreaking event (Figures 5.9c,f). By lag days -4 to -2, both CTRL and PERT show the development of low height anomalies in the central subtropical Pacific, as well as over Japan and the Sea of Okhotsk (Figures 5.9d,e), and a high $Z500$ anomaly over Alaska and the east Pacific.

By the event peak (lag days -1 to +1; Figures 5.9g-i), the low height anomaly over the western Pacific has increased. The center of the low height anomaly is westward in PERT relative to CTRL (Figures 5.9g,h), while the high height anomaly over Alaska is larger in PERT (Figure 5.9i). As expected from Figure 5.8, and from previous work (e.g. Liu and Barnes (2015)), Figures 5.9g,h show $I\vec{V}T$ directed poleward at the event peak in CTRL and in PERT. In both cases, the strongest $I\vec{V}T$ is largely coincident with the strongest gradient in $Z500$.

The differences between CTRL and PERT become more pronounced after the peak of the cyclonic Rossby wave breaking event (lag days +2 to +13, Figures 5.9j-u). At lag days +2 to +4 (Figures 5.9j-l), both CTRL and PERT show a deepening of heights associated with the Aleutian low. The maximum $Z500$ anomaly is actually slightly stronger in CTRL than in PERT, although the anomaly extends farther westward in PERT than in CTRL (Figures 5.9j,k). By lag days +5 to +7, these height anomalies have set up an east-west dipole in $Z500$, with anomalously high heights over eastern Russia and anomalously low heights over Alaska (Figures 5.9m-n). This dipole is stronger in PERT than it is in CTRL, particularly the low height anomaly over Alaska (Figure 5.9o). This east-west dipole in $Z500$ persists into lag days +8 to +10 (Figures 5.9p,q), and the $Z500$ anomalies are particularly strong and persistent in PERT. These more persistent $Z500$ anomalies in PERT create a stronger meridional gradient in $Z500$ that maximizes over eastern Russia and Kamchatka, enhancing equatorward-directed $I\vec{V}T$ across 70° N in this region in PERT relative to CTRL (Figure 5.9r). By lag days +11 to +13, the low $Z500$ anomaly remains in PERT, while it is greatly diminished in CTRL (Figures 5.9s-t). Again, the larger, more persistent low $Z500$ anomaly in PERT is associated with anomalously large equatorward-directed $I\vec{V}T$ in the western Pacific, over eastern Russia and Kamchatka (Figure 5.9u). Therefore, broadly speaking, after the peak of the cyclonic Rossby wave breaking life cycle, PERT shows stronger, more zonally extensive, and more persistent low $Z500$ anomalies over Alaska and the Bering Sea (similar to Figures 5.6) when

Z500 and $IV\vec{T}$ Composited on Cyclonic Rossby Wave Breaking Events

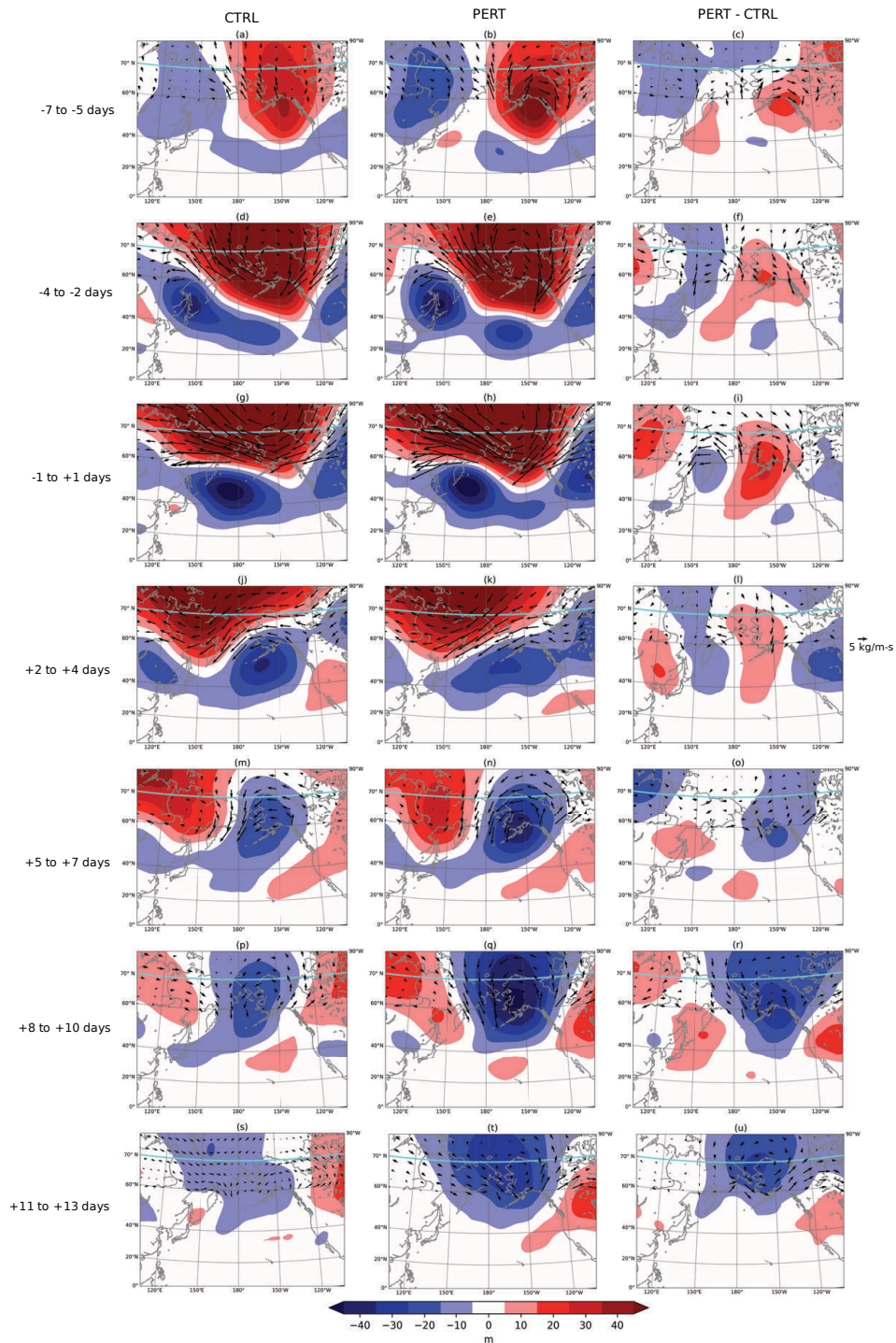


Fig. 5.9. Lagged composites of 500 hPa geopotential height (shading) and $IV\vec{T}$ (arrows; only plotted north of 60° N) anomalies during cyclonic Rossby wave breaking events for (left) CTRL, (center) PERT, and (right) PERT - CTRL. Lag days are averaged in 3 day increments and begin at lag days -7 to -5 (before the event maximum, top row) and continue to lag days +11 to +13 (after the event maximum; bottom row). Only gridpoints with significant changes in 500 hPa geopotential height ($IV\vec{T}$; only one component must be significant) are shaded (plotted). The solid cyan line indicates 70° N.

compared to CTRL (Figures 5.9m-u). This stronger and more persistent low $Z500$ anomaly in PERT facilitates the development of a stronger east-west gradient in $Z500$ that is associated with enhanced equatorward-directed $I\vec{V}T$ over the Bering Strait and eastern Siberia (Figures 5.9m-u). Overall, a life cycle analysis of cyclonic Rossby wave breaking events reinforces the hypothesis that changes in the large-scale circulation associated with sea ice loss act to preferentially enhance equatorward moisture flux, particularly in the Bering Strait region.

5.4 CONCLUSIONS

We use the atmosphere-only general circulation model runs of Sun et al. (2015) to explore the changes in moisture flux across 70° N associated with sea ice loss. When the moisture flux is broken down into poleward and equatorward components, we see an increase in both poleward and equatorward moisture flux across 70° N. The increase in equatorward moisture flux is greater than the increase in poleward moisture flux, particularly in the boreal cold season (SONDJF). A decomposition of the meridional moisture transport reveals that the changes in moisture flux are largely explained by processes occurring on transient time scales and changes in the zonally asymmetric background circulation. Spatially, the largest increases in equatorward moisture fluxes occur in the North Pacific, with over 50% of the increase in global equatorward moisture transport in SONDJF occurring over the North Pacific (120 - 240° E). We conclude that this increase in North Pacific equatorward moisture flux can be explained, at least in part, by an increase in frequency and shift in the location of cyclonic Rossby wave breaking near 55 - 60° N. Large-scale circulation responses in the zonal winds, cyclonic wind shear, and 500 hPa geopotential heights support this conclusion. Rossby wave breaking has been linked to changes in moisture fluxes in the Gulf of Alaska and North American West Coast regions in prior work, suggesting that large-scale atmospheric dynamics can play an important role in moisture transport in the polar and sub-polar regions (e.g. Ryoo et al. (2013), Payne and Magnusdottir (2014), Baggett et al. (2016), Mundhenk et al. (2016)).

We note that these conclusions are drawn based on considering sea ice loss only. In reality, the climate system is more complex and overall changes in midlatitude-Arctic circulation and moisture fluxes are potentially more complicated than what we propose here. For example, greenhouse gas

forcings are often associated with circulation anomalies that oppose those associated with Arctic warming and sea ice loss, and these effects are not necessarily linear (e.g., Butler et al. (2010), McGraw and Barnes (2016), Sun et al. (2015), McKenna et al. (2018)). Recently, however, the circulation responses to greenhouse gas warming and sea ice loss have been shown to be more separable than previously thought (e.g. McCusker et al. (2017)). For example, Figure 5.6 shows a strengthening of the Aleutian low in response to sea ice loss. This strengthening of the Aleutian low has been previously identified in climate model studies as both a response to greenhouse gas warming (e.g. Gan et al. (2017), McCusker et al. (2017)) and to Arctic warming and sea ice loss (e.g. Sun et al. (2015), Blackport and Kushner (2017)). Furthermore, the atmospheric responses to greenhouse gas forcing and sea ice loss may in fact be especially additive in the North Pacific (e.g. Oudar et al. (2017), McCusker et al. (2017)). Thus, the overall response of moisture transport over the North Pacific to sea ice loss may in fact offer insights into the broader response when considering the full impacts of climate change.

Finally, we note that this hypothesis does not argue that all increases in Arctic moisture fluxes are an artifact of circulation changes. Rather, we simply argue that increases in equatorward moisture transport are associated with circulation changes driven by sea ice loss. Figures 7, 8, and 9 illustrate the importance of the changes in the synoptic-scale, transient circulation by showing that the increase in cyclonic Rossby wave breaking events associated with sea ice loss is accompanied by an increase in equatorward IVT following the peak of the events. Thus, changes in the circulation are important for future Arctic moisture transport and must be considered.

Many thanks to Lantao Sun of the NOAA/Earth System Research Laboratory in Boulder, CO, for providing us with the model simulations, and to Elizabeth Barnes for support and feedback. The model data used in this paper are available from the corresponding author upon request. This research was supported by the Climate and Large-Scale Dynamics Program of the National Science Foundation under grant AGS-1419818. Analysis was performed in Python V2.7.8, MATLAB Release 2016b, and the National Center for Atmospheric Research Command Language (NCL) version V6.4.0.

5.5 ADDITIONAL FIGURES

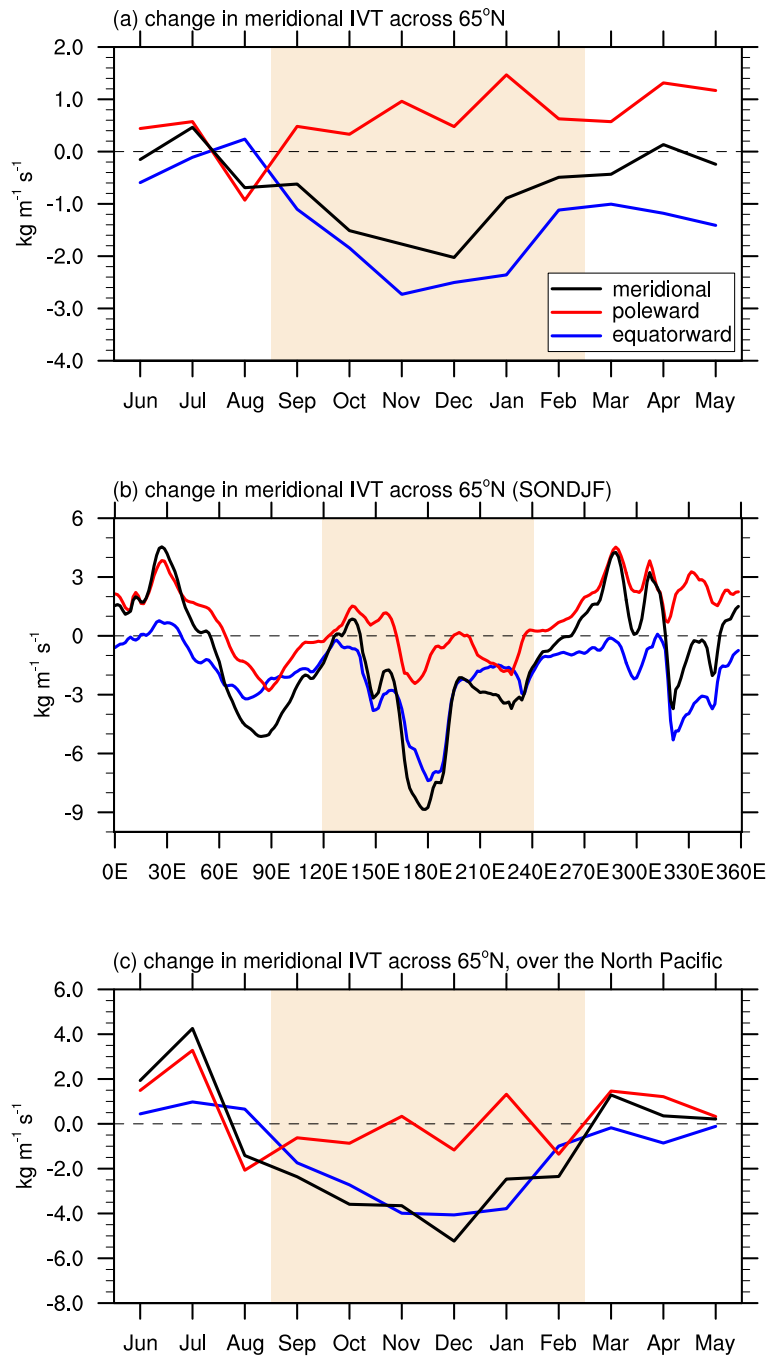


Fig. 5.10. As in Figure 2, but for meridional IVT across 65° N. Change (PERT - CTRL) in meridional IVT associated with sea ice loss as a function of (a) month, (b) longitude during SONDJF (highlighted in (a)), and (c) month over the North Pacific region (120-240° E, highlighted in (b)). Red lines indicate poleward (northward) IVT, blue lines indicate equatorward (southward) IVT, and black lines are the meridional IVT (poleward IVT + equatorward IVT).

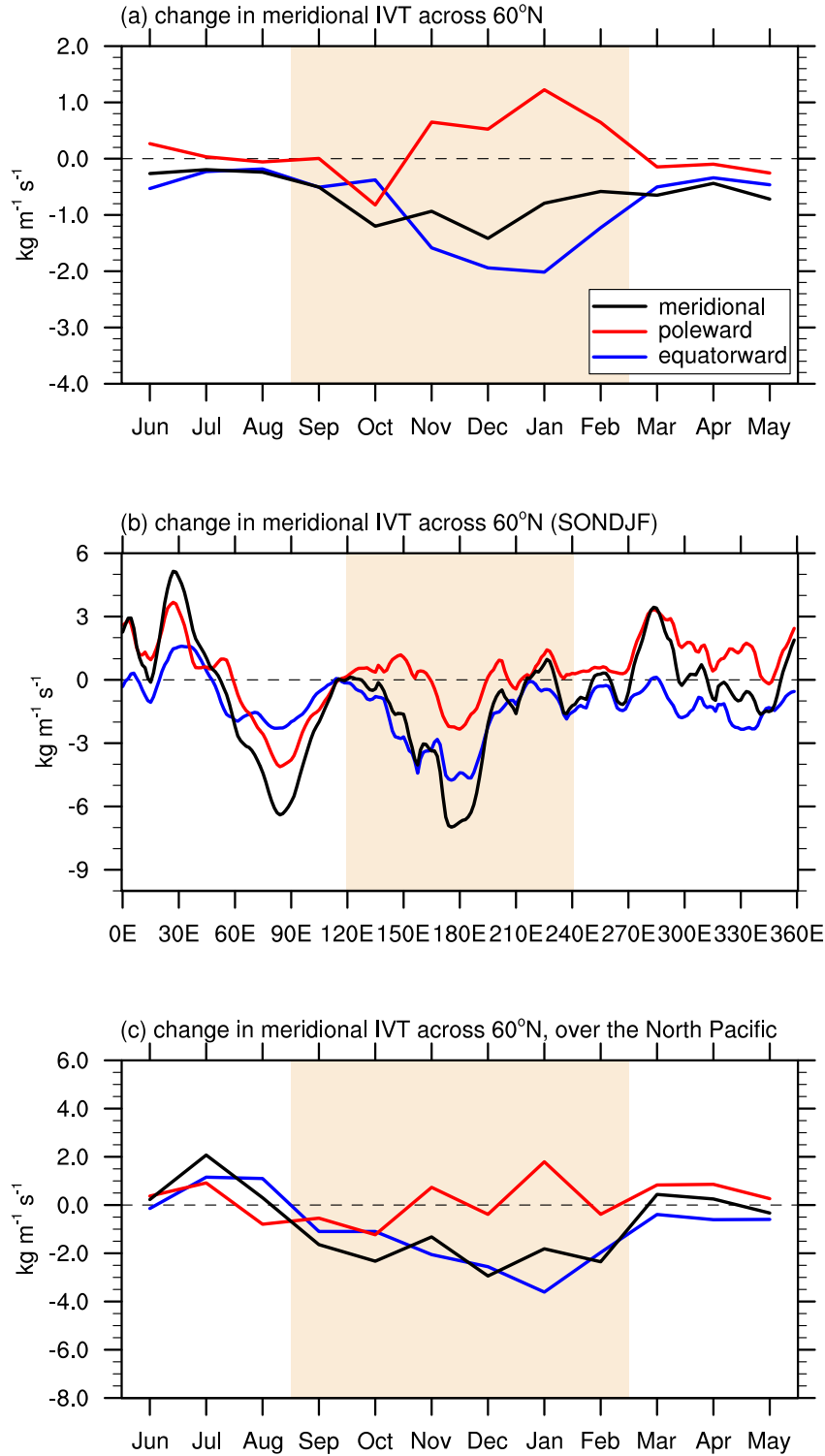


Fig. 5.11. As in Figure 2, but for meridional IVT across 60° N. Change (PERT - CTRL) in meridional IVT associated with sea ice loss as a function of (a) month, (b) longitude during SONDJF (highlighted in (a)), and (c) month over the North Pacific region (120-240° E, highlighted in (b)). Red lines indicate poleward (northward) IVT, blue lines indicate equatorward (southward) IVT, and black lines are the meridional IVT (poleward IVT + equatorward IVT).

6 Conclusions

The work contained within this dissertation explores the connections between Arctic variability and the variability of the midlatitude circulation. This research highlights new relationships between the Arctic and the midlatitude circulation, mostly on sub-monthly timescales. This research also strives to explore and understand these connections in the context of two-way feedbacks, and to present such analysis and the techniques behind it in an accessible, approachable way to the climate science community. This emphasis on both pathways of influence provides a contrast to typical targeted modeling studies, which by design focus only on one direction of influence. This two-way feedback perspective enlightens and guides the major findings of this research.

6.1 THE ROLE OF MIDLATITUDE VARIABILITY IN DRIVING AN ARCTIC RESPONSE

Framing the connections between Arctic and midlatitude variability in the context of two-way feedbacks particularly highlights the importance of the midlatitude circulation variability in driving variability in the Arctic. Many targeted modeling studies constrain the Arctic to a particular state, limiting the ability of the midlatitude circulation to impact the Arctic. However, this pathway of influence is clearly important, and should not be neglected. Variability in both the North Atlantic and North Pacific jet streams drives Arctic variability, which then drives further variability in the jet streams. On sub-monthly timescales, the circulation variability in many midlatitude regions—including North America, Siberia, and the east Pacific and Alaska—drives a response in the Arctic. There is great regional diversity in these relationships, highlighting the importance of a spatially heterogeneous approach in analyzing Arctic-midlatitude connections. Sea ice loss drives changes in the midlatitude circulation, which affect moisture fluxes into and out of the Arctic. Changes in the circulation are associated with a preferential increase in moisture fluxes *out* of the Arctic, which has potential implications for Arctic climate. To paint a comprehensive picture of Arctic-midlatitude connections, influence of the midlatitude circulation on the Arctic must be considered

alongside the more heavily-studied pathway of the Arctic influencing the midlatitudes.

This research has focused on a perspective of two-way feedbacks between the Arctic and the midlatitudes. However, these relationships between the Arctic and the midlatitude circulation can be re-framed in the context of predictability, using many of the same tools. For example, Kretschmer et al. (2017) use many of the same methods described in Chapter 3 to identify predictors of the stratospheric polar vortex state, with a goal of ultimately improving predictability of tropospheric circulation and winter weather. In a similar manner, some of the methods described in this chapter could be used to explore predictability. Possible avenues for future research focused on predictability include:

- (1) Arctic variability has been shown to drive a response in the circulation in the subtropical Pacific (e.g., Figure 5.6a,b). The circulation in the subtropical Pacific influences weather in many regions, including atmospheric rivers hitting the west coast of the US. Does Arctic variability improve the predicability of weather patterns in the subtropical Pacific?
- (2) High Z_{500} anomalies over Eurasia drive Arctic variability at lags of 25 days. Could this be a source of predictability for the Arctic? And since the Arctic drives midlatitude circulation variability on shorter timescales, could we use circulation variability over Eurasia to predict circulation variability in other regions via the Arctic?

Finally, it is worth noting that most of the work within this dissertation is focused on sub-monthly variability. This work does not explore how these relationships between the Arctic and the midlatitude circulation could be impacted by climate change. Relatedly, the processes studied within this dissertation have been assumed to be stationary, at least on timescales relevant to the dynamics of interest. Granger causality-based approaches to non-stationary processes have been developed and applied to climate science (e.g., Attanasio et al. (2013)); however, they have not been adopted here. It is possible that climate change could affect the strength and pattern of these Arctic-midlatitude connections. We have also not addressed the influence of low-frequency variability on these connections, beyond some very preliminary investigations. As low frequency variability has been shown to influence the state of the Arctic (e.g., Screen and Francis (2016)), it is plausible that the

Arctic-midlatitude relationships characterized here could also vary based on low-frequency variability, and preliminary results based on a VAR analysis of climate model output suggest that there is likely a low-frequency component to these Arctic-midlatitude relationships.

6.2 THE PERSISTENCE OF MEMORY

In much of this dissertation, Arctic-midlatitude connections are assessed in the framework of Granger causality. That is, these relationships are considered in the context of added predictive power—how much does including this second predictor improve my predictive skill *beyond* that of autocorrelation, or memory? Many geophysical variables exhibit substantial autocorrelation, so by limiting the influence of autocorrelation, we can focus on, for example, the additional variance in the midlatitude circulation that can be explained by Arctic variability. Working within the Granger causality framework, we can make stronger statements about causal relationships as compared to standard lagged linear regression analysis. As an example, many recent studies have linked Arctic warming and sea ice loss with a strengthening of the Siberian high, and associated cold temperature anomalies (e.g., Honda et al. (2009), Mori et al. (2014), Overland et al. (2015)). Many of these studies implicitly assume that it is the Arctic that is driving a response over Siberia, and they draw these conclusions from regression or composite analysis that does not explicitly account for autocorrelation. However, this research, which does account for the effects of memory and autocorrelation, suggests that circulation anomalies over Siberia drive a response in the Arctic far more than the other way around. These results are in agreement with several modeling studies that have implied that Arctic warming and sea ice loss do not drive significant responses in Eurasian circulation (e.g., McCusker et al. (2016), Sun et al. (2016), Ogawa et al. (2018)), and with the links between extreme temperature events in the Arctic and Siberian circulation (e.g., Messori et al. (2018)).

Furthermore, an analysis framework that accounts for autocorrelation of the climate system can better contextualize the importance of such relationships. In fact, much of this analysis suggests that these relationships between the Arctic and the midlatitudes are relatively small when compared to autocorrelation. Barnes and Simpson (2017) find that Arctic variability only explains 1-3% of

additional variability in the midlatitude jet streams; the work in this dissertation is consistent with these conclusions. Midlatitude circulation variability explaining less than 5% of additional variability in the Arctic in all regions on sub-monthly timescales; and Arctic variability explains even less of the additional variability in the circulation. So, while the influence of the midlatitude circulation in the Arctic is of equal magnitude to that of the Arctic on the midlatitude circulation, neither of these relationships is particularly strong when compared to the role of autocorrelation, and of other drivers.

The approaches described in this dissertation do not account for hidden common causes. That is, they do not explicitly address the possibility that the variables of interest are not directly related to each other, but rather, are both being caused by some unaccounted for third party. This is a fundamental issue of many causality-based analyses, although current work is focused on improving the ability of causal discovery algorithms to detect such hidden common causes (Samarasinghe et al. (2018a)). Ultimately, effective and responsible deployment of causal discovery analyses requires a good physical understanding of the underlying physics so that critical choices about variable selection, model setup, and data preprocessing can be made in an informed manner. We have made these decisions regarding variable selection, timescales of interest, preprocessing, and so on to the best of our abilities, but the possibility of a hidden common cause remains.

Finally, we note that the methods described here are intended to be applied to linear problems. However, there are many areas of atmospheric dynamics that involve non-linear processes. The results of Chapter 5 are an excellent example of this. The changes in Arctic moisture transport in Chapter 5 are attributed to changes in Rossby wave breaking, a highly non-linear phenomenon. Exploratory work was done using a LASSO model to try to predict Arctic moisture transport using Rossby wave breaking and several other related variables. Ultimately, the LASSO model, fundamentally based on linear regression, was not as effective a tool for understanding these relationships as the more standard climate science approaches used in Chapter 5. There are causality-based approaches that are able to characterize non-linear relationships (see the end of Chapter 3 for more on this); however, they were not employed here.

6.3 A DIFFERENCE OF PERSPECTIVE

Ultimately, this research seeks to offer a different perspective on analyzing climate dynamics. Much of the research undertaken to understand these large-scale relationships between different parts of the atmosphere and the climate system utilize targeted modeling studies. While these studies offer great physical insights, and provide substantial opportunities to explore and test physical mechanisms, they are often limited to exploring only one pathway of influence. In reality, these relationships do go in both directions, and a comprehensive understanding of such large-scale interactions between different parts of the atmosphere must ultimately consider the two-way relationships. This research has focused on the relationships between the Arctic and the midlatitude circulation on sub-seasonal timescales; however, the general framework and ideas espoused within have the potential for broader application to many aspects of the climate system on a variety of timescales. We have consistently endeavored to present this work in a manner which emphasizes the more widespread appeal and utility of this approach. In conjunction with this goal, this research also aims to describe the causal discovery methods used here in a comprehensive and approachable manner, with interpretation and examples that are relevant and accessible to climate scientists. Beyond writing papers with thorough and understandable methods section, many of the analytical tools used in this research will be made publicly available as part of the DATAS gateway project, with the goal of writing code that will be widely adoptable by the scientific community.

The two-way feedback perspective, and the causality-based tools applied within it, provide useful and unique perspectives on climate variability. However, it must be stressed that these approaches are *not* intended to replace tools like climate modeling studies. Rather, these tools should be considered alongside such modeling studies. Going forward, a potentially interesting and useful application of the framework developed here involves the use of the two-way feedback perspective and causal discovery tools to develop and refine physical hypotheses. Recent work has focused on identifying key tropospheric predictors of stratospheric variability (e.g., Kretschmer et al. (2017)), and on stratospheric predictors of tropospheric extreme temperature events (e.g., Kretschmer et al.

(2018)), within a causal discovery framework. Causal discovery analysis from a two-way feedback perspective could help identify key relationships between physical variables, and the relevant timescales on which these relationships occur. This identification could help scientists develop more specific, robust physical hypotheses about the dynamics and physics that underly these relationships. The way forward for such studies focused on atmospheric and climate variability includes a place for causality analysis and the inclusion of two-way feedbacks to refine, hone, and complement targeted modeling studies.

REFERENCES

- Arnold, A., Y. Liu, and N. Abe, 2007: Temporal causal modeling with graphical Granger methods. *Proc. 13th ACM SIGKDD Int. Conf. on Knowledge Discovery and Data Mining (SIGKDD '07)*, San Jose, CA, ICKDD, 10pp.
- Arrhenius, S., 1896: On the influence of carbonic acid in the air upon the temperature of the ground. *Phil. Mag. S.*, **41**, 237–276.
- Attanasio, A., A. Pasini, and U. Triacca, 2012: A contribution of attribution of recent global warming by out-of-sample Granger causality analysis. *Atmospheric Science Letters*, **13**, 67–72, doi: 10.1002/asl/365.
- Attanasio, A., A. Pasini, and U. Triacca, 2013: Granger causality analyses for climatic attribution. *Atmospheric and Climate Sciences*, **3**, 515–522, doi: 10.4236/acs.2013.34054.
- Ayarzagüena, B. and J. Screen, 2016: Future Arctic sea ice loss reduces severity of cold air outbreaks in midlatitudes. *Geophysical Research Letters*, **43**, 2801–2809.
- Baggett, C. and S. Lee, 2017: An identification of the mechanisms that lead to Arctic warming during planetary-scale and synoptic-scale wave life cycles. *Journal of the Atmospheric Sciences*, **74** (6), 1859–1877.
- Baggett, C., S. Lee, and S. Feldstein, 2016: An investigation of the presence of atmospheric rivers over the North Pacific during planetary-scale wave life cycles and their role in Arctic warming. *Journal of the Atmospheric Sciences*, **73** (11), 4329–4347.
- Baggett, C. F. and S. Lee, 2015: Arctic warming induced by tropically forced tapping of available potential energy and the role of the planetary-scale waves. *J. Atmos. Sci.*, **72**, 1562–1568, doi: 10.1175/JAS-D-14-0334.1.
- Barnes, E. A., 2013: Revisiting the evidence linking Arctic amplification to extreme weather in midlatitudes. *Geophys. Res. Lett.*, **40**, doi: 10.1002/grl.50880.
- Barnes, E. A. and D. L. Hartmann, 2012: Detection of Rossby wave breaking and its response to shifts of the midlatitude jet with climate change. *J. Geophys. Res.: Atmos.*, **117**, doi:

10.1029/2012JD017469.

Barnes, E. A. and J. A. Screen, 2015: The impact of Arctic warming on the midlatitude jet-stream: Can it? Has it? Will it? *WIREs Clim. Change*, **6**, 277–286, doi: 10.1002/wcc.337.

Barnes, E. A. and I. R. Simpson, 2017: Seasonal sensitivity of the Northern Hemisphere jet streams to Arctic temperatures on subseasonal time scales. *Journal of Climate*, **30**, 10 117–10 137.

Barnett, L. and A. Seth., 2014: The MVGC multivariate Granger causality toolbox: A new approach to Granger-causal inference. *Journal of Neuroscience Methods*, **223**, 50–68.

Blackport, R. and P. Kushner, 2016: The transient and equilibrium climate response to rapid summertime sea ice loss in CCSM4. *Journal of Climate*, **29**, 401–417.

Blackport, R. and P. J. Kushner, 2017: Isolating the atmospheric circulation response to Arctic sea ice loss in the coupled climate system. *J. Climate*, **30**, 2163–2185.

Blanchard-Wrigglesworth, E., C. M. Bitz, and M. M. Holland, 2011: Influence of initial conditions and climate forcing on predicting Arctic sea ice. *Geophys. Res. Lett.*, **38**, L18 503, doi: 10.1029/2011GL048807.

Burt, M. A., D. A. Randall, and M. D. Branson, 2016: Dark warming. *Journal of Climate*, **29** (2), 705–719.

Butler, A. H., D. W. J. Thompson, and R. Heikes, 2010: The steady-state atmospheric circulation response to climate change-like thermal forcings in a simple general circulation model. *J. Climate*, **23**, 3474–3496, doi: 10.1175/2010JCLI3228.1.

Cattiaux, J., Y. Peings, D. Saint-Martin, N. Trou-Kechout, and S. J. Vavrus, 2016: Sinuosity of mid-latitude atmospheric flow in a warming world. *Geophys. Res. Lett.*, doi: 10.1002/2016GL070309.

Chu, T., D. Danks, and C. Glymour, 2005: Data driven methods for nonlinear granger causality: Climate teleconnection mechanisms. Tech. rep., Carnegie Mellon University, Department of Philosophy.

- Cohen, J., et al., 2014: Recent Arctic amplification and extreme midlatitude weather. *Nature Geoscience*, **7**, 627–637, doi: 10.1038/ngeo2234.
- Cohen, J. L., J. C. Furtado, M. A. Barlow, V. A. Alexeev, and J. E. Cherry, 2012: Arctic warming, increasing snow cover and widespread boreal winter cooling. *Environ. Res. Lett.*, **7**, 014007, doi: 10.1088/1748-9326/7/1/014007.
- Collins, M., et al., 2013: Long-term Climate Change: Projections, Commitments and Irreversibility. In: *Climate Change 2013: The Physical Science Basis. Contribution of Working Group I to the Fifth Assessment Report of the Intergovernmental Panel on Climate Change*. Cambridge University Press.
- Colombo, D. and M. H. Maathuis, 2014: Order-independent constraint-based causal structure learning. *The Journal of Machine Learning Research*, **15** (1), 3741–3782.
- Compo, G., et al., 2011: The Twentieth Century Reanalysis Project. *Quart. J. Roy. Meteorol. Soc.*, **137**, 1–28, doi: 10.1002/qj.776.
- Davidson, J., D. Stephenson, and A. Turasie, 2016: Time series modeling of paleoclimate data. *Environmetrics*, **27**, 55–65.
- Deser, C., L. Sun, R. A. Tomas, and J. Screen, 2015: Does ocean coupling matter for the northern extratropical response to projected Arctic sea ice loss? *Geophys. Res. Lett.*, **43**, 2149–2157, doi: 10.1002/2016GL067792.
- Deser, C., L. Terray, and A. S. Phillips, 2016: Forced and internal components of winter air temperature trends over North America during the past 50 years: Mechanisms and implications. *J. Climate*, **29**, 2237–2258, doi: 10.1175/JCLI-D-15-0304.1.
- Deser, C., R. A. Tomas, M. Alexander, and D. Lawrence, 2010: The seasonal atmospheric response to projected Arctic sea ice loss in the late twenty-first century. *J. Clim.*, **23**, 333–351, doi: 10.1175/2009JCLI3053.1.
- Ebert-Uphoff, I. and Y. Deng, 2012: Causal discovery for climate research using graphical models. *J. Climate*, **25**, 5648–5665.
- Elsner, J., 2006: Evidence in support of the climate change–Atlantic hurricane hypothesis. *Geophys. Res. Lett.*, **33**, L16705, doi: 10.1029/2006GL026869.

- Elsner, J., 2007: Granger causality and Atlantic hurricanes. *Tellus A*, **59**, 476–485, doi: 10.1111/j.1600-0870.2007.00244.x.
- Feldstein, S. B. and S. Lee, 2014: Intraseasonal and interdecadal jet shifts in the Northern Hemisphere: The role of warm pool tropical convection and sea ice. *Journal of Climate*, **27** (17), 6497–6518.
- Francis, J. A. and E. Hunter, 2006: New insight into the disappearing Arctic sea ice. *Eos, Transactions American Geophysical Union*, **87**, 509–511, doi: 10.1029/2006EO460001.
- Francis, J. A. and S. J. Vavrus, 2012: Evidence linking Arctic amplification to extreme weather in mid-latitudes. *Geophys. Res. Lett.*, **39**, doi: 10.1029/2012GL05100.
- Francis, J. A. and S. J. Vavrus, 2015: Evidence for a wavier jet stream in response to rapid Arctic warming. *Environ. Res. Lett.*, **10**, doi: 10.1088/1748-8326/10/1/014005.
- Franzke, C., T. Woollings, and O. Martius, 2011: Persistent circulation regimes and preferred regime transitions in the North Atlantic. *J. Atmos. Sci.*, **68**, 2809–2825.
- Franzke, C. L. E., S. Lee, and S. B. Feldstein, 2016: Evaluating Arctic warming mechanisms in CMIP5 models. *Clim. Dyn.*, doi: 10.1107/s00382-016-3263-9.
- Furtado, J., J. Cohen, A. Butler, E. Riddle, and A. Kumar, 2015: Eurasian snow cover variability and links to winter climate in the CMIP5 models. *Climate Dynamics*, **45**, 2591–2605.
- Gan, B., L. Wu, F. Jia, S. Li, W. Cai, H. Nakamura, M. J. Alexander, and A. J. Miller, 2017: On the response of the Aleutian low to greenhouse gas warming. *J. Climate*, **30**, 3907–3925.
- Ghatak, D., C. Deser, A. Frei, G. Gong, A. Phillips, D. A. Robinson, and J. Stroeve, 2012: Simulated Siberian snow cover response to observed Arctic sea ice loss, 1979–2008. *J. Geophys. Res.: Atmos.*, **117**, 2156–2270, doi: 10.1029/2012JD018047.
- Ghatak, D. and J. Miller, 2013: Implications for Arctic amplification of changes in the strength of the water vapor feedback. *Geophys. Res. Lett.*, **118**, 7569–7578, doi: 10.1002/jgrd.50578.

- GMAO, 2015: MERRA-2 inst6_3d_ana_Np: 3d, 6-Hourly, Instantaneous, Pressure-Level, Analysis, Analyzed Meteorological Fields V5.12.4. Greenbelt, MD, USA, Goddard Earth Sciences Data and Information Services Center (GES DISC), Accessed 2017-03-23, doi: 10.5067/A7S6XP56VZWS.
- Goss, M. S., S. B. Feldstein, and S. Lee, 2016: Stationary wave interference and its relation to tropical convection and Arctic warming. *J. Climate*, **29**, 1369–1389, doi: 10.1175/JCLI-D-15-0267.1.
- Granger, C., 1969: Investigating causal relations by econometric models and cross-spectral methods. *Econometrica*, **37**, 424–438, doi: 10.2307/1912791.
- Graversen, R. G., 2006: Do changes in the midlatitude circulation have any impact on the Arctic surface air temperature trend? *J. Climate*, **19**, 5422–5438.
- Graversen, R. G. and M. Burtu, 2016: Arctic amplification enhanced by latent energy transport of atmospheric planetary waves. *Quart. J. Roy. Meteorol. Soc.*, **142**, 2046–2054, doi: 10.1002/qj.2802.
- Gu, G. and R. F. Adler, 2011: Precipitation and temperature variations on the interannual time scale: Assessing the impact of ENSO and volcanic eruptions. *J. Climate*, **24**, 2258–2270, doi: 10.1175/2010JCLI3727.1.
- Handorf, D., R. Jaiser, K. Dethloff, A. Rinke, and J. Cohen, 2015: Impacts of Arctic sea ice and continental snow cover changes on atmospheric winter teleconnections. *Geophysical Research Letters*, **42**, GL063 203.
- Hannart, A., J. Pearl, F. Otto, P. Naveau, and M. Ghil, 2016a: Causal counterfactual theory for the attribution of weather and climate-related events. *Bulletin of the American Meteorological Society*, **97** (1), 99–110.
- Hannart, A., J. Pearl, F. E. L. Otto, P. Naveau, and M. Ghil, 2016b: Causal counterfactual theory for the attribution of weather and climate-related events. *Bull. Amer. Meteor. Soc.*, **97**, 99–110, doi: 10.1175/BAMS-D-14-00034.1.
- Hansen, J., A. Lacis, D. Rind, G. Russell, P. Stone, I. Fung, R. Ruedy, and J. Lerner, 1984: *Climate sensitivity: Analysis of feedback mechanisms*. American Geophysical Union, 130-163 pp., AGU Geophysical Monographs, No. 29, Maurice Ewing Vol. 5.

- Hastie, T., R. Tibshirani, and J. Friedman, 2001: *The Elements of Statistical Learning: Data Mining, Inference, and Prediction*. 2d ed., Springer.
- Hastie, T., R. Tibshirani, and M. Wainwright, 2015: *Statistical Learning with Sparsity: The Lasso and Generalizations*. Chapman and Hall/CRC.
- Held, I. M. and B. J. Soden, 2006: Robust responses of the hydrological cycle to global warming. *J. Climate*, **19**, 5686–5699.
- Hendon, H. H., M. C. Wheeler, and C. Zhang, 2007: Seasonal dependence of the MJO-ENSO relationship. *J. Climate*, **20**, 531–543, doi: 10.1175/JCLI4003.1.
- Holland, M. M. and C. M. Bitz, 2003: Polar amplification of climate change in coupled models. *Clim. Dyn.*, **21**, 221–232, doi: 10.1007/s00382-003-0332-6.
- Honda, M., J. Inoue, and S. Yamane, 2009: Influence of low Arctic sea-ice minima on anomalously cold Eurasian winters. *Geophysical Research Letters*, **36**.
- Hoskins, B. J. and K. I. Hodges, 2002: New perspectives on the Northern Hemisphere winter storm tracks. *J. Atmos. Sci.*, **59**, 1041–1061.
- Inoue, J., M. E. Hori, and K. Takaya, 2012: The role of Barents Sea ice in the wintertime cyclone track and emergence of warm-Arctic cold-Siberian anomaly. *J. Climate*, **25**, 2561–2568, doi: 10.1175/JCLI-D-11-00449.1.
- Ivanov, V. and L. Kilian, 2005: A practitioner’s guide to lag order selection for VAR impulse response analysis. *Studies in Nonlinear Dynamics & Econometrics*, **9** (1), doi: 10.2202/1558-3708.1219.
- Jahn, A., J. E. Kay, M. M. Holland, and D. M. Hall, 2016: How predictable is the timing of a summer ice-free Arctic? *Geophysical Research Letters*, **43**, 9113–9120.
- Johansen, S. and K. Juselius, 1990: Maximum likelihood estimation and inference on cointegration—With applications to the demand for money. *Oxford Bulletin of Economics and Statistics*, **52**, 169–210, doi: 10.1111/j.1468-0084.1990.mp52002003.x.
- Kapsch, M.-L., R. G. Graversen, M. Tjernstroöm, and R. Bintanja, 2016: The effect of downwelling longwave and shortwave radiation on Arctic summer sea ice. *J. Climate*, **29**, 1143–1158,

doi: 10.1175/JCLI-D-15-0238.1.

- Kaufman, R., L. Zhou, R. Myneni, C. Tucker, D. Slayback, N. Shabanov, and J. Pinzon, 2003: The effect of vegetation on surface temperature: A statistical analysis of NDVI and climate data. *Geophys. Res. Lett.*, **30**, 2147, doi: 10.1029/2003GL018251.
- Kaufmann, R. K. and D. I. Stern, 2002: Cointegration analysis of hemispheric temperature relations. *Journal of Geophysical Research: Atmospheres*, **107**, 2156–2202, doi: 10.1029/2000JD000174.
- Kay, J., et al., 2015: The Community Earth System Model (CESM) Large Ensemble Project: A Community Resource for Studying Climate Change in the Presence of Internal Climate Variability. *Bull. Amer. Meteor. Soc.*, **96**, 1333–1349, doi: 10.1175/BAMS-D-13-00255.1.
- Kelleher, M. and J. Screen, 2018: Atmospheric precursors of and response to anomalous Arctic sea ice in CMIP5 models. *Advances in Atmospheric Sciences*, **35**, 27–37.
- Kim, B.-M., S.-W. Son, S.-K. Min, J.-H. Jeong, S.-J. Kim, X. Zhang, T. Shim, and J.-H. Yoon, 2014: Weakening of the stratospheric polar vortex by Arctic sea-ice loss. *Nature communications*, **5**, 4646.
- Klein, S. A., B. J. Soden, and N.-C. Lau, 1999: Remote sea surface temperature variations during ENSO: Evidence for a tropical atmospheric bridge. *J. Climate*, **12**, 917–932, doi: 10.1175/1520-0442(1999)012<0917:RSSTVD>2.0.CO;2.
- Koenigk, T., M. Caian, G. Nikulin, and S. Schimanke, 2016: Regional Arctic sea ice variations as a predictor for winter climate conditions. *Climate Dynamics*, **46**, 317–337.
- Kretschmer, M., D. Coumou, L. Agel, M. Barlow, E. Tziperman, and J. Cohen, 2018: More-persistent weak stratospheric polar vortex states linked to cold extremes. *Bulletin of the American Meteorological Society*, **99**, 49–60.
- Kretschmer, M., D. Coumou, J. F. Donges, and J. Runge, 2016: Using causal effect networks to analyze different Arctic drivers of midlatitude winter circulation. *Journal of Climate*, **29**, 4069–4081.
- Kretschmer, M., J. Runge, and D. Coumou, 2017: Early prediction of extreme stratospheric polar vortex states based on causal precursors. *Geophysical Research Letters*, **44**, GL074696.

- Kug, J.-S., J.-H. Jeong, Y.-S. Jang, B.-M. Kim, C. Folland, S.-K. Min, and S.-W. Son, 2015: Two distinct influences of Arctic warming on cold winters of North America and East Asia. *Nature Geoscience*, **8**, doi: 10.1038/NGEO2517.
- Kug, J.-S., J.-H. Jeong, Y.-S. Jang, B.-M. Kim, C. K. Folland, S.-K. Min, and S.-W. Son, 2017: Two distinct influences of Arctic warming on cold winters over North America and East Asia. *Nat. Geosci.*, **8**, 759–762, doi: 10.1038/ngeo2517.
- Langen, P. L. and V. A. Alexeev, 2007: Polar amplification as a preferred response in an idealized aquaplanet GCM. *Clim. Dyn.*, doi: 10.1007/s00382-006-0221-x.
- Lee, M.-Y., C.-C. Hong, and H.-H. Hsu, 2015: Compounding effects of warm sea surface temperature and reduced sea ice on the extreme circulation over the extratropical North Pacific and North America during the 2013–2014 boreal winter. *Geophys. Res. Lett.*, **42**, 2014GL062956.
- Lee, S., 2014: A theory for polar amplification from a general circulation perspective. *Asia-Pac. J. Atmos. Sci.*, **50**, 31–43.
- Liu, C. and E. A. Barnes, 2015: Extreme moisture transport into the Arctic linked to Rossby wave breaking. *J. Geophys. Res. Atmos.*, **120**, 3774–3788, doi: 10.1002/2014JD022796.
- Liu, C., X. Ren, and X. Yang, 2014: Mean flow-storm track relationship and Rossby wave breaking in two types of El-Niño. *Advances in Atmospheric Sciences*, **31** (1), 197.
- Liu, J., J. A. Curry, H. Wang, M. Song, and R. M. Horton, 2012: Impact of declining Arctic sea ice on winter snowfall. *Proc. Natl. Acad. Sci. (USA)*, **109**, 4074–4079, doi: 10.1073/pnas.1114910109.
- Lund, R., H. Hurd, P. Bloomfield, and R. Smith, 1995: Climatological time series with periodic correlation. *Journal of Climate*, **8**, 2787–2809.
- Luo, B., D. Luo, L. Wu, L. Zhong, and I. Simmonds, 2017: Atmospheric circulation patterns which promote winter Arctic sea ice decline. *Environmental Research Letters*, **12** (5).
- Luo, D., Y. Xiao, Y. Yao, A. Dai, I. Simmonds, and C. Franzke, 2016: Impact of Ural blocking on winter warm Arctic–cold Eurasian anomalies. Part I: Blocking-induced amplification. *Journal of Climate*, **29**, 3925–3947.

- Lütkepohl, H., 2007: *New Introduction to Multiple Time Series Analysis*. Corr. 2nd printing ed., Springer.
- Manabe, S. and R. J. Stouffer, 1980: Sensitivity of a global climate model to an increase of CO₂ concentration in the atmosphere. *J. Geophys. Res.*, **85**, 5529–5554.
- Manabe, S. and R. T. Wetherald, 1975: The effects of doubling the CO₂ concentration on the climate of a general circulation model. *Journal of the Atmospheric Sciences*, **32** (1), 3–15.
- Matthewman, N. J. and G. Magnúsdóttir, 2011: Observed interaction between Pacific sea ice and the Western Pacific Pattern on intraseasonal time scales. *J. Climate*, **24**, 5031–5042, doi: 10.1175/2011-JCLI4216.1.
- McCusker, K., J. Fyfe, and M. Sigmond, 2016: Twenty-five winters of unexpected Eurasian cooling unlikely due to Arctic sea-ice loss. *Nat. Geosci.*, **9**, 838–842, doi: 10.1038/ngeo2820.
- McCusker, K. E., P. J. Kushner, J. C. Fyfe, M. Sigmond, V. V. Kharin, and C. M. Bitz, 2017: Remarkable separability of circulation response to Arctic sea ice loss and greenhouse gas forcing. *Geophys. Res. Lett.*, **L074327**, 7955–7964.
- McGraw, M. C. and E. A. Barnes, 2016: Seasonal sensitivity of the eddy-driven jet to tropospheric heating in an idealized AGCM. *J. Climate*, **29**, 5223–5240, doi: 10.1175/JCLI-D-15-0723.1.
- McGraw, M. C. and E. A. Barnes, 2018: Memory matters: A case for Granger causality in climate variability studies. *Journal of Climate*, **31**, 3289–3300, doi: 10.1175/JCLI-D-17-0334.1.
- McKenna, C. M., T. J. Bracegirdle, E. F. Shuckburgh, P. H. Haynes, and M. M. Joshi, 2018: Arctic sea ice loss in different regions leads to contrasting Northern Hemisphere impacts. *Geophysical Research Letters*, **L076433**.
- Melkumova, L. and S. Shatskikh, 2017: Comparing ridge and lasso estimators for data analysis. *Procedia Engineering*, **201**, 746–755.
- Messori, G., C. Woods, and R. Caballero, 2018: On the drivers of wintertime temperature extremes in the high Arctic. *J. Climate*, **31**, 1597–1618.

- Mohkov, I., D. Smirnov, P. Nakonechny, S. Kozlenko, E. Seleznev, and J. Kurths, 2011: Alternating mutual influence of El Niño/Southern Oscillation and Indian monsoon. *Geophys. Res. Lett.*, **38**, L00F04.
- Mokhov, I. I., D. A. Smirnov, P. I. Nakonechny, S. S. Kozlenko, E. P. Seleznev, and J. Kurths, 2011: Alternating mutual influence of El-Niño/Southern Oscillation and Indian monsoon. *Geophysical Research Letters*, **38**.
- Mori, M., M. Watanabe, H. Shiogama, J. Inoue, and M. Kimoto, 2014: Robust Arctic sea-ice influence on the frequent Eurasian cold winters in past decades. *Nature Geoscience*, **7**, 869.
- Mortin, J., G. Svensson, R. G. Graversen, M.-L. Kapsch, J. C. Stroeve, and L. N. Boisvert, 2016: Melt onset over Arctic sea ice controlled by atmospheric moisture transport. *Geophysical Research Letters*, **43** (12), 6636–6642.
- Mosedale, T., D. Stephenson, M. Collins, and T. Mills, 2006: Granger causality of coupled climate processes: Ocean feedback on the North Atlantic Oscillation. *J. Climate*, **19**, 1182–1194, doi: 10.1175/JCLI3653.1.
- Mundhenk, B. D., E. A. Barnes, E. D. Maloney, and K. M. Nardi, 2016: Modulation of atmospheric rivers near Alaska and the U.S. West Coast by northeast Pacific height anomalies. *Journal of Geophysical Research: Atmospheres*, **121**, 12 751–12 765, doi: 10.1002/2016JD025350.
- Murphy, K., 2014: Bayes net toolbox for Matlab (BNT). Available at <https://github.com/bayesnet/bnt>.
- Newman, M., G. N. Kiladis, K. M. Weickmann, F. M. Ralph, and P. D. Sardeshmukh, 2012: Relative contributions of synoptic and low-frequency eddies to time-mean atmospheric moisture transport, including the role of atmospheric rivers. *J. Climate*, **25**, 7341–7361, doi: 10.1175/JCLI-D-11-00665.1.
- Nicholson, W. B., D. S. Matteson, and J. Bien, 2017: VARX-L: Structured regularization for large vector autoregressions with exogenous variables. *International Journal of Forecasting*, **33** (3), 627–651.
- Ogawa, F., et al., 2018: Evaluating impacts of recent Arctic sea ice loss on the Northern Hemisphere winter climate change. *Geophysical Research Letters*, **45**, 3255–3263.

- Osborne, J., J. Screen, and M. Collins, 2017: Ocean-atmosphere state dependence of the atmospheric response to Arctic sea ice loss. *J. Climate*, **30**, 1537–52.
- Oudar, T., E. Sanchez-Gomez, F. Chauvin, J. Cattiaux, L. Terray, and C. Cassou, 2017: Respective roles of direct GHG radiative forcing and induced Arctic sea ice loss on the Northern Hemisphere atmospheric circulation. *Climate Dynamics*, **49**, 3693–3713.
- Overland, J., J. A. Francis, R. Hall, E. Hanna, S.-J. Kim, and T. Vihma, 2015: The melting Arctic and midlatitude weather patterns: Are they connected? *Journal of Climate*, **28**, 7917–7932.
- Papagiannopoulou, C., D. G. Miralles, S. Decubber, M. Demuzere, N. E. C. Verhoest, W. A. Dorigo, and W. Waegeman, 2017: A non-linear granger-causality framework to investigate climate–vegetation dynamics. *Geoscientific Model Development*, **10** (1), 1945–1960, doi: <https://doi.org/10.5194/gmd-10-1945-2017>.
- Park, D.-S. R., S. Lee, and S. B. Feldstein, 2015a: Attribution of the recent winter sea ice decline over the Atlantic sector of the Arctic Ocean. *J. Climate*, **28**, 4027–4033, doi: 10.1175/JCLI-D-15-0042.1.
- Park, H.-S., S. Lee, S.-W. Son, S. B. Feldstein, and Y. Kosaka, 2015b: The impact of poleward moisture and sensible heat flux on Arctic winter sea ice variability. *J. Climate*, **28**, 5030–5040, doi: 10.1175/JCLI-D-15-0074.1.
- Pasini, A., U. Triacca, and A. Attanasio, 2012: Evidence of recent causal decoupling between solar radiation and global temperature. *Environ. Res. Lett.*, **7**, 034 020, doi: 10.1088/1748-9326/7/3/034020.
- Payne, A. E. and G. Magnusdottir, 2014: Dynamics of landfalling atmospheric rivers in the North Pacific in 30 years of MERRA Reanalysis. *J. Climate*, **27**, 7133–7150, doi: 10.1175/JCLI-D-14-00034.1.
- Pearl, J., 1988: *Probabilistic Reasoning in Intelligent Systems: Networks of Plausible Inference*. 2d ed., Morgan Kaufman Publishers, 552 pp.
- Pearl, J., 2000: *Causality - Models, Reasoning and Inference*. Reprinted with corrections ed., Cambridge University Press.

- Pearl, J., 2009: *Causality*. Cambridge University Press.
- Pedersen, R., I. Cvijanovic, P. Langen, and B. Vinther, 2016: The impact of regional Arctic sea ice loss on atmospheric circulation and the NAO. *Journal of Climate*, **29**, 889–902.
- Peings, Y., E. Brun, V. Mauvais, and H. Douville, 2013: How stationary is the relationship between Siberian snow and Arctic Oscillation over the 20th century? *Geophys. Res. Lett.*, **40**, 183–188, doi: 10.1029/2012GL054083.
- Peings, Y., J. Cattiaux, S. Vavrus, and G. Magnusdottir, 2017: Late twenty-first-century changes in the midlatitude atmospheric circulation in the CESM large ensemble. *J. Climate*, **30**, 5943–5960, doi: 10.1175/JCLI-D-16-0340.1.
- Peings, Y. and G. Magnusdottir, 2014: Response of the wintertime Northern Hemisphere atmospheric circulation to current and projected Arctic sea ice decline: A numerical study with CAM5. *J. Climate*, **27**, 244–264, doi: 10.1175/JCLI-D-13-00272.1.
- Peings, Y. and G. Magnusdottir, 2016: Wintertime atmospheric response to Atlantic multidecadal variability: Effect of stratospheric representation and ocean–atmosphere coupling. *Climate dynamics*, **47**, 1029–1047.
- Peixóto, J. P. and A. H. Oort, 1992: *Physics of Climate*. American Institute of Physics, 520 pp pp.
- Pfaff, B. et al., 2008: VAR, SVAR and SVEC models: implementation within R package vars. *Journal of Statistical Software*, **27** (4), 1–32.
- Polyani, L. M. and D. W. Waugh, 2004: Upward wave activity flux as a precursor to extreme stratospheric events and subsequent anomalous surface weather regimes. *J. Climate*, **17**, 3548–3554, doi: 10.1175/1520-0442(2004)017<3548:UWAFAA>2.0.CO;2.
- Rayner, N., D. Parker, E. Horton, C. Folland, L. Alexander, D. Rowell, E. Kent, and A. Kaplan, 2003: Global analyses of sea surface temperature, sea ice, and night marine air temperature since the late nineteenth century. *J. Geophys. Res.*, **108**, 4407, doi: 10.1029/2002JD002670.
- Rebane, G. and J. Pearl, 1987a: The recovery of causal poly-trees from statistical data. *Proc. Sixth Workshop on Uncertainty in AI*, Seattle, WA, AAAI, 222–228.

- Rebane, G. and J. Pearl, 1987b: The recovery of causal poly-trees from statistical data. en “uai’87: Proceedings of the third annual conference on uncertainty in artificial intelligence”, págs. 175–182. Elsevier.
- Ronalds, B., E. Barnes, and P. Hassanzadeh, 2018: A barotropic mechanism for the response of jet stream variability to Arctic amplification and sea ice loss. *J. Climate*, **31**, 7069–7085, doi: 10.1175/JCLI-D-17-0778.1.
- Ropelewski, C. and M. Halpert, 1986: North American precipitation and temperature patterns associated with the El Niño/Southern Oscillation (ENSO). *Mon. Wea. Rev.*, **114**, 2352–2362, doi: 10.1175/1520-0493(1986)114<2352:NAPATP>2.0.CO;2.
- Runge, J., V. Petoukhov, and J. Kurths, 2014: Quantifying the strength and delay of climatic interactions: The ambiguities of cross correlation and a novel measure based on graphical models. *J. Climate*, **27**, 720–739, doi: 10.1175/JCLI-D-13-00159.1.
- Ryoo, J.-M., Y. Kaspi, D. W. Waugh, G. N. Kiladis, D. E. Waliser, E. J. Fetzer, and J. Kim, 2013: Impact of Rossby wave breaking on U.S. West Coast winter precipitation during ENSO events. *J. Climate*, **26**, 6360–6382, doi: 10.1175/JCLI-D-12-00297.1.
- Samarasinghe, S., E. Barnes, and I. Ebert-Uphoff, 2018a: Causal discovery in the presence of latent variables for climate science. *Proceedings of the 8th International Workshop on Climate Informatics*, NCAR Technical Note NCAR/TN-550+PROC, doi: 10.5065/D6BZ64XQ.
- Samarasinghe, S., M. McGraw, E. Barnes, and I. Ebert-Uphoff, 2018b: A study of links between the Arctic and the midlatitude jet-stream using Granger and Pearl causality. *Environmetrics*, doi: 10.1002/env.2540.
- Screen, J., 2014: Arctic amplification decreases temperature variance in northern mid-to high-latitudes. *Nat. Climate Change*, **4**, 577–582, doi: 10.1038/nclimate2268.
- Screen, J., 2017: Simulated atmospheric response to regional and pan-Arctic sea ice loss. *J. Climate*, **30**, 3945–62.
- Screen, J. A., C. Deser, and I. Simmonds, 2012: Local and remote controls on observed Arctic warming. *Geophys. Res. Lett.*, **39**, L10 709, doi: 10.1029/2012GL051598.

- Screen, J. A., C. Deser, and L. Sun, 2015a: Projected changes in regional climate extremes arising from Arctic sea ice loss. *Env. Res. Lett.*, **10**, doi: 10.1088/1748-9326/10/8/084006.
- Screen, J. A., C. Deser, and L. Sun, 2015b: Reduced risk of North American cold extremes due to continued Arctic sea ice loss. *Bull. Amer. Meteorol. Soc.*, **96**, doi: 10.1175/BAMS-D-14-00185.1.
- Screen, J. A. and J. A. Francis, 2016: Contribution of sea-ice loss to Arctic amplification is regulated by Pacific Ocean decadal variability. *Nature Clim. Change*, **6**, 856–860, doi: 10.1038/nclimate3011.
- Screen, J. A. and I. Simmonds, 2010: Increasing fall-winter energy loss from the Arctic Ocean and its role in Arctic temperature amplification. *Geophys. Res. Lett.*, **37**, L16707, doi: 10.1029/2010GL044136.
- Screen, J. A., et al., 2018: Consistency and discrepancy in the atmospheric response to Arctic sea-ice loss across climate models. *Nature Geoscience*, **1**.
- Serreze, M. C., A. P. Barrett, and J. Stroeve, 2012: Recent changes in tropospheric water vapor over the Arctic as assessed from radiosondes and atmospheric reanalyses. *J. Geophys. Res. Atmos.*, **117**, doi: 10.1029/2011JD017421.
- Serreze, M. C. and R. G. Barry, 2005: *The Arctic Climate System*. Cambridge University Press, Cambridge, UK.
- Serreze, M. C. and R. G. Barry, 2011: Processes and impacts of Arctic amplification: A research synthesis. *Glob. Planet. Change*, **77**, 85–96, doi: 10.1016/j.gloplacha.2011.03.004.
- Sims, C. A., 1980: Macroeconomics and reality. *Econometrica: Journal of the Econometric Society*, 1–48.
- Smith, D. M., N. J. Dunstone, A. A. Scaife, E. K. Fiedler, D. Copsey, and S. C. Hardiman, 2017: Atmospheric response to Arctic and Antarctic sea ice: The importance of ocean–atmosphere coupling and the background state. *Journal of Climate*, **30**, 4547–4565.
- Spirtes, P. and C. Glymour, 1991: An algorithm for fast recovery of sparse causal graphs. *Social science computer review*, **9** (1), 62–72.

- Spirtes, P., C. Glymour, and R. Scheines, 1991: From probability to causality. *Philos. Stud.*, **64**, 1–36.
- Spirtes, P., C. Glymour, and R. Scheines, 2000: *Causation, Prediction, and Search*. 2d ed., MIT Press.
- Stokes, P. A. and P. Purdon, 2017: A study of problems encountered in Granger causality analysis from a neuroscience perspective. *Proceedings of the National Academy of Sciences*, **114**, E7063–E7072.
- Strong, C. and G. Magnusdottir, 2008: Tropospheric Rossby wave breaking and the NAO/NAM. *Journal of the atmospheric sciences*, **65** (9), 2861–2876.
- Strong, C., G. Magnusdottir, and H. Stern, 2009: Observed feedback between winter sea ice and the North Atlantic Oscillation. *J. Climate*, **22**, 6021–6032, doi: 10.1175/2009JCLI3100.1.
- Sun, L., C. Deser, and R. A. Tomas, 2015: Mechanisms of stratospheric and tropospheric circulation response to projected Arctic sea ice loss. *J. Climate*, **28**, 7824–7845, doi: 10.1175/JCLI-D-15-0169.1.
- Sun, L., J. Perlwitz, and M. Hoerling, 2016: What caused the recent “Warm Arctic, Cold Continents” trend pattern in winter temperatures? *Geophys. Res. Lett.*, **43**, 5345–5352, doi: 10.1002/2016GL069024.
- Sung, M.-K., B.-M. Kim, E.-H. Baek, Y.-K. Lim, and S.-J. Kim, 2016: Arctic-North Pacific coupled impacts on the late autumn cold in North America. *Environ. Res. Lett.*, **11**, 084 016.
- Tang, Q., X. Zhang, X. Yang, and J. A. Francis, 2013: Cold winter extremes in northern continents linked to Arctic sea ice loss. *Environ. Res. Lett.*, **8**, doi: 10.1088/1748-9326/8/1/014036.
- Thorncroft, C., B. Hoskins, and M. McIntyre, 1993: Two paradigms of baroclinic-wave life-cycle behaviour. *Quart. J. Roy. Meteor. Soc.*, **119**, 17–55.
- Tibshirani, R., 1996: Regression shrinkage and selection via the lasso. *Journal of the Royal Statistical Society. Series B (Methodological)*, 267–288.
- Tomas, R. A., C. Deser, and L. Sun, 2016: The role of ocean heat transport in the global climate response to projected Arctic sea ice loss. *J. Climate*, **in press**, doi: 10.1175/JCLI-D-15-0651.1.

- Tyrlis, E. and B. J. Hoskins, 2008: The morphology of Northern Hemisphere blocking. *J. Atmos. Sci.*, **65**, 1653–1665, doi: 10.1175/2007JAS2338.1.
- Walker, G. T., 1923: Correlations in seasonal variations of weather, VIII. A preliminary study of world weather. *Mem. Indian Meteor. Dept.*, **24**, 75–131.
- Walker, G. T., 1924: Correlation in seasonal variations of weather, IX. A further study of world weather. *Mem. Indian Meteor. Dept.*, **24**, 275–333.
- Wallace, J. M. and D. S. Gutzler, 1981: Teleconnections in the geopotential height field during the Northern Hemisphere winter. *Mon. Weath. Rev.*, **109**, 784–812, doi: 10.1175/1520-0493(1981)109<0784:TITGHF>2.0.CO;2.
- Walsh, J., 2014: Intensified warming of the Arctic: Causes and impacts on middle latitudes. *Glob. Planet. Change*, **117**, 52–63.
- Wang, Q., S. Danilov, T. Jung, L. Kaleschke, and A. Wernecke, 2016: Sea ice leads in the Arctic Ocean: Model assessment, interannual variability and trends. *Geophys. Res. Lett.*, **43**, doi: 10.1002/2016GL068696.
- Wang, W., B. T. Anderson, R. K. Kaufmann, and R. B. Myneni, 2004: The relation between the North Atlantic Oscillation and SSTs in the North Atlantic basin. *J. Climate*, **17**, 4752–4759, doi: 10.1175/JCLI-33186.1.
- Wettstein, J. and J. Wallace, 2010: Observed patterns of month-to-month storm-track variability and their relationship to the background flow. *J. Atmos. Sci.*, **67**, 1420–1437, doi: 10.1175/2009JAS3194.1.
- Wettstein, J. J. and C. Deser, 2014: Internal variability in projections of twenty-first-century Arctic sea ice loss: Role of the large-scale atmospheric circulation. *J. Climate*, **27**, 527–550, doi: 10.1175/JCLI-D-12-00839.1.
- Wilks, D., 2016: “The stippling shows statistically significant grid points”: How research results are routinely overstated and overinterpreted, and what to do about it. *Bulletin of the American Meteorological Society*, **97**, 2263–2273.

- Woods, C. and R. Caballero, 2016: The role of moist intrusions in winter Arctic warming and sea ice decline. *J. Climate*, **29**, 4473–4485, doi: 10.1175/JCLI-D-15-0773.1.
- Woods, C., R. Caballero, and G. Svensson, 2013: Large-scale circulation associated with moisture intrusions into the Arctic during winter. *Geophys. Res. Lett.*, **40**, 4717–4721, doi: 10.1002/grl.50912.
- Woollings, T., A. Hannachi, and B. Hoskins, 2010: Variability of the North Atlantic eddy-driven jet stream. *Quart. J. Roy. Meteor. Soc.*, **136**, 856–868, doi: 10.1002/qj.625.
- Woollings, T., B. Harvey, and G. Masato, 2014: Arctic warming, atmospheric blocking and cold European winters in CMIP5 models. *Environ. Res. Lett.*, **9**, doi: 10.1088/1748-9326/9/1/014002.
- Wu, Y. and K. Smith, 2016: Response of Northern Hemisphere midlatitude circulation to Arctic amplification in a simple atmospheric general circulation model. *J. Clim.*, accepted.
- Yu, J.-Y., H.-Y. Kao, and T. Lee, 2010: Subtropics-related interannual sea surface temperature variability in the central equatorial Pacific. *J. Climate*, **23**, 2869–2884, doi: 10.1175/2010JCLI3171.1.
- Zappa, G., F. Pithan, and T. Shepherd, 2018: Multimodel evidence for an atmospheric circulation response to Arctic sea ice loss in the CMIP5 future projections. *Geophys. Res. Lett.*, **45**, L076096, doi: 10.1002/2017GL076096.
- Zhang, P., Y. Wu, I. Simpson, K. Smith, X. Zhang, B. De, and P. Callaghan, 2018a: A stratospheric pathway linking a colder Siberia to Barents-Kara Sea sea ice loss. *Science Advances*, **4** (7), eaat6025.
- Zhang, P., Y. Wu, and K. Smith, 2018b: Prolonged effect of the stratospheric pathway in linking Barents-Kara Sea sea ice variability to the midlatitude circulation in a simplified model. *Climate Dynamics*, **50**, 527–539.

APPENDIX A

Additional VAR and LASSO Model Results for CESM

A1 ASSESSING THE SIGNIFICANCE OF THE VAR MODEL

To assess the skill of our VAR model at predicting Z_{500} and T_{polar} , we compare a full, or unrestricted, p -th order VAR model,

$$Z_{500}(t) = a_1 Z_{500}(t-1) + a_2 Z_{500}(t-2) + \dots + a_p Z_{500}(t-p) + \dots \quad (\text{A1a})$$

$$b_1 T_{polar}(t-1) + b_2 T_{polar}(t-2) + \dots + b_p T_{polar}(t-p) + \epsilon_{1,t}$$

$$T_{polar}(t) = c_1 Z_{500}(t-1) + c_2 Z_{500}(t-2) + \dots + c_p Z_{500}(t-p) + \dots \quad (\text{A1b})$$

$$d_1 T_{polar}(t-1) + d_2 T_{polar}(t-2) + \dots + d_p T_{polar}(t-p) + \epsilon_{2,t},$$

to a restricted version of the model. The restricted model is so called because it restricts one variable's ability to predict the other by setting its regression coefficients to zero. For example, if we wanted to restricted T_{polar} 's ability to predict Z_{500} , we would set all b coefficients in Equation A1a to 0,

$$Z_{500}(t) = a_1 Z_{500}(t-1) + a_2 Z_{500}(t-2) + \dots + a_p Z_{500}(t-p) + \dots \quad (\text{A2a})$$

$$\cancel{b_1 T_{polar}(t-1)} + \cancel{b_2 T_{polar}(t-2)} + \dots + \cancel{b_p T_{polar}(t-p)} + \epsilon_{3,t}$$

$$T_{polar}(t) = c_1 Z_{500}(t-1) + c_2 Z_{500}(t-2) + \dots + c_p Z_{500}(t-p) + \dots \quad (\text{A2b})$$

$$d_1 T_{polar}(t-1) + d_2 T_{polar}(t-2) + \dots + d_p T_{polar}(t-p) + \epsilon_{4,t},$$

We can restrict Z_{500} 's ability to predict T_{polar} in a similar manner,

$$Z_{500}(t) = a_1 Z_{500}(t-1) + a_2 Z_{500}(t-2) + \dots + a_p Z_{500}(t-p) + \dots \quad (\text{A3a})$$

$$b_1 T_{polar}(t-1) + b_2 T_{polar}(t-2) + \dots + b_p T_{polar}(t-p) + \epsilon_{5,t}$$

$$T_{polar}(t) = \cancel{c_1 Z_{500}(t-1)} + \cancel{c_2 Z_{500}(t-2)} + \dots + \cancel{c_p Z_{500}(t-p)} + \dots \quad (\text{A3b})$$

$$d_1 T_{polar}(t-1) + d_2 T_{polar}(t-2) + \dots + d_p T_{polar}(t-p) + \epsilon_{6,t},$$

The restricted models (Equation A2, Equation A3) and the full model (Equation A1) are then compared in order to determine significance. If the restricted and full models are determined to be significantly different, the relationship being restricted (T_{polar} driving Z_{500} in Equation A2) can be said to be significant, and Granger-causal (T_{polar} would be a Granger-cause of Z_{500}). While we could also restrict Z_{500} 's ability to predict itself (a coefficients) and T_{polar} 's ability to predict itself (d coefficients), we choose to focus on the restricted models described in Equations A2, A3.

To assess significance, the full model (Equation A1) is separately compared to each restricted model (Equations A2, A3) with a log-likelihood score. A likelihood score, L , is calculated separately for each model, as in Sims (1980),

$$L \equiv (X - c) (\log |\Sigma_r| - \log |\Sigma_u|), \quad (\text{A4})$$

where X is the number of observations, c is the maximum number of regressors in the longest equation, and $|\Sigma_r|$ and $|\Sigma_u|$ are the determinants of the covariance matrices of the restricted and

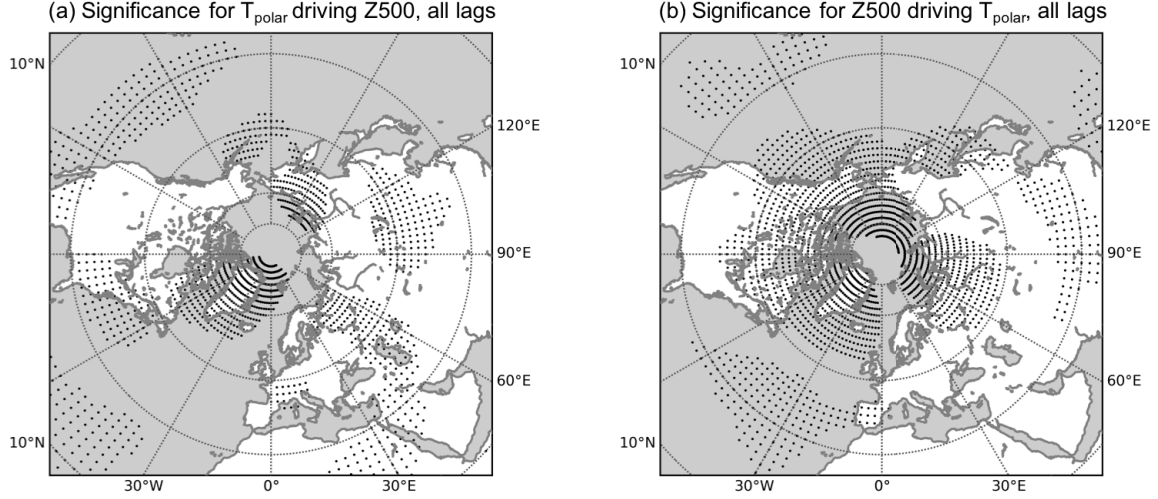


Fig. A1. VAR model gridpoints exhibiting statistical significance according to the log-likelihood score and the field significance test for (a) T_{polar} driving Z_{500} and (b) Z_{500} driving T_{polar} . As previously stated, significance for the VAR model is assessed over all lags.

unrestricted model residuals, respectively. To assess significance, we compute the test statistic, D , which is a ratio of the logarithm of the likelihood ratios (hence, the log-likelihood score),

$$D = 2 \ln \left(\frac{L_{restricted}}{L_{full}} \right) \quad (A5)$$

D , the test statistic, has an asymptotic χ^2 distribution, from which the p -value is determined. Significance is assessed at 95% confidence. We note that Z_{500} has dimensions of [longitude \times latitude \times time], while T_{polar} has dimensions of only [1 \times time]. Thus, a VAR model is created at every gridpoint— T_{polar} is used to predict Z_{500} at each gridpoint, and Z_{500} at each gridpoint is used to predict T_{polar} (and itself at that gridpoint). Since Z_{500} at each gridpoint cannot be assumed to be independent from its neighbors, we apply the field significance test described in Wilks (2016), using a false discovery rate of $\alpha = 0.1$. Thus, all results shown are significant according to both the log-likelihood test, and the field significance test. Figure A1 shows the statistically significant gridpoints for each model— T_{polar} driving Z_{500} , (Figure A1a), and Z_{500} driving T_{polar} (Figure A1b).

A2 RESULTS OF THE VAR MODEL FOR MERRA-2

The results of the two-dimensional VAR model are shown in Figure A2 (T_{polar} driving Z_{500}) and Figure A3 (Z_{500} driving T_{polar}); the LASSO results are reproduced for easy comparison. The relationships seen in the LASSO model are reproduced in the VAR model, with regions that are significant in the LASSO model also exhibiting significance in the VAR model. We note that the coefficients in the VAR model are larger than those of the LASSO model. This is expected, since LASSO shrinks the overall value of the regression coefficients (e.g., Hastie et al. (2015)).

We also apply the VAR model to the individual regions listed in Table 1 and shown in Figure 4. The results of the regional one-dimensional VAR models are shown in Figure A4; coefficients that were significant in the LASSO model are in bold in Figure A4. As in Figures A2, A3, the VAR

coefficients are generally larger than their LASSO counterparts, explaining anywhere from 2 to 5 times as much variance as the LASSO models would suggest. Finally, we note that we also performed a VAR analysis on output from the CESM-Large Ensemble pre-industrial control run (Kay et al. (2015)). The results from 1798 years of the CESM-LE pre-industrial control run were broadly similar to those of the MERRA-2 reanalysis. We also sub-sampled the CESM output at 37-year intervals, to match the MERRA-2 record, and performed a separate VAR analysis on each 37-year chunk. The results of this VAR analysis are included in subsequent sections.

A3 VAR MODEL RESULTS FOR CESM

While the primary focus of Chapter 4 is on understanding the Arctic-midlatitude causal connections in reanalysis, a similar framework was also applied to climate model output, specifically, the Community Earth System Model–Large Ensemble (CESM-LE) pre-industrial control simulation (Kay et al. (2015)). The goals of this analysis are two-fold: one, to compare the results of the MERRA-2 analysis to those of a climate model with 1800 years of output; and two, to begin to explore how low-frequency variability could impact the sub-monthly Arctic-midlatitude relationships. For example, Screen and Francis (2016) demonstrated that Arctic sea ice concentrations are sensitive to the state of the extratropical Pacific Ocean—a different PDO phase can yield substantial differences in Arctic sea ice concentrations, which can thus impact the two-way relationships between the Arctic and midlatitudes. Arctic warming is larger and sea ice loss is enhanced during the negative phase of the PDO relative to the positive phase. While this research was not included in the publication that resulted from Chapter 4, it provides some interesting results, and could suggest some areas for future research.

A1 CESM Model Output

We use 1798 years of general circulation model (GCM) output from the fully-coupled Community Earth System Model–Large Ensemble (CESM) preindustrial control simulation (Kay et al. (2015)). In this experiment, all external forcing is fixed at 1850 levels, with ozone forcing derived from the Whole Atmosphere Community Climate Model (WACCM). We focus our analysis on 850-hPa temperatures from 70°-90° N (T_{polar}), and 500-hPa geopotential height in the Northern Hemisphere (Z_{500}). In the first part of our study, we analyze all 1798 years of the control run together. In the second part, we subsample the model output at consecutive 37-year intervals (to match the time period covered by our reanalysis) with 50% overlap, giving us a total of 93 samples that are 37 years long. With nearly 2,000 years of daily climate model output, we expect an excellent sampling of internal variability, while our 37-year subsampled model output will allow us to have a better comparison to reanalysis, as well as to more fully isolate the subseasonal variability that is the focus of our study. We compare the results of the regression model applied to the CESM output to the results of the Modern-Era Retrospective analysis for Research and Applications, Version 2 (MERRA-2, GMAO (2015); detailed in Chapter 4).

For both the model output and reanalysis, we focus on two primary variables. The first is Z_{500} , which is the Northern Hemisphere 500-hPa geopotential height at every gridpoint (dimensions of longitude by latitude by time). The second is T_{polar} , which is the zonally-averaged 850 hPa temperature averaged from 70-90°N (a time series). The seasonal cycle is removed from both sets of variables, and 5-day means are taken with both so as to remove emphasize the 5-25 day subseasonal variability of the circulation. Here, we focus only on boreal winter (December-February) so

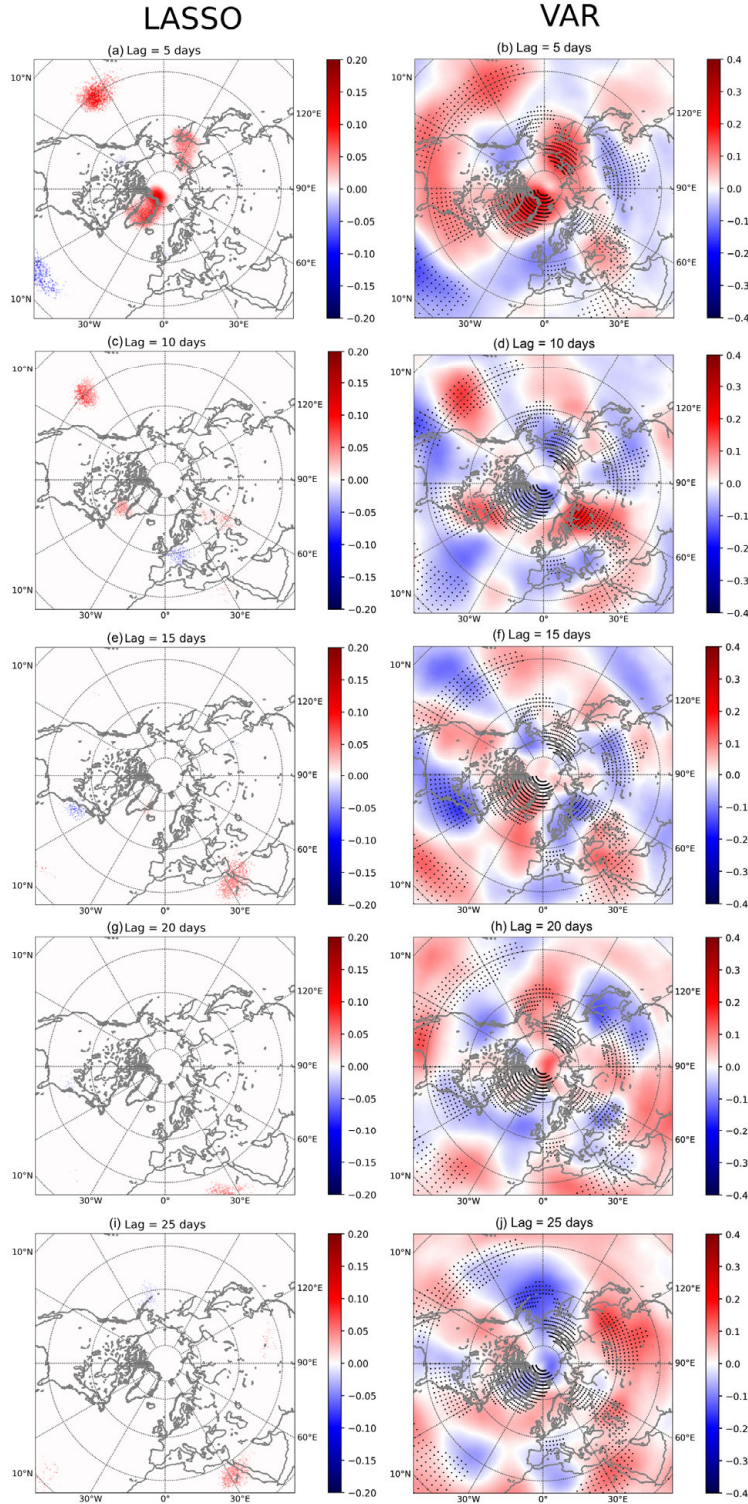


Fig. A2. LASSO (left) and VAR (right) models of T_{polar} driving Z_{500} at each gridpoint at lags of (a,b) 5 days to (i,j) 25 days. For the LASSO model, only gridpoints where T_{polar} drives a significant response in Z_{500} at that gridpoint are shown. For the VAR model, stippling indicates gridpoints where T_{polar} drives a significant response in Z_{500} at that gridpoint are shown.

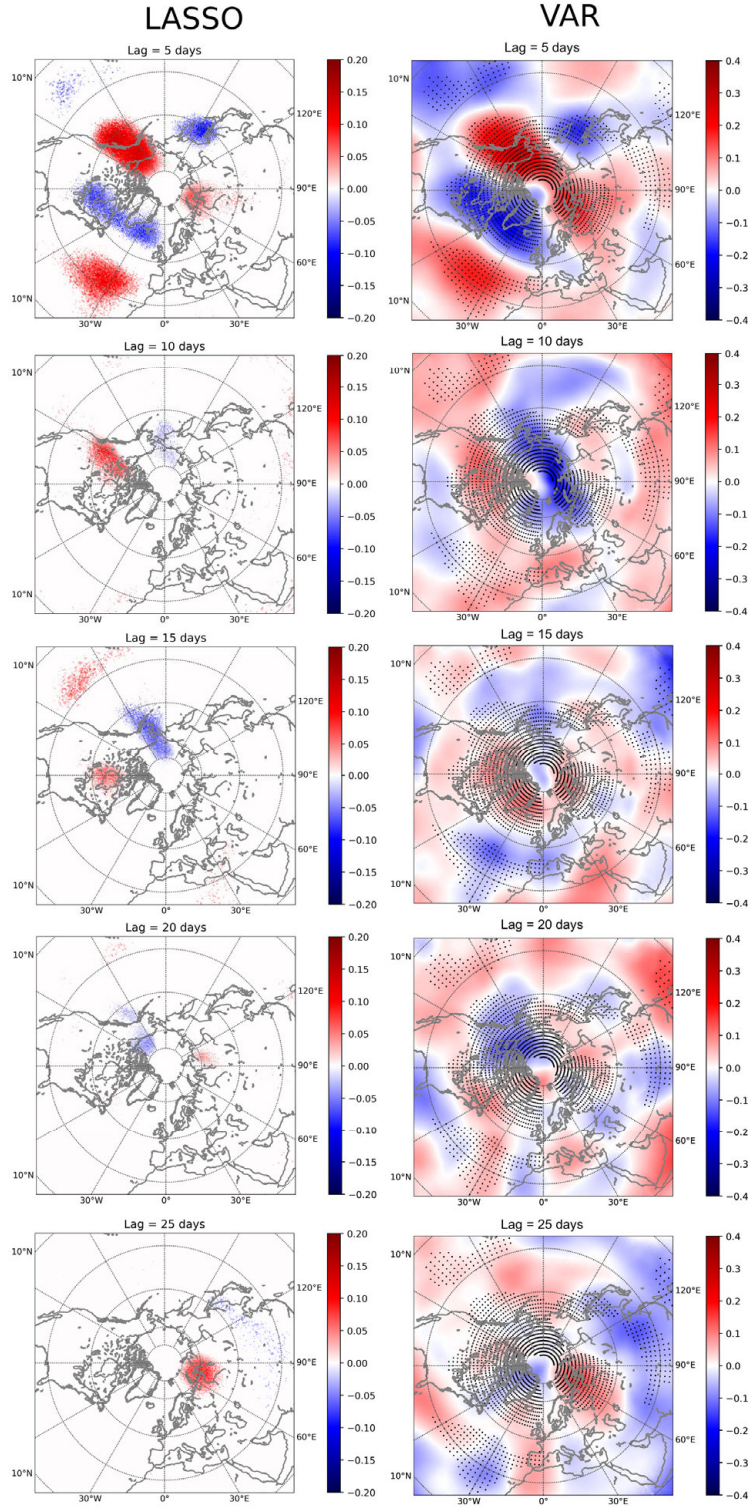


Fig. A3. LASSO (left) and VAR (right) models of Z_{500} at each gridpoint driving T_{polar} at lags of (a,b) 5 days to (i,j) 25 days. For the LASSO model, only gridpoints where Z_{500} at that gridpoint drives a significant response in T_{polar} are shown. For the VAR model, stippling indicates gridpoints where Z_{500} at that gridpoint drives a significant response in T_{polar} are shown.

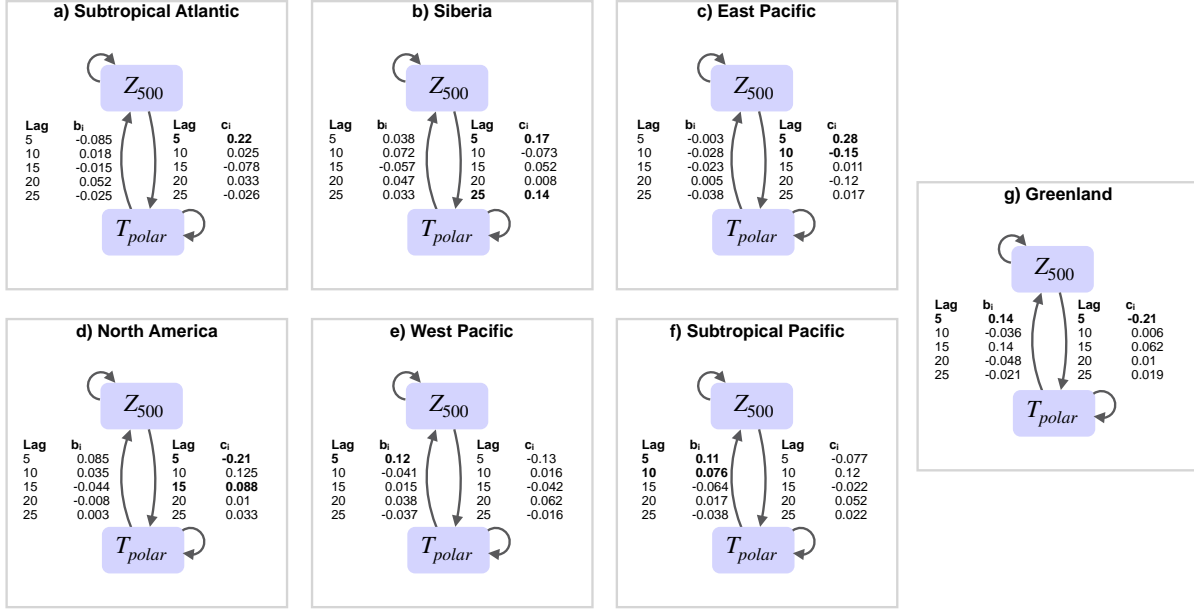


Fig. A4. VAR model results for the 7 regions outlined in Table 1. Coefficients that were significant in the LASSO model are in bold. Curved arrows indicate autoregressive relationships (coefficients not shown).

as to smooth out higher-frequency variability. As described in detail in Chapter 4, we evaluate our regression model in the context of Granger causality, or added variance explained.

As described in the previous section, we model the relationship between Z_{500} and T_{polar} with a p th-order vector autoregression (VAR) model. A VAR model predicts each model variable using lagged values of all model variables. As we are interested in the two-way relationships between Z_{500} and T_{polar} , we use a two-variable p th-order VAR model,

$$Z_{500}(t) = a_1 Z_{500}(t-1) + a_2 Z_{500}(t-2) + \dots + a_p Z_{500}(t-p) + \dots \quad (\text{A6a})$$

$$b_1 T_{polar}(t-1) + b_2 T_{polar}(t-2) + \dots + b_p T_{polar}(t-p) + \epsilon_{Z,t}$$

$$T_{polar}(t) = c_1 Z_{500}(t-1) + c_2 Z_{500}(t-2) + \dots + c_p Z_{500}(t-p) + \dots \quad (\text{A6b})$$

$$d_1 T_{polar}(t-1) + d_2 T_{polar}(t-2) + \dots + d_p T_{polar}(t-p) + \epsilon_{T,t},$$

where $\epsilon_{Z,t}$ and $\epsilon_{T,t}$ are error terms. Equation A6a uses Z_{500} and T_{polar} to predict Z_{500} —the a_i coefficients quantify Z_{500} 's influence on itself, while the b_i coefficients quantify the influence of T_{polar} on Z_{500} . Similarly, in equation A6b, Z_{500} and T_{polar} are used to predict T_{polar} , with the c_i coefficients quantifying Z_{500} 's influence on T_{polar} , while the d_i coefficients quantify the influence of T_{polar} on itself. We do not allow Z_{500} and T_{polar} to influence each other instantaneously—that is, we assume there is no relationship at lag 0. In this work, we use a model order of $p = 5$ —that is, 5 non-overlapping chunks of 5 day means, for a total of 25 days. We established our optimum p by testing several different values for p . Estimating p using the Akaike information criteria yielded a similar value of $p = 5$ as those tested based on prior knowledge of the climate system. Since Z_{500} is assessed separately at each gridpoint, each gridpoint can be considered its own VAR model, with Z_{500} at that gridpoint being regressed with the T_{polar} time series.

A2 Assessing Skill and Significance

To assess the skill of our VAR model at predicting Z_{500} and T_{polar} , we compare the full, i.e. “unrestricted”, VAR model described above and a “restricted” version of the model. The restricted model restricts one variable’s ability to predict the other by setting its regression coefficient to zero. For example, if we want to restricted T_{polar} ’s ability to predict Z_{500} , we set all b coefficients in equation A6a to 0. The restricted model and the full model are then compared in order to determine significance. Specifically, the two models are compared with a log-likelihood score. A likelihood score, L , is calculated separately for the restricted and the full models, as in Sims (1980),

$$L \equiv (X - c) (\log|\Sigma_r| - \log|\Sigma_u|), \quad (\text{A7})$$

where X is the number of observations, c is the maximum number of regressors in the longest equation, and $|\Sigma_r|$ and $|\Sigma_u|$ are the determinants of the covariance matrices of the restricted and unrestricted model residuals, respectively. These scores are used to assess significance via a test statistic, D , which is the ratio of the logarithm of the likelihood ratios (hence, the “log-likelihood score”),

$$D = 2 \ln \left(\frac{L_{restricted}}{L_{full}} \right). \quad (\text{A8})$$

The test statistic, D , has an asymptotic χ^2 distribution, from which the p -value is determined. Significance is assessed at 95% confidence following the false discovery rate criteria described in Wilks (2016), with $\alpha_{FDR} = 0.10$. Significance is assessed over the entire model—that is, for a gridpoint to be significant, it must be significant when all lags are considered; this also means that significance is the same for all lags. We note that since there are 1800 years of CESM results, nearly all gridpoints will exhibit a statistically significant response when all 1800 years of model output are analyzed at once.

A3 Results for Full Climate Model

We apply the full and restricted VAR models to both the 1798 years of CESM pre-industrial control run model output as well as 37 years of MERRA-2 reanalysis. We note that both T and Z_{500} exhibit substantial autocorrelation, as expected. However, as the focus of this work is on the influence of T_{polar} on Z_{500} , and vice versa, we focus on these parts of the VAR model (e.g., the b and c coefficients of equation 1(a),(b)). Since the VAR model separates the predictability of, for example, Z_{500} into a component driven by Z_{500} , and another driven by T_{polar} , we can and do focus only on the cross-correlation terms. As the large sample size in the CESM output (1800 years) means that nearly all gridpoints will exhibit a statistically significant response, we focus primarily on regions which are statistically significant in both MERRA-2 and CESM. The left panels of Figure A5 show the role of Arctic temperature (T_{polar}) in driving variability in Z_{500} at lags from 5-25 days in the CESM model output, while the right panels of Figure A5 show the same for MERRA-2 reanalysis. Figure A6 shows the role of Z_{500} at each gridpoint in driving variations in T_{polar} for (left) the CESM model output and (right) the MERRA-2 reanalysis. In both figures, the top two panels show the locations with statistically significant gridpoints. Generally speaking, the patterns in MERRA-2 (right columns of Figures A5 and A6) are reproduced in the CESM pre-industrial control run output (left columns of Figures A5 and A6). Many of the dynamical aspects of the Arctic-midlatitude circulation are discussed in more detail in Chapter 4, so we simply summarize some key points from Figures A5 and A6:

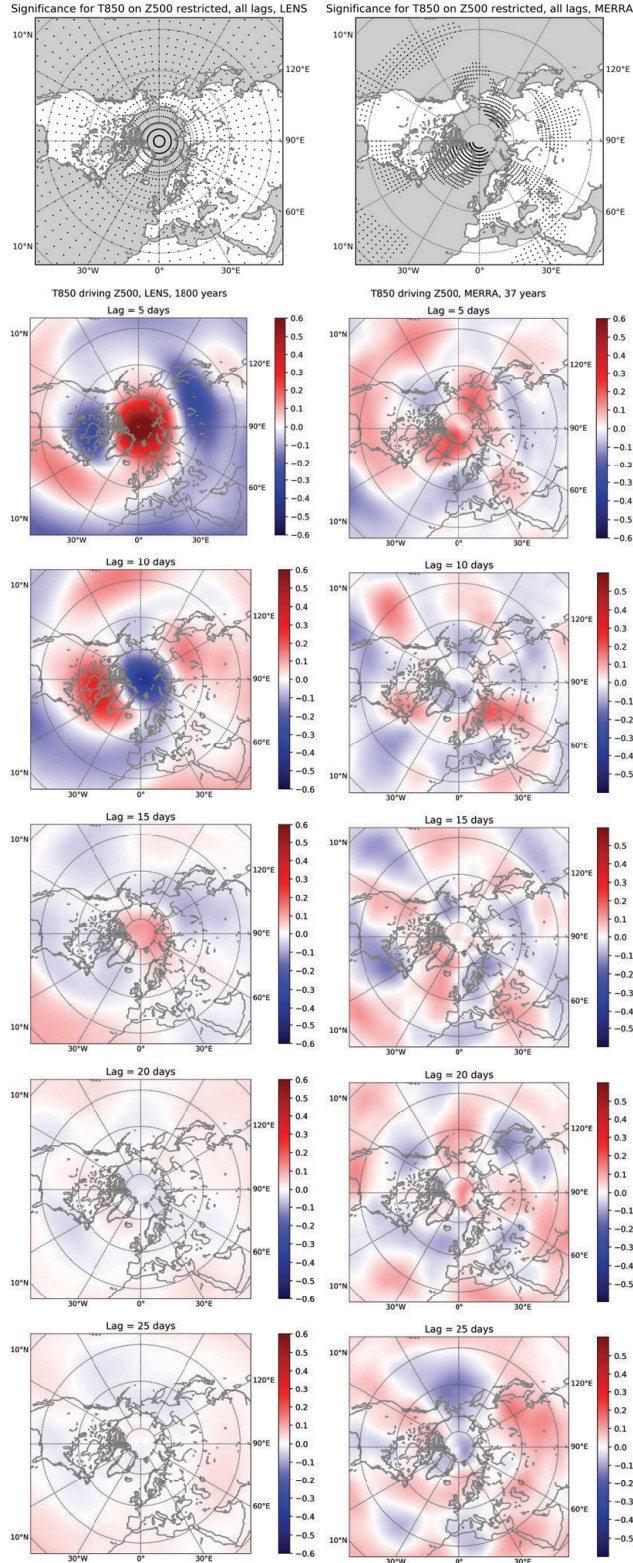


Fig. A5. (a,b) Statistical significance for VAR model where T_{polar} drives Z_{500} for (a) CESM and (b) MERRA-2. (c-l) T_{polar} driving Z_{500} for (left) CESM and (right) MERRA-2 at lags of (c,d) 5 days to (k,l) 25 days.

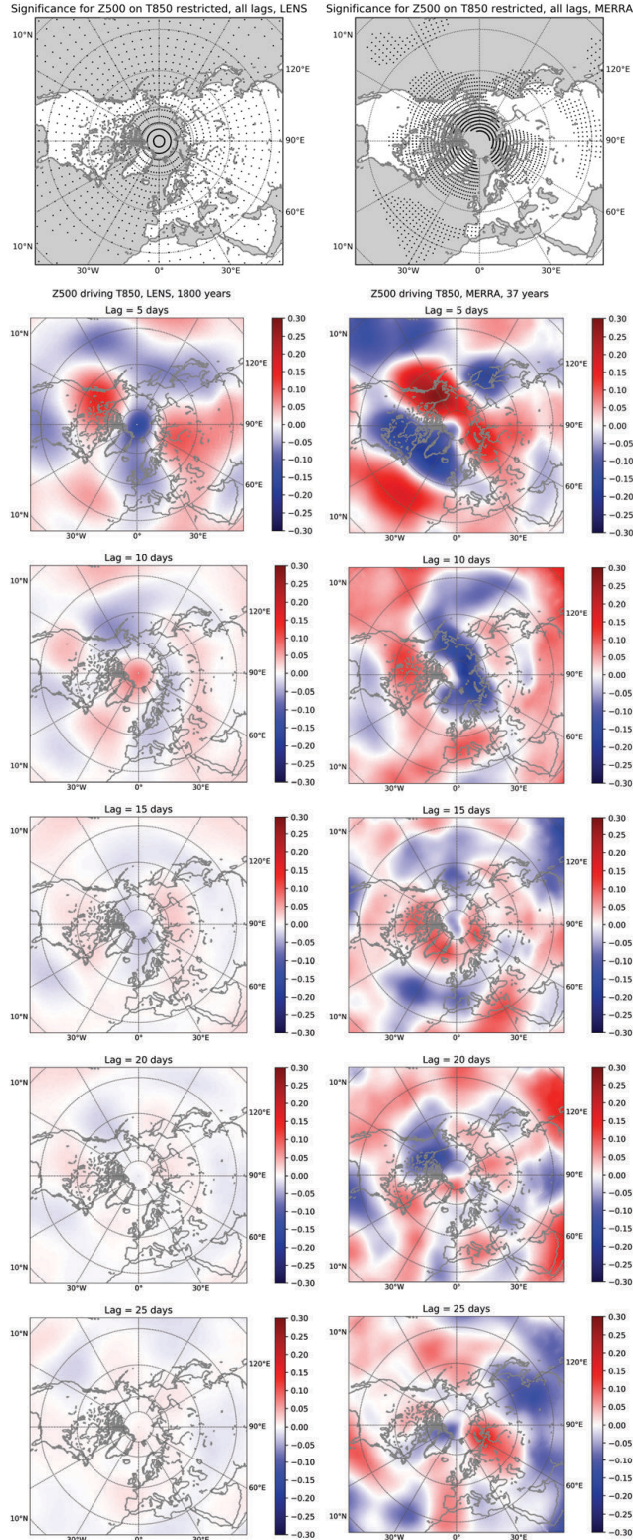


Fig. A6. (a,b) Statistical significance for VAR model where Z_{500} drives T_{polar} for (a) CESM and (b) MERRA-2. (c-l) Z_{500} driving T_{polar} for (left) CESM and (right) MERRA-2 at lags of (c,d) 5 days to (k,l) 25 days.

- (1) The results from fully-coupled climate model and the reanalysis look broadly similar, suggesting that to first order, the CESM model output is able to represent the important processes of the Arctic-midlatitude teleconnection variability;
- (2) The patterns of Z_{500} driving T_{polar} are not the same—that is, the regions that are influenced by the Arctic are not necessarily those that are influenced by the Arctic;
- (3) The MERRA-2 reanalysis shows many regions of statistical significance, suggesting that 37 years is enough to identify a response that stands out significantly from internal variability (e.g., much of the dynamical response is driven by high-frequency variability); and finally,
- (4) The magnitude of the MERRA-2 response is larger than that of the CESM response.

Regarding the final point, there are several possibilities for the weaker response in CESM. The first is of course model deficiencies; the second is that the MERRA-2 reanalysis includes forcing from greenhouse gas warming, while the pre-industrial control model output does not have greenhouse gas warming. The third possibility is that lower-frequency variability captured in the 1800 years of model output, but not in the 37 years of reanalysis, is influencing at least some part of the Arctic-midlatitude feedbacks. The third possibility is explored in more detail in the next section by subsampling the climate model output.

A4 Results for Subsampled Climate Model

We note that the comparison between 1798 years of climate model output and 37 years of reanalysis is not entirely fair. While the two products present broadly similar patterns of Arctic-midlatitude influence, the fact remains that the climate model output could be incorporating the influence of very low frequency variability that is not accurately represented in the relatively short reanalysis record. For example, the midlatitude circulation is certainly sensitive to background conditions and low-frequency variability (CITE). Furthermore, recent work has shown that low-frequency variability in the oceans can also affect conditions in the Arctic (e.g. Screen and Francis (2016), Lee et al. (2015), Sung et al. (2016), Osborne et al. (2017), Smith et al. (2017), Peings and Magnusdottir (2016)). As the CESM model output set is approximately two orders of magnitude longer than that of MERRA-2, it is of interest to try to isolate the effects of this low-frequency variability and to ensure that the patterns seen in Figures A5, A6, are not simply dominated by, for example, the ocean state.

To that end, we subdivide the 1798 years of CESM model output into consecutive segments of 37 years. Each segment has 50% overlap, yielding 93 37-year segments of model output. These 37-year chunks of CESM output are separately analyzed following the methods outlined in section 2. Agreement between the 37 year segments is assessed by comparing the sign of the regression coefficient at each gridpoint. The percentage of chunks that agrees on the sign of the regression coefficient at each gridpoint is plotted in Figure A7. Red indicates that the sign of the regression coefficient is positive, while blue indicates that the sign is negative. Darker colors indicate better agreement. The robustness of the sign of the regression coefficient is assessed at 95% using a binomial distribution for both T_{polar} driving Z_{500} (right) and Z_{500} driving T_{polar} (left). For an effective sample size of 46 (we reduce N by half since the 37 year segments have 50% overlap), we require at least 71% of the 37-year chunks (that is, 66 out of 93) to agree on the sign of the response for the result to be considered significant at 95%. In Figure A7, only the statistically significant results are shown.

In both cases— Z_{500} driving T_{polar} , and T_{polar} driving Z_{500} —the agreement is generally quite high and broadly-distributed at the smaller lags, and decreases at larger lags. Again, regions of

agreement for T_{polar} driving Z_{500} are not necessarily the same as those for Z_{500} driving T_{polar} . In particular, the sign agreement for Z_{500} driving T_{polar} is low after lag day 10. There are a few regions of significant sign agreement at longer lags for T_{polar} driving Z_{500} —much of east Asia, eastern North America and the central Arctic exhibit broad regions of sign agreement at lag day 15; and areas of significant sign agreement remain over the ocean basins up to lag day 25. Central Asia also shows a re-emergent signal of sign agreement T_{polar} driving Z_{500} at lag day 25. This region of cohesive sign agreement in CESM at lag day 25 in Figure A7 (bottom panels) is adjacent to the region of re-emergence in Z_{500} driving T_{polar} (bottom panels of Figure A6). Snow cover in this region has been linked to driving a large-scale atmospheric response; this midlatitude variability could drive further Arctic variability (e.g., Cohen et al. (2012), Furtado et al. (2015), Handorf et al. (2015)); however, this is certainly conjecture, as the relationship between Figure A7 (bottom panels) and Figure A6 (bottom panels) has not been further explored.

After the analysis of Figure A7, preliminary analysis was carried out regarding the role of low-frequency variability on the higher frequency sub-monthly Arctic-midlatitude connection patterns. We applied a LASSO model to select regions, similar to Chapter 4, and explored the graphical results of the LASSO model. We then composited sea surface temperatures (SST) based on LASSO results. Overall, the SST results did suggest some potentially interesting areas that could be sources of low-frequency variability, including variability in the Southern Ocean. However, this analysis is very preliminary, and ultimately, for reasons sufficient to the author, it has not been included in this dissertation.

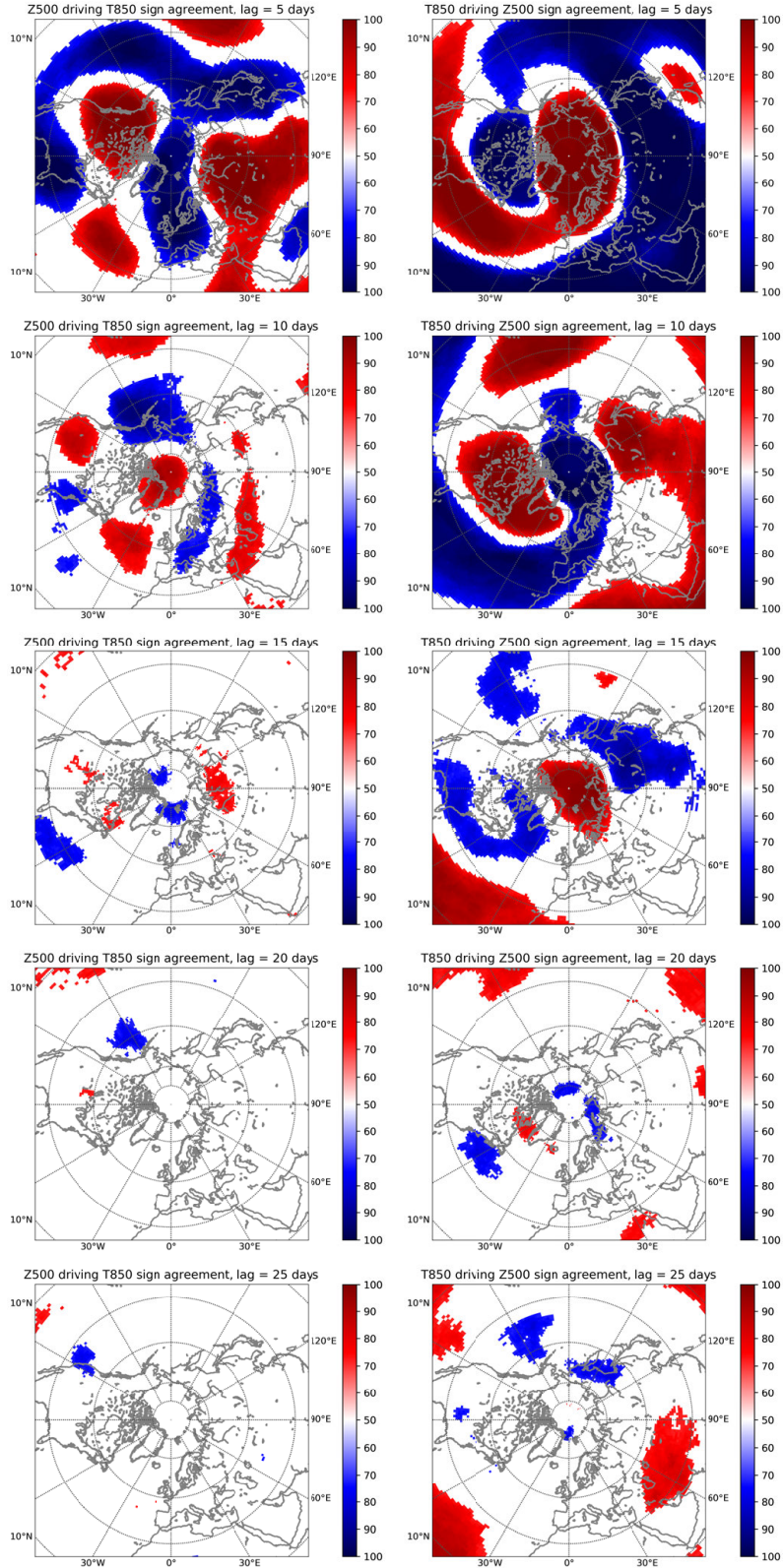


Fig. A7. Percent of 37-year chunks of CESM that agree on the sign of the regression coefficient at each gridpoint for (left) Z500 driving T_{polar} and (right) T_{polar} driving Z500.